UNIVERSIDAD DE BUENOS AIRES
Facultad de Ciencias Exactas y Naturales
Departamento de Física

DESARROLLOS EN DOSIMETRÍA COMPUTACIONAL Y OPTIMIZACIÓN DE TRATAMIENTOS PARA LA TERAPIA POR CAPTURA NEUTRÓNICA EN BORO

Tesis presentada para optar al título de Doctor de la Universidad de Buenos Aires en el área Ciencias Físicas

Sara J. González

Director de tesis: Dr. Robert Zamenhof
Director asistente: Dr. Daniel Batistoni

Lugar de trabajo: Comisión Nacional de Energía Atómica

Buenos Aires, 2005

Resumen

Al igual que en otras formas de radioterapia, el éxito potencial de la Terapia por Captura Neutrónica en Boro (BNCT) se asocia con la posibilidad de entregar dosis altas a los tumores y de preservar los tejidos normales. Para lograr este objetivo, BNCT saca provecho de la alta transferencia de energía de los productos de la reacción $^{10}\mathrm{B}(\mathrm{n},\alpha)^{7}\mathrm{Li}$ y de la acumulación preferencial del boro en las células tumorales. Si bien una fracción importante de la dosis en BNCT se debe a la interacción del campo de neutrones con el compuesto de boro, la dosis total es el resultado de distintas radiaciones que actúan en diferentes escalas de longitud. En consecuencia, tanto los cálculos de dosimetría macroscópica tridimensional como el modelado de la probabilidad de control tumoral son apreciablemente más complejos que en el caso de la radioterapia convencional. Este trabajo presenta desarrollos prácticos y teóricos sobre modelado computacional para cálculos de planificación de tratamiento. Asimismo, introduce un marco teórico que permite incorporar la variabilidad de la relación de concentración de $^{10}\mathrm{B}$ tumor-sangre en los cálculos de dosis absorbidas y probabilidades de control tumoral. En particular, se desarrolló por primera vez un modelo de probabilidad de control tumoral que tiene en cuenta dicha variabilidad y posibles inhomogeneidades de dosis en un volumen tumoral. Además, se elaboró un método novedoso para la determinación de la relación tumor-sangre. Este método se aplicó en el primer tratamiento de melanoma cutáneo llevado a cabo en la Argentina.

Palabras clave: BNCT, melanoma, planificación de tratamiento, modelo voxelizado, probabilidad de control tumoral.

DEVELOPMENTS IN COMPUTATIONAL DOSIMETRY AND TREATMENT OPTIMIZATION FOR BORON NEUTRON CAPTURE THERAPY

Abstract

As in other forms of radiotherapy, the eventual success of the Boron Neutron Capture Therapy (BNCT) is associated with the ability of delivering high doses to the tumors while sparing surrounding normal tissues. To achieve this goal, BNCT takes advantage of the high LET products of the $^{10}B(n,\alpha)^{7}Li$ reaction, and the preferential boron uptake by tumor cells. Although a large fraction of the dose in BNCT is due to the interaction of the neutron radiation field with the boron compound, the total dose is the result of a combination of radiations acting on different length scales. Therefore, detailed macrodosimetry calculations and tumor control probability modeling are significantly more complicated than in conventional radiotherapy. This work presents practical and theoretical developments on computational modeling for treatment planning calculations, and introduces a comprehensive framework for incorporating the variability of tumor-to-blood ^{10}B concentration ratios into the calculation of absorbed doses and tumor control probabilities. Specifically, a tumor control probability model was developed for the first time, which considers this ratio variability as well as the possible dose inhomogeneity throughout the tumor volume. In addition, a new approach to determine tumor-to-blood ratios was presented and applied to the first skin melanoma BNCT treatment performed in Argentina.

Keywords: BNCT, melanoma, treatment planning, voxel model, tumor control probability.

Acknowledgments

I would first like to express my deep gratitude to my advisor Dr. Robert Zamenhof. His open-minded personality and friendship has been of extremely importance not only for his guidance in this work but in the concretion of the clinical trials in Argentina. I am also thankful for giving me the opportunity to work with him and his group in Boston, a rewarding experience that I will never forget. I would also like to thank Dr. Daniel Batistoni for his assistance, advice and suggestions for this work.

I thank Dr. Sara Liberman who has provided the environment where students and investigators of many areas can perform radiation research. She allowed me to participate in the BNCT project of Argentina and supported me in many ways, for which I am very grateful.

I want to express my deepest gratitude to my group Instrumentación y Control. I am thankful for their faith in me that I would concrete this work. Thanks to Silvia and Marcelo for their continuous encouragement, respect and support. I am indebted with them. Thanks also to Gustavo, Manuel, Emilio, Carlos, Claudio, Lili, Pepe y Juan who have made contributions to this work, both directly and indirectly.

I have to say a big thanks to Salvador Gil and Amanda Schwint. They were a key point in the development of my career, for which I will be always grateful. I am also very grateful to Marcelo Venere for his disinterested help when I needed it.

Thanks to all those people who participate in the BNCT project. Alejandra Dagrosa and Raúl Jiménez Rebagliati, who provided tumor and blood boron measurements in patients, are much appreciated. The work of Herman Blaumann, Osvaldo Calzetta and Juan Longhino in beam modeling and physical dosimetry of the RA-6 reactor is also gratefully acknowledged. Thanks to the medical physicists and oncologists of the Instituto Roffo for sharing their experience and knowledge in conventional radiotherapy. Mariana Casal and Marcelo Bonomi are particularly acknowledged.

I would like to thank to the Departamento de Física of Tandar, CNEA, for its kind hospitality. Daniel Saldívar and Roberto De Luca are also thanked for their technical support.

My eternal friends, Vero, Andrés, Sebas and Lucas definitely made this long way easier, funnier and less arduous. Many thanks to my family for their support and encouragement. To my brother Federico, for his infinite patience in reading and correcting many many English texts, and to my brother Martín for introducing Lola to our lives.

Finally, to the person who admire and love with all my heart, Daniel. Without his help I could not have completed this project.

Peer reviewed papers included in this thesis

1. H. R. Blaumann, S. J. González, J. Longhino, G. A. Santa Cruz, O. A. Calzetta Larrieu, M. R. Bonomi, B. M. C. Roth, Boron neutron capture therapy of skin melanomas at the RA-6 reactor: a procedural approach to beam set up and performance evaluation for upcoming clinical trials. *Med. Phys.* **31** (1), 70-80, 2004.

2. S. J. González, M. R. Bonomi, G. A. Santa Cruz, H. R. Blaumann, O. A. Calzetta Larrieu, P. Menéndez, R. Jiménez Rebagliati, J. Longhino, D. B. Feld, M. A. Dagrosa, C. Argerich, S. G. Castiglia, D. A. Batistoni, S. J. Liberman, B. M. C. Roth, First BNCT treatment of a skin melanoma in Argentina: Dosimetric Analysis and clinical outcome. *Appl. Radiat. Isotopes* **61**, 1101-1105 (2004).

3. S. J. González, D. G. Carando, M. R. Bonomi, A new approach to determine tumor-to-blood ^{10}B concentration ratios from the clinical outcome of a BNCT treatment. *Appl. Radiat. Isotopes* **61**, 923-928 (2004).

4. S. J. González, D. G. Carando, G. A. Santa Cruz, R. G. Zamenhof, Voxel model in BNCT treatment planning: performance analysis and improvements. *Phys. Med. Biol.* **50**, 441-458 (2005).

5. S. J. González and D. G. Carando, Effects of tumor-to-blood ^{10}B concentration ratio variability and dose inhomogeneity on dosimetry and tumor control probability in boron neutron capture therapy. (Submitted for publication)

Peer reviewed papers partially included in this thesis

6. M. R. Casal, S. J. González, H. R. Blaumann, J. Longhino, O. A. Calzetta Larrieu, C. A. Wemple, Comparison of the performance of two NCT treatment planning systems using the therapeutic beam of the RA-6 reactor. *Appl. Radiat. Isotopes* **61**, 805-810 (2004).

7. S. J. Liberman, A. Dagrosa, R. A. Jiménez Rebagliati, M. R. Bonomi, B. M. Roth, L. Turjanski, S. I. Castiglia, S. J. González, P. R. Menéndez, R. Cabrini, M. J. Roberti and D. A. Batistoni. Biodistribution studies of boronophenylalanine-fructose in melanoma and brain tumor patients in Argentina. *Appl. Radiat. Isotopes* **61**, (2004), 1095-1100.

Contents

List of Figures

List of Tables

Chapter 1

Introduction

1.1 Overview

Cancer is the uncontrolled growth and spread of cells that may affect almost any tissue of the body. More than 10 million people are diagnosed with cancer every year in the world, being the second leading cause of death by illness in Argentina.

Skin cancer is an important public health concern. Among the different common types of skin cancer, cutaneous malignant melanoma is the most aggressive and life-threatening cancer. The incidence of cutaneous melanoma in the European Community and United States is 17000 and 50000 new cases per year, respectively [25, 82], and continues to rise faster than any other malignancy. There is a lack of incidence records in Argentina but 350 deaths are reported per year from this disease [70]. Several factors influence the survival rate of people who have malignant melanoma. Examples are tumor size, depth of invasion, tumor thickness, and tumor stage at diagnosis. The average length of survival is fewer than 13 months, with a survival rate at five years of only 13% for patients with the highest combination of risk factors [82].

Cutaneous melanoma is generally considered a highly metastatic disease wherein surgery is the mainstay of treatment due to the lack of an effective systemic treatment.

Surgery is usually reserved for management of primary disease and occasionally lymphatic spread. Radiation likewise has an important role for a number of patients in the treatment of localized disease. Radiotherapy is used as adjuvant treatment when micro- or macroscopic residual disease is left in situ and a reintervention is not feasible for medical reasons, for unacceptable morbidity or for cosmetic limitations, and as a palliative therapy in cases of local relapses and metastatic disease.

The clinical experience treating melanoma with radiation is mixed. While there is a widespread belief that melanomas are unusual in their limited response to doses of radiation that would have had a more pronounced effect on other tumors of similar size, an increasing number of clinical studies have supported the view that malignant melanoma is a radioresponsive tumor provided large doses per fraction are applied. Also, some reports indicate that despite the disseminated nature of this disease, proper local treatment of patients presenting with local/regional disease may have an improved survival [79].

The limited effectiveness of conventional radiation have prompted interest in the use of Boron Neutron Capture Therapy (BNCT) to treat melanoma. Conventional radiation therapy involves the use of high-energy X-rays or electron beams. This form of radiation is termed "sparsely ionizing" and is described as having a low linear energy transfer (LET) since the energy depositions in tissue as ionizations are spatially infrequent. A higher absorbed dose to tumor relative to normal tissue is achieved by precise geometric target localization, judicious computer-aided treatment planning and accurate beam delivery systems [49]. Neutron Capture Therapy (NCT) is a technique that was designed to selectively target high LET heavy charged particle radiation to tumors at the cellular level. The concept of NCT was first proposed shortly after the discovery of the neutron by Chadwick in 1932, and the large thermal neutron capture cross-section of the naturally occurring isotope ^{10}B by Goldhaber in 1934. Goldhaber discovered that ^{10}B had an unusually high avidity for absorbing slow or "thermal" neutrons (energy < 0.5 eV). Immediately after capturing a thermal neutron ^{10}B briefly becomes ^{11}B, then immediately

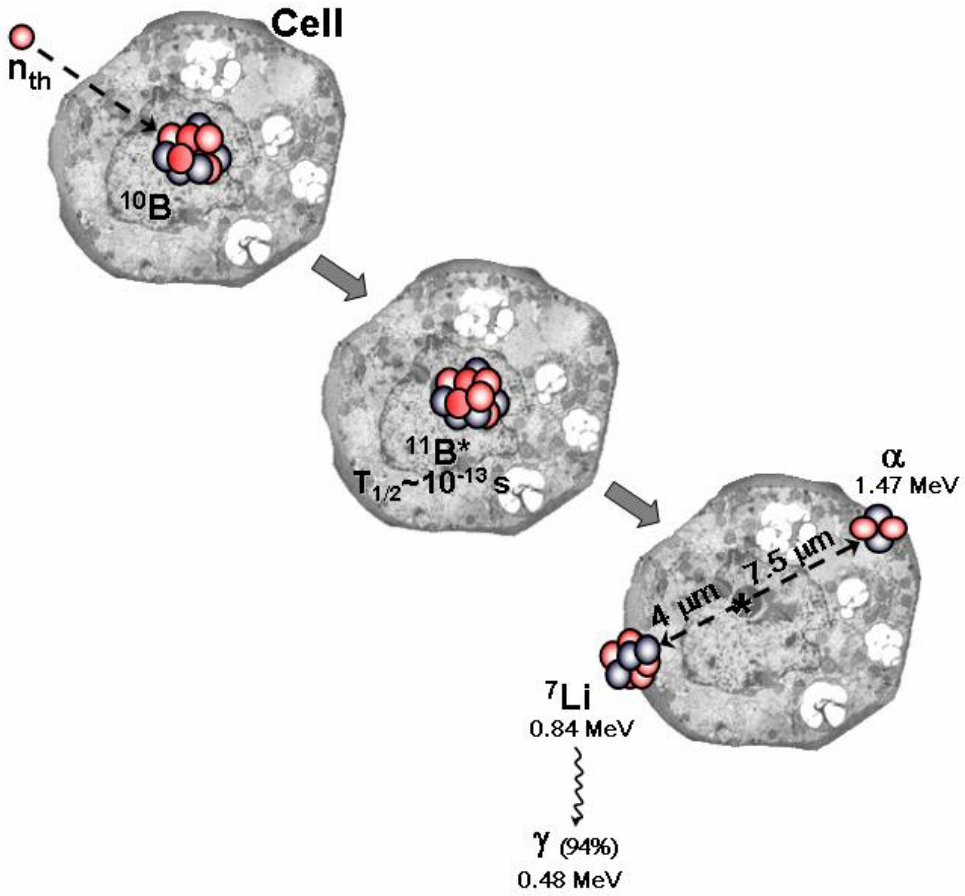

Figure 1.1: Boron neutron capture reaction $^{10}\mathrm{B}(\mathrm{n},\alpha)^{7}\mathrm{Li}^{*}$. The densely ionizing particles have a combined range in tissue of $\sim 12-14$ μm, comparable with cellular dimensions. The reaction releases an average of 2.79 MeV per neutron capture.

disintegrates into an energetic alpha particle back to back with a recoiling ^{7}Li ion. As depicted by Fig. 1.1, these densely ionizing particles have a combined range in tissue of $\sim 12-14$ μm (comparable with cellular dimensions) and a combined average kinetic energy of 2.34 MeV.

Gordon Locher first proposed the principle of BNCT in 1936 [65]. He postulated that if boron could be selectively concentrated in a tumor and the volume was then exposed to thermal neutrons, a higher radiation dose to the tumor relative to adjacent normal tissue would result. In this way, targeting is primarily accomplished by selectively concentrating

the boron drugs in the tumor rather than by aiming the beam. Therein lies the rationale for the clinical implementation of the concept of BNCT.

The Massachusetts General Hospital and the Brookhaven National Laboratory conducted in the 1950s and 1960s, the first clinical trials to treat primary high-grade brain tumors -glioblastoma multiforme (GBM)- using thermal neutrons [88]. Due to poor selectivity of the boron delivery agents and the shallow penetration of the thermal neutron beams from nuclear reactors, these initial trials failed to demonstrate significant prolongation of life or any evidence of therapeutic efficacy. However, the development of new boron compounds that yielded more favorable tumor-to-normal tissue concentration ratios and more penetrating beams (epithermal beams) renewed the interest in BNCT.

The initial human clinical experience irradiating patients with melanoma took place in Japan under the direction of Y. Mishima. After the successful basic research of 13 years, this group started in 1987 the first clinical trial of melanoma using the amino acid p-boronophenylalanine (BPA) as a boron carrier, and the thermal neutron facility of the Kyoto Research Reactor [31]. Since melanoma cells synthetise melanin, the concept was to incorporate ^{10}B into a melanin precursor such as the phenylalanine. BNCT trials in Japan have shown a 73% complete response rate in cutaneous melanoma, which seems encouraging for a disease with an ominous prognosis [30].

Motivated by these promising results together with the positive experience of the melanoma program in the United States [68], a Phase I/II[1] clinical trial for treating cutaneous melanomas with BNCT was designed in Argentina by the Comisión Nacional de Energía Atómica (CNEA), and the medical center Instituto Roffo. In 2003, after seven years of preparation and basic research, the CNEA BNCT research group commenced the clinical trials of BNCT for peripheral melanomas. The protocol involves single administrations of boronophenylalanine-fructose boron compound (BPA-F) [20], followed

[1]Phase I trial: dose finding study where the primary objective is to determine the Maximum Tolerable Dose of the treatment, and to define the toxcities of the treatment. Phase II trial: tests the ability of the treatment to produce measurable tumor shrinkage in a small to medium sized group of patients, all with the same kind of advanced cancer.

by single fraction mixed neutron beam irradiations using the BNCT facility of the RA-6 reactor located at the Centro Atómico Bariloche (CNEA, Argentina) [13, 14].

1.2 Clinical dosimetry of BNCT

In BNCT medical physics, the generally accepted neutron energy classification is as follows: thermal neutrons, $E \leq 0.5$ eV; epithermal neutrons, 0.5 eV $< E \leq 10$ keV; fast neutrons, $E > 10$ keV.

The neutron capture reaction $^{10}\mathrm{B}(\mathrm{n},\alpha)^{7}\mathrm{Li}$ requires a neutron in the thermal energy range, i.e. energies lower than 0.5 eV. Two different neutron beams are commonly used in BNCT, named thermal and epithermal beams. Thermal neutrons are attenuated exponentially as a function of depth in tissue, primarily by capture in hydrogen. Since for a uniform ^{10}B distribution the boron dose profile follows the thermal neutron flux, their therapeutic benefit is limited to very shallow depths. Thus, thermal neutron irradiations have been used for melanoma treatments in the skin [29], as well as with open craniotomy for glioma treatments [45]. Unlike thermal neutron beams, an epithermal beam entering tissue creates a radiation field with a maximum thermal flux at a depth of 2-3 cm, which drops exponentially thereafter. Thus, the current trend for treatment of patients with deep-seated brain tumors is to use epithermal neutron beams. In addition to thermal and epithermal neutron beams, a mixed thermal and epithermal -named *hyperthermal*- neutron beam has been developed at the RA-6 reactor, CNEA, Argentina [7, 13]. RA-6 is a pool-type reactor that has been designed to obtain a thermal neutron flux peak of about 1.0 x 10^{9} cm^{-2} s^{-1} at approximately 1 cm depth. Since the hyperthermal beam configuration provides a boron dose profile that peak at shallow depths into the tissue, this beam is expected to inure to the benefit of surface tumor treatment.

Linear energy transfer (LET) is a measure of the density of the ionizations produced as radiation penetrates tissue. The radiation field produced in tissue during BNCT consists of a mixture of components with different LET characteristics. In addition to the high-

LET products of the $^{10}B(n,\alpha)^{7}Li$ reaction, the interaction of the neutron beam with the nuclei of elements in tissue will deliver an unavoidable, nonspecific background dose, from a mixture of high- and low- LET radiation components, to both tumor and normal tissue [20]. For treatment planning and dosimetry purposes, the combination of the different LET radiations present in the mixed radiation field of BNCT is generally divided according to their source into four primary dose components, namely, the boron dose, thermal neutron dose, fast neutron dose, and photon dose.

As previously discussed, the boron dose is the result of slow neutrons (n_{th}) interacting with ^{10}B atoms in tissue. When a ^{10}B nucleus captures a thermal neutron, it forms an excited state of ^{11}B which immediately fissions into a ^{7}Li nucleus ($T_{1/2} \sim 10^{-13}$s) and an alpha particle (^{4}He). The boron capture reaction releases an average of 2.79 MeV per neutron capture. The recoiling alpha particle and lithium ion carry away an average of 2.34 MeV in the following manner:

$$^{10}B + n_{th} \rightarrow {}^{7}Li\ (0.84\ MeV) + {}^{4}He\ (1.47\ MeV) + \gamma\,(0.48\ MeV) \qquad (93.7\%)$$

$$^{10}B + n_{th} \rightarrow {}^{7}Li\ (1.01\ MeV) + {}^{4}He\ (1.78\ MeV) \qquad (6.3\%)$$

where the branching indicates that the reaction product ^{7}Li may be left either in its ground state or in its first excited state at 0.48 MeV. The excited lithium nucleus quickly returns to its ground state ($T_{1/2} \sim 10^{-13}$ s) with the emission of 0.48 MeV gamma ray. About 94% of all reactions lead to the excited state and only 6% to the ground state [58]. In either case, the reaction products are highly ionizing with initial LET values in tissue of 180 to 370 keV/μm. The lithium ion and alpha particle lose their energy over distances less than 10 μm: 4 (4.5) μm for the ^{7}Li nucleus and 7.5 (9.2) μm for the alpha particle in the case of $^{7}Li^{*}$ ($^{7}Li^{g.s.}$). These distances are in turn less than the diameter of most mammalian cells. The selection of ^{10}B over other isotopes in NCT is related with its large cross section, 3839 barns at 0.0253 eV, its high natural isotopic abundance of 19.8%, and the short range of the resulting reaction products. Also, boron is also available ^{10}B-enriched to values greater than 90%.

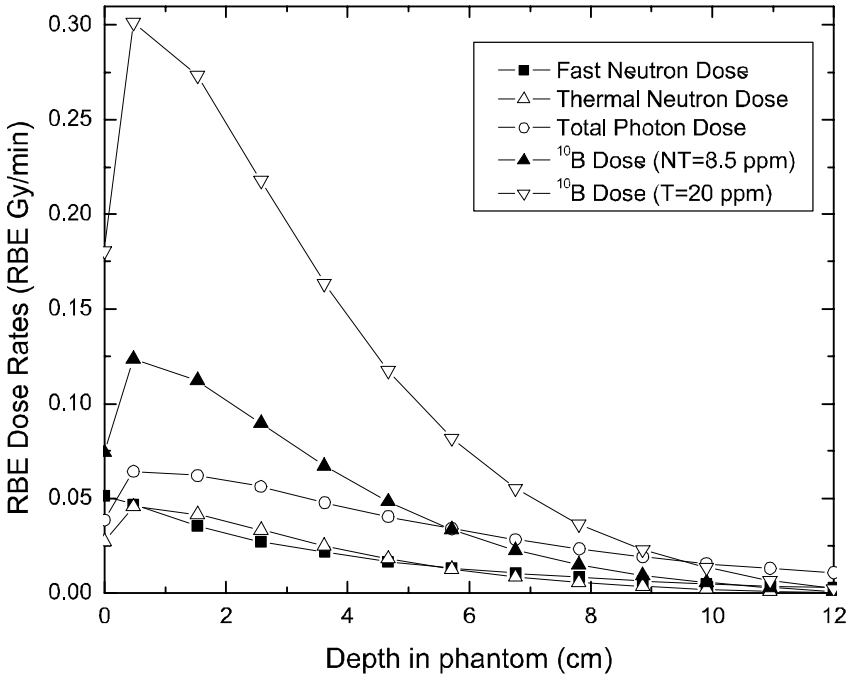

Figure 1.2: In-depth RA-6 reactor dosimetry computed for the cylindrical phantom. Assumed ^{10}B cocentrations: 8.5 ppm for normal tissue (NT), and 20 ppm for tumor (T). Biological effectiveness factors: Neutrons, 3; Photons, 1, Tumor ^{10}B, 3.8; N. Tissue ^{10}B, 2.5.

The thermal neutron dose primarily arises from the $^{14}\mathrm{N}(\mathrm{n},\mathrm{p})^{14}\mathrm{C}$ thermal neutron capture reaction, which releases a high-LET proton with an energy of 590 keV. Contaminating fast neutrons in the beam (those with energies $>$ 10 keV) principally produce high-LET recoil protons with similar average energy through elastic collisions with hydrogen nuclei, i.e. $^{1}\mathrm{H}(\mathrm{n},\mathrm{n}')^{1}\mathrm{H}$, in tissue. Other neutron reactions may also contribute to the fast neutron dose such as the recoils of heavier nuclei (e.g., ^{12}C, ^{16}O and ^{31}P). The photon dose component originates from two sources: contaminating photons produced in the beam structure (incident photon dose), and 2.2 MeV prompt gammas produced by neutron capture in the target, principally by the $^{1}\mathrm{H}(\mathrm{n},\gamma)^{2}\mathrm{H}$ reaction in tissue (induced photon dose). Figure 1.2 illustrates the complexity of BNCT dosimetry showing

the various dose components of the RA-6 neutron beam along the beam axis as a function of depth in a cylindrical water phantom. The depth-dose characteristics of the curves for the $^{10}B(n,\alpha)^{7}Li$ and $^{14}N(n,p)^{14}C$ reactions are similar, each being dependent on the thermal neutron flux. The total photon dose has a broader depth-dose profile due to the greater penetration range of photons. The fast neutron dose is highest at the surface and decreases exponentially as the fast neutrons are attenuated. Although the relatively low concentration of ^{10}B compared to isotopes naturally present in tissues (e.g., ^{1}H and ^{14}N), the boron dose often dominates other dose components. For ^{10}B concentrations of ~ 100 μg/g, the probability of neutron capture by ^{10}B equals that of the natural components in tissue. However, due to the large local energy release in the boron reaction, the minimum requirement for effective BNCT was estimated to be ~ 20 μg/g or $\sim 10^{9}$ atoms/cell.

Due to the high density of ionizations produced along the particle track, high-LET radiation generates more damage in biological systems than an equal physical dose (in Gy) of low-LET radiation. Dose components with different LET characteristics will have different degrees of biological effectiveness with regard to tumor and to the various normal tissues within the treatment volume. To express the total BNCT dose to a given tissue in a common, photon-equivalent unit, each of the high-LET dose components (physical dose in Gy) is multiplied by an experimentally determined biological effectiveness factor. For the non-boron dose components, these factors are known as the relative biological effectiveness factors (RBEs) and are defined as the ratio of doses of a reference radiation (generally cobalt-60 gamma rays) to a test radiation that will produce the same biological endpoint in a given system. In the case of the boron dose component, the biological effectiveness factor is termed compound biological effectiveness (CBE) because it depends not only on the LET of the boron reaction products, but also on the on variations in the microdistribution of different boron compounds, and of the same boron compound in different tissues. The total photon-equivalent BNCT dose can then be expressed as the sum of the biological effectiveness-corrected physical absorbed dose components, using a

unit defined as the Gray-Equivalent (Gy-Eq) or RBE Gy.

Owing to the different radiation transport characteristic of the four dose components, dosimetry calculations in BNCT are more complicated than in conventional photon therapy. In the case of high-energy x-rays, the accurate modeling of the radiation field in the subject's body is based on a combination of calibration measurements performed in cubical water phantoms together with empirically derived correction factors to account for incident body surface curvature, off-axis dose profile behavior, and the effect of internal inhomogeneities. In the case of BNCT, the complex radiation dose field demands to use deterministic transport methods solved by numerical techniques (e.g., discrete-ordinates method), or statistical simulation methods (e.g., Monte Carlo). Although deterministic methods may be applicable to derive the patient's dosimetry, the Monte Carlo stochastic simulation method predominates in BNCT treatment planning systems (TPS) [16, 37, 62, 78, 90].

In the 1990s, the Harvard-MIT BNCT group developed a TPS for boron neutron capture therapy called MacNCTPlan. As part of preparation for the melanoma clinical trials in Argentina and subjected to the collaboration between CNEA and Harvard-MIT BNCT programs, this TPS was thoroughly benchmarked by CNEA [36]. This code was also compared by other groups [40, 93] to the BNCT_rtpe [77] and SERA [78] treatment planning systems. These studies along with the routine use of MacNCTPlan in Phase I BNCT trials at Harvard-MIT [12, 81] revealed some limitations and deficiencies of this system, principally associated with the geometry modeling technique based on the voxel reconstruction method [74].

The voxel reconstruction method or "voxel model" is a common method employed in BNCT to generate the description of the geometry that will be used for the Monte Carlo simulation. Briefly, it consists in the partitioning of the geometry described by medical images into units of regular size. Each unit, known as voxel or cell, is filled with a homogeneous material. Some investigators have studied the influence of the voxel

size and material homogenization in dosimetry calculations. As a general conclusion, a voxel size of 1 cm^3 is acceptable for clinical-like geometries. However, the voxelization process may lead to inaccurate dose estimations in surface areas. Up to now, the only proposed solution to this problem was to reduced the voxel size. The drawback is that the downsizing of the voxel considerably increases memory usage, and more importantly, execution times [40, 62].

The main objective of the present work regarding computational dosimetry is to introduce a modified analytical approach for accurately computing the material-map of the anatomical region from medical images, and to develope a novel strategy to improve the prediction within the first millimeters of the model surface without any detriment of execution times.

1.3 BNCT macrodosimetry: other important topics

As in other forms of radiotherapy, the eventual success of the Boron Neutron Capture Therapy is associated with the ability of delivering high doses to the tumors while sparing surrounding normal tissues. To achieve this goal, this radiotherapy takes advantage of the high LET products of the $^{10}B(n,\alpha)^{7}Li$ reaction, and the preferential boron uptake by tumor cells [2, 20].

In the BNCT clinical trials currently underway, boron dose is evaluated assuming a homogeneous distribution of the boron atoms in the different parts of the tissues of interest and in the different sub-cellular structures. It is recognized that this is an important operational assumption, but no alternative approach is nowadays possible [49]. Boron concentration in peripheral blood is the only measurable quantity during patient treatment. The tissue boron concentration is then derived from tissue-to-blood ^{10}B concentration ratios previously obtained for different tissues from animal experiments and patient observations [11, 18, 24, 31, 64, 69]. In these kinetic studies, biopsy specimens are resected for boron analysis after the boron compound administration, and in some cases, surgery

must be performed to obtain tissue samples. This technique of estimating the tissue-to-blood ratios is the most natural and direct. However, it is costly, time-consuming, and in the case of human studies, invasive for the patients.

In BNCT clinical trials mediated by the administration of BPA-F complex, the estimate of the boron concentration in tumor relies on the assumption that its level can be described as a *single static* ratio. Some authors have reported that *static* tissue-to-blood uptake ratios do not completely reflect the dynamic ^{10}B loading and washout behavior expected in tumor and normal tissues [55]. However, Fukuda *et al.* [31] measured skin-to-blood and tumor-to-blood ratios in melanoma patients, and observed a relatively constant value during 6 hours after the end of the boron compound infusion. This assumption as well as the *single value* for the ratios have been accepted and applied so far, due to the difficulty and complexity of *in vivo* quantification of the boron concentration in different tissues and volumes during the treatment.

Under this scenario, it is then usual to consider a single value of the tumor-to-blood ratio in order to compute absorbed doses and tumor control probabilities in BNCT treatments. The single value that is used in these cases is generally the arithmetic mean of some set of experimental measurements. Due to measurement uncertainties and biological diversity, a description of the tumor-to-blood ratio as a random variable would be more realistic. Since the dose depends linearly on the ratio, the computation of the expected absorbed dose as the dose corresponding to that single value of the ratio is adequate. However, a good description of the distribution of ratios is necessary to compute confidence intervals for the dose, and to describe the probability distribution of possible doses. Moreover, as observed by Culbertson *et al.* [22], the behavior of tumor control probability (TCP) with respect to the dose is highly nonlinear, which makes the computation of these probabilities from a single value of the ratio very questionable. In addition to the tumor-to-blood ratio variability, the dose inhomogeneity over the target volume may also affect the tumor control probability. In conventional radiotherapy, many efforts are made

to deliver an almost uniform dose to tumors (i.e., the target volume should be included within the 95% isodose surface). Since under this condition the average absorbed dose is a representative dose of the target volume, most TCP models do not need to deal with large dose inhomogeneities. On the contrary, the dose distribution in BNCT varies significantly with depth, and then, the dose uniformity condition is virtually impossible to achieve, particularly in large tumor volumes [59]. For a typical BNCT treatment, the maximum and minimum values of the tumor dose distribution differ significantly (typically, more than 20%). In these cases, the average dose is generally used as a representative value. The TCP is then computed as if the dose in the tumor were uniformly equal to the average dose. This procedure can lead to very inaccurate results, as will be shown in the present work.

This thesis presents a non-invasive predictor of tumor-to-blood ^{10}B concentration based on the clinical outcome of BNCT treatments, and introduces a comprehensive framework for incorporating the variability of the tumor-to-blood ratios into the calculation of absorbed doses and $TCPs$. Furthermore, a tumor control probability model is presented in BNCT for the first time, which considers the effect of the ratio variability as well as the possible dose inhomogeneity over tumor volumes.

1.4 Objectives

Boron Neutron Capture Therapy is a form of radiotherapy that poses a unique challenge for optimizing the treatment of each individual patient. Since the radiation dose field combines high and low-LET radiation acting on different length scales, detailed three dimensional dosimetry calculations as well as tumor control probabilities estimations are significantly more complicated than in conventional external beam radiotherapy. This thesis aims to contribute to the knowledge in this field, presenting practical and theoretical developments on the computational modeling for treatment planning calculations, and also, a methodology for calculating absorbed doses and tumor control probabilities under

conditions of variable tumor-to-blood ratios and inhomogeneous tumor doses.

1.5 Organization

This work is organized in the following manner. Chapter 2 reviews concepts on computational dosimetry and Monte Carlo methods for radiation transport, and describes the physical and mathematical principles, architecture and operation of the MacNCTPlan Treatment Planning System. Techniques towards *in vivo* boron quantification are also discussed.

In Chapters 3 and 4, a detailed analysis of the performance of the voxel reconstruction method for a fixed voxel size of 1 cm^3 is carried out. Chapter 3 introduces the limitations of the MacNCTPlan geometry modeling technique and presents a new algorithm for the voxel model, named NCTPlan voxel model. The verification and clinical validation that provides details of the algorithm's accuracy and demonstrate its clinical usability are also described in this chapter. These procedures are conducted using both numerical and experimental standard reference tests. Chapter 4 presents a theoretical analysis of the voxel method on surface boundary regions and proposes a novel strategy to improve the prediction within the first millimeters of the model surface without any detriment of execution times.

Chapter 5 reports on the first skin melanoma treatments performed at the RA-6 BNCT facility. Results of those treatments that are specifically used in the following chapters are described in detail. Since clinical trials involved different areas of preparation, the main foci of beam design, physical dosimetry, and treatment planning approach are discussed, including a description of the BNCT procedure in Argentina. In Chapter 6, a new approach to determining the tumor-to-blood ^{10}B concentration ratio is presented. It consists of a maximum likelihood estimation from the clinical outcome of a BNCT treatment. The method is applied to the first skin melanoma BNCT treatment performed in Argentina, and the results are compared to experimental data. A comprehensive frame-

work for incorporating the variability of the tumor-to-blood ratios into the calculation of absorbed doses and TCP in BNCT treatments is described in Chapter 7. Also, a tumor control probability model is presented, which considers the effect of the ratio variability as well as the possible dose inhomogeneity throughout the tumor volume. The introduced concepts are applied to cases of malignant melanomas, and are illustrated in the first BNCT treatments of skin melanoma carried out in Argentina. Conclusions and future investigations are presented in Chapter 8.

A list of acronyms is provided in Appendix A. Auxiliary computations and numerical simulations related to Chapter 4 are described in Appendices B and C, respectively. Appendix D provides mathematical developments for Chapter 7.

Chapter 2

Background

2.1 Computational dosimetry and treatment planning

As mentioned in Chapter 1, BNCT is a complex form of radiotherapy since the mixed dose field of high and low-LET radiation acts on different length scales ranging from a few microns to various centimeters. Thus, dosimetry calculations are significantly more complicated than for conventional radiotherapy approaches.

The mathematical description of the transport of neutrons through matter comprises the solution of the integrodifferential form of the transport equation. Although this equation provides the exact description of the particle density in the phase space, it is virtually impossible to find an explicit solution even for relatively simple geometries. The complexity of the problem usually demands to use deterministic transport methods solved by numerical techniques (e.g., discrete-ordinates method), or statistical simulation methods (e.g., Monte Carlo) [27].

Among the discretization techniques used historically in neutron transport modeling, mesh representations and homogenization methods provided satisfactory solutions, but with an unavoidable loss of fine-scale information [73, 74]. However, it will be shown

in subsequent chapters that the degree of accuracy of these methods can be improved if physical and geometrical information is appropriately managed in the generation of the model.

Treatment planning systems (TPS) based on Monte Carlo methods appeared as the principal candidate tool in BNCT [57, 77, 78, 94, 95]. Monte Carlo calculations allow treating the complex radiation transport problem accurately, tracking millions of particles and computing each dose component. Currently, there are several developments of planning codes either based on Monte Carlo or deterministic methods [16, 37, 53, 57, 60, 62, 78, 83, 90]. However, only a few of these systems have been used clinically in the USA, Europe, Argentina and Japan, and all of them are Monte Carlo-based codes: 1) MacNCTPlan [57, 94], and its successor NCTPlan [37], developed by CNEA (Argentina) and the Beth Israel Deaconess Medical Center (USA), 2) BNCT_rtpe [77], and its successor SERA [78], developed by Idaho National Energy and Engineering Laboratory in collaboration with Montana State University (USA), and 3) JCDS [62], developed by Japan Atomic Energy Research Institute (JAERI).

As part of the preparation for melanoma clinical trials in Argentina, the MacNCTPlan TPS was thoroughly benchmarked by the CNEA Treatment Planning Group in 1999 [36]. This code was also compared by other groups to the BNCT_Rtpe [40] and SERA treatment planning systems [93]. In short, the result of these studies and the routine use of MacNCTPlan in Phase I BNCT trials at Harvard-MIT [12, 81], revealed some limitations and deficiencies of the this system, principally associated with the geometry modeling technique, thus motivating new developments on the computational model for treatment planning calculations.

This section describes the physical and mathematical principles, architecture and operation of the Monte Carlo-based treatment planning system MacNCTPlan for the computational macrodosimetry in BNCT. Since the Monte Carlo engine utilized by MacNCTPlan is the general-purpose Monte Carlo N-Particle code MCNP [8], a brief discussion of the

Monte Carlo method as well as MCNP code is also included.

2.1.1 Monte Carlo Method for radiation transport and MCNP

The Monte Carlo method is simply a numerical method that can be used to duplicate theoretically a statistical process such as the interaction of nuclear particles with materials. In particle transport, the Monte Carlo technique is a theoretical experiment that consists of actually following each of many particles from a source throughout its life to its death in some terminal category, i.e. absorption, escape, etc. The individual probabilistic events that comprise a process are simulated sequentially. The statistical sampling process is based on the selection of random numbers, and probability distributions governing events are randomly sampled using transport data to determine the outcome at each step of the particle life [8].

By contrast to deterministic transport methods, Monte Carlo does not solve an explicit equation, but rather obtains answers by simulating individual particles and recording some aspects (tallies) of their average behavior. The average behavior of particles in the physical system is then inferred (using the central limit theorem) from the average behavior of the simulated particles. Monte Carlo in radiation transport can be described as follows. Initially, the computer code randomly select the initial particle position and velocity vector based on information about the user-supplied particle source. The source model is generally described by spatial, energy and angular distributions (e.g., the case of the hyperthermal RA-6 beam at the reactor port). Next, numbers between 0 and 1 are selected randomly to determine what (if any) and where interaction takes place, based on the rules (physics) and probabilities (transport data) governing the processes and materials involved. For example, if a neutron collision occurs as a first event, the neutron is scattered in a direction selected randomly from the physical scattering distribution. If a photon is also produced, then it is temporarily stored, or banked, for later analysis. When a capture or fission reaction occurs as a second event, the incoming particle is no

longer tracked, thus resulting in the termination of the neutron history and the birth of two or more outgoing particles. Stored particles are retrieved from the bank in such a way that the last particle stored in the bank is the first particle taken out. The tracking of a particle is ended if it is captured or escapes out of the defined geometry. If enough particles are tracked in this way, estimates of particle flux in a given region of space can be computed, which then can be modified by fluence-to-dose conversion factors (i.e., kerma factors [1]) to produce estimates of dose.

MCNP is a general-purpose Monte Carlo code that has the ability to transport neutron, photon, electron, or coupled neutron/photon/electron fields through an arbitrary three-dimensional configuration of materials in geometric cells bounded by first- and second-degree surfaces and fourth-degree elliptical tori. It uses continuous-energy nuclear and atomic data libraries. For neutrons, all reactions given in a particular cross section evaluation (such as ENDF/B [86] and ENDL [48]) are accounted for. Thermal neutrons are described by both the free gas and thermal scattering $S(\alpha, \beta)$ models. For photons, the code takes account of incoherent and coherent scattering, the possibility of fluorescent emission after photoelectric absorption, absorption in pair production with local emission of annihilation radiation, and bremsstrahlung. A continuous-slowing-down model is used for electron transport that includes positrons, k x-rays, and bremsstrahlung but does not include external or self-induced fields [8].

The first version of MCNP was released by Los Alamos National Laboratory in 1963 as a natural consequence and extension of Enrico Fermi's work done pre and during World War II. Currently, it represents over 45 years and 500 person-years of development at Los Alamos. There are over 3000 active user of MCNP spread all over the world. By virtue of it various implementations along with its continual development, MCNP is a well-benchmarked code extensively validated against experimental data, with a broad scope and far-reaching functionality. As such, it was considered a powerful computational tool for applications to BNCT both in the areas of patient dosimetry and neutron beam design.

2.1.2 MacNCTPlan Treatment Planning System

As previously described, MCNP was conceived to handle a broad range of calculations and it provides the user almost complete control over various input parameters such as particle source, geometry modeling, cross-section data, etc. To describe the shape of the three-dimensional regions through which the particles are to be transported, MCNP utilize user-defined materials in geometric cells bounded by planes, cylinders, ellipsoids, etc. These surfaces are defined by supplying coefficients to their analytic equations or, for certain types of surfaces, known points belonging to them. Cells are then described as the intersections, unions, and complements of the regions bounded by the surfaces.

Although MCNP gives the user the flexibility of defining geometrical regions from all the first and second degree surfaces of analytical geometry and elliptical tori, and combining them with Boolean operators, it is very difficult to accurately describe the human anatomical structures with these simple surfaces. In an effort to model the patient geometry as accurate as possible for BNCT calculations using MCNP, Zamenhof *et al.* [94] proposed for the first time to use a mesh or voxel representation of the patient geometry created from medical images. Thus, in 1996 they introduced the first version of the Monte Carlo-based treatment planning system for boron neutron capture therapy, called NCTPlan [94], based on the voxel reconstruction technique coupled to the general-purpose Monte Carlo code MCNP. The original version of the NCTPlan code, written in FORTRAN on a VAX platform under the VMS operating system, was used to plan irradiations for four subjects who completed a Phase I BNCT protocol for melanoma of the extremities at Harvard-MIT [43]. Owing to the experience gained in its use, a number of limitations were identified which led in 1997 the Harvard-MIT program to rewrite the code in a Power Macintosh platform using Pascal units nested within the image processing code NIH-image [57, 95]. The new version of the code, called Macintosh Neutron Capture Therapy Plan (MacNCTPlan), was extensively used to plan irradiations for glioblastoma multiforme (GBM) and melanoma patients at Harvard-MIT [95, 81], and also for GBM

patients at Rez, Czech Republic [10]. What follows describes in detail the concepts and design of the code.

Geometry modeling technique

The reconstruction technique that is used by the MacNCTPlan system to create the Monte Carlo model is based on the voxel reconstruction method. This method uses the information provided from a set of computed tomography (CT) scans of the subject´s relevant body part, typically acquired as 125 contiguous 2 mm images from a helicoidal CT scanner.

In this technique, each plane of medical image data is partitioned into squares of regular size before being mathematically stacked to construct a large three-dimensional array of $21 \times 21 \times 25$ cells (or voxels) of 1 cm^3 each. In order to assign an homogeneous mixed material in a single voxel, the four primary material types, i.e. air, bone, and both tumor and normal tissue (soft tissues), are averaged by volume. The image segmentation into these primary materials is carried out applying a thresholding process. From a large region of interest containing areas of contiguous normal tissue, bone and air, a Hounsfield Unit (H) frequency histogram is constructed. Based on the threshold H values selected from the frequency histogram and tumor volume outlines drawn by the user, the algorithm of the voxel method examines every pixel of each CT image, and automatically assigns the corresponding material type to each one. Although tumor and normal tissues are differentiated according the tumor outlines, both tissues are assumed to have the same elemental composition the only difference being the ^{10}B content. The number of pixels contributing to a single cell depends on the in-plane pixel dimensions and the image width. For typical values of these parameters (about 1 mm and 2 mm, respectively), 500 to 1000 pixels contribute to a 1 cm^3 cell. Thus, the number of pixels of a specific material type will give the proportion of that primary material in a cell. The composite admixtures of tumor, normal tissue, bone and air characterizing each of these cells are

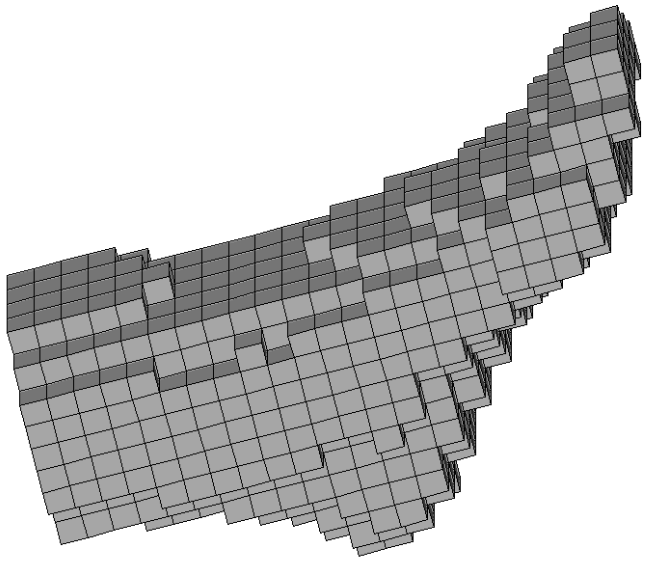

Figure 2.1: Voxel model of a lower part of the leg and foot.

defined as "mixed materials". To avoid the large number of different mixed materials that can result from this process (for example, with 500 pixels and four primary materials there are approximately 21 million possible combinations), the algorithm rounds the proportion of each primary material off to the nearest 20% volume increment. In this way, the number of possible mixed materials for each 1 cm^3 cell is reduced to 56.

Figure 2.1 shows an example of the voxel model for a lower part of a leg and foot. The final result of the voxel reconstruction method is a heterogeneous multi-material mathematical model, consisting of 11025 cells enclosed in a parallelepiped box (in example, cells containing air are not shown). This array is ready for downloading into the Monte Carlo simulation code. MacNCTPlan graphical interface allows the user to examine the voxelized model, indicating the material mixture assigned to every cell.

Particle transport simulation and dose determination

In MCNP runs, one of the parameters to define the particle source is the beam direction. In MacNCTPlan TPS this is carried out selecting the entrance and exit points of the beam on a graphical window that displays, simultaneously, two orthogonal slices through the CT image set.

When the voxel model of the anatomical body part has been computed, information regarding the description of materials and selection of cross section evaluations, the location and characteristics of the neutron and photon sources, and the type of answers or tallies desired must be supplied into the MCNP input deck file. Since this file has a specific format, all the data is converted into the standard format required by MCNP code using a FORTRAN program called MPREP.

As mentioned in section 1.2, BNCT demands the use of both neutron and photon sources. Then, two separate simulations are required because MCNP can only start one type of particle per simulation. In the case of neutron transport simulation, photon production by neutron interactions is handled by a photon production segment of a cross section file. Among the eight classes of nuclear data tables that exist for MCNP, continuous-energy neutron interaction data, photon interaction data, and $S(\alpha, \beta)$ neutron thermal data are used in BNCT problems. The continuous-energy data tables provides a grid that is sufficiently dense that linear-linear interpolation between points reproduces the evaluated cross sections within a specified tolerance that is generally 1% or less. To account for the molecular binding effects of hydrogen in biological materials such as those present in BNCT, the $S(\alpha, \beta)$ thermal neutron scattering treatment for hydrogen in light water at 300 K is used. This treatment is of critical importance in modeling neutron thermalization since at neutron energies below several eV, the neutron energy is comparable to the thermal energy of the target atom as well as to its chemical binding energy. Then, while the thermal motion of the target alters the effective scattering cross section and the energy transfer to or from the incident neutron, the chemical binding affects the recoil of

the target nucleus and thus influences the energy and angle of the outgoing neutron.

The tissue elemental composition of the primary materials used for particle transport are taken from the ICRU 44 and 46 reports [50, 51], and in the case of air, from the composition described by Chadwick *et al.* [17]. When treatments plans are computed for the head, tumor and normal soft tissue are both assumed to have the elemental composition of adult whole brain, and bone, the elemental composition of skeleton-cranium. When treatment plans are computed for other regions such as legs, tumor and normal soft tissue are assumed to have the adult muscle composition, and bone, the adult femur composition.

As described above, tumor and normal tissues are differentiated according to their ^{10}B content. The explicit inclusion of the ^{10}B in the Monte Carlo model influences the radiation transport, accounting for the depression of the thermal neutron flux and its natural effect on the ^{10}B and thermal neutron dose components.

MCNP allows for particle sources of various shapes with a variety of energy, position and angular distributions. However, in order to avoid geometry errors, the source specification in MacNCTPlan is limited to a distribution on a plane surface from which particles are started. Typically, this distribution is represented by spatial, angular and energy coupled probability distributions, and corresponds to the neutrons (or photons) coming out the reactor at the beam port. The source modeling demands multiple Monte Carlo runs simulating the reactor core and the surrounding structures, and a subsequent transport of neutrons and photons through the filter elements of the beam line.

For purposes of BNCT, MCNP is used to produce estimates of the particle flux in a cell by calculating the track lengths per unit time and volume in that region (F4 tally type) [8, 15]. To compute dose-rate values in every cell of the voxel representation, the particle flux tallies are modified by energy-dependent response functions which convert the average flux in a cell to the average dose rate for a given material either explicitly or implicitly specified in the model. As described in ICRU Report 63 [52], these response functions

for neutrons and photons are the fluence-to-kerma coefficients that account for the initial kinetic energy of all those primary charged particles released by uncharged particles. Once the average flux or dose in a cell is computed, it is assigned to the geometrical center of the voxel. The coarse flux/dose matrix that result from this procedure is then used to interpolate data in all the volume.

Dose calculations in the voxel model are performed with the assumption that charged particle equilibrium (CPE) conditions are satisfied everywhere in the geometry [1]. Under this assumption, dose is approximated by kerma. For the 1 cm^3 voxels, the CPE condition is readily fulfilled for neutrons of low to moderate energies such as those present in a typical BNCT beam. In the case of photons, CPE condition does not hold for interfaces (i.e., build-up regions), and the actual dose delivered is lower than the corresponding kerma value [1]. Nevertheless, with the assumption of CPE, the photon dose in the first few millimeters of tissue close to the interface with air will be overestimated by the simulation, which in a sense constitutes a conservative position in terms of normal tissue dose tolerance.

The neutron kerma factors usually used in BNCT are calculated from the kerma data in ICRU Report 63 and JENDL-3.2 cross sections and reaction Q-values [52, 75]. On the other hand, photon kerma factors are based on mass energy absorption coefficients (μ_{en}/ρ) reported by Hubbell and Seltzer [47] as part of the NIST data. Kerma factors for ^{10}B are calculated from the ENDF/B-VI library for the $^{10}\mathrm{B}(\mathrm{n},\alpha)^{7}\mathrm{Li}$ and $^{10}\mathrm{B}(\mathrm{n},\alpha)^{7}\mathrm{Li}^{*}$ reactions which dominate at thermal energies. Although there are other reactions that may represent a significant fraction of the total boron kerma at energies above several hundred keV, their impact on the total dose from the ^{10}B is negligible due to the very low absolute value of the kerma factors in this energy range [41]. Through the use of the energy tally card and the appropriate neutron kerma factors, MCNP estimates physical doses that result from thermal and fast neutrons (i.e., thermal and fast neutron doses), which then may be multiplied by their corresponding RBE values to obtain the photon-equivalent

BNCT dose. Regarding the boron dose, a specified explicit bulk of ^{10}B is included in the patient model as a first-order correction for thermal neutron flux depression. However, MCNP computes this dose normalized to 1 ppm of ^{10}B in the material. The reason of this approach is that the average ^{10}B concentrations in tumor and normal tissue in each patient will likely differ from the bulk concentration guessed for the model. Thus, the normalized dose is finally multiplied by the correct value of boron concentration.

For a typical BNCT treatment plan, 10 million particle histories are tracked per run to compute a single beam orientation. This derives statistical uncertainties of less than 3% for high- and low-dose regions. The process of photon and coupled neutron-photon fields takes approximately 2 h on a 2.4 GHz Pentium IV processor with 512 MB RAM. This execution time is achieved using a modified version of MCNP4B, and it can be reduced if calculations are processed on a cluster of computers [39].

Display of results

The MCNP output files resulting from the Monte Carlo simulations are imported back into MacNCTPlan TPS to graphically display the results. MacNCTPlan can generate one dimensional dose profiles along any arbitrary plane, two dimensional isodose contours overlaid on CT images, and other figures of merit such as cumulative dose-volume histograms (DVH). Since for each simulation, flux-to-kerma conversion factors are specified for one explicit tissue (e.g., muscle), the 3D dose distribution for all the geometry will correspond to dose values for that tissue, even if the dose location happens to correspond to another tissue or a mixture one. Then, it is common to have a set of isodose contour plots corresponding to different tissues. Figure 2.2 shows a typical graphical view of the dose isocontours overlaid on top of two orthogonal planes of the original medical images. In this example, the dose distribution corresponds to normal tissue and thus, it would be useful to produce a treatment plan that spares important tissues.

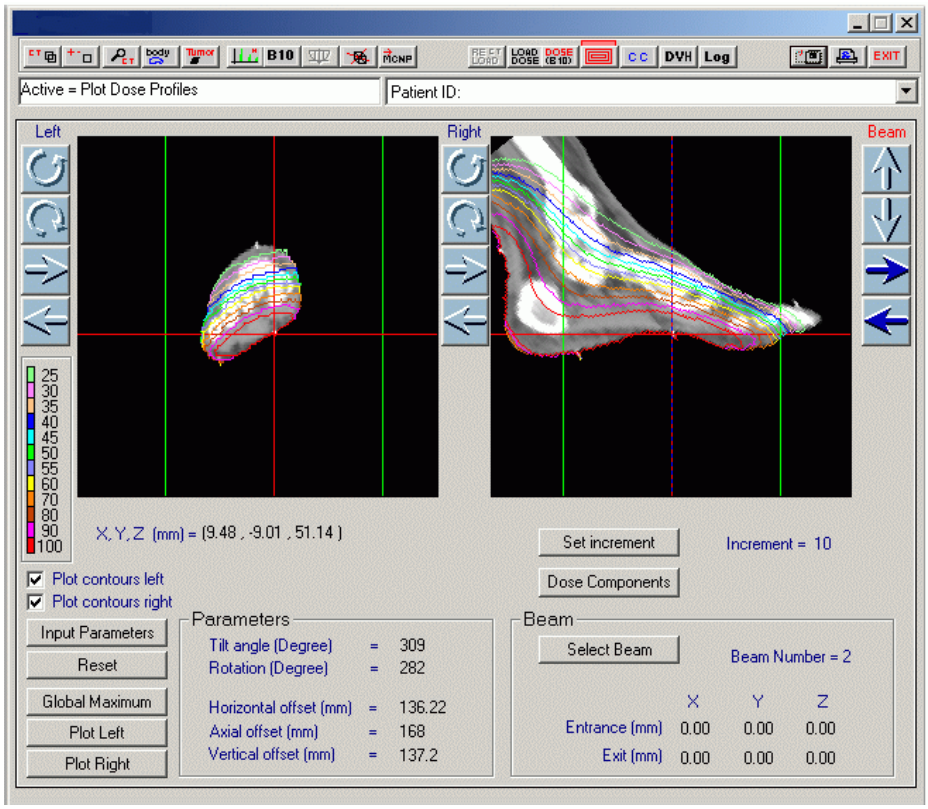

Figure 2.2: Normal tissue dose isocontours overlaid on top of two orthogonal planes through the CT image set.

2.2 *In vivo* boron quantification methods

In the BNCT clinical trials currently underway, boron dose cannot be measured in patients or phantoms. For treatment purposes, this component is then computed assuming a homogeneous distribution of the boron atoms in the different parts of the tissues of interest and in the different sub-cellular structures. As mentioned before, the tissue boron concentration is derived from tissue-to-blood ^{10}B concentration ratios previously obtained from experiments, and pharmacokinetic models which allow to describe the temporal ^{10}B distribution in blood [55]. Since blood and biopsy specimens are required for boron analysis after the boron compound administration, and in some cases, surgery must be performed to obtain tissue samples, this technique is considered invasive for patients and therefore,

it is not frequently applied.

During the last years, much effort has been done in development of noninvasive *in vivo* macroscopic boron quantification. Among the quantitative techniques potentially useful for *in vivo* boron determination are nuclear magnetic resonance (NMR), the positron emission tomography (PET), and prompt gamma neutron activation analysis (PGNAA). This section briefly presents these techniques.

2.2.1 Nuclear magnetic resonance

NMR has been studied to direct detect boron. In clinical BNCT trials, the boron compound is 98% isotopically enriched in ^{10}B. This isotope has a large quadrupole moment that produces a large line broadening in NMR, with a relative NMR sensitivity of 0.02 compared to ^{1}H [96]. Due to this condition, the signal is very poor compared to the noise and thus, ^{10}B has to be detected by nonconventional NMR techniques. Such is the case of the proton-boron double-resonance approach [3], but due to its complicated experimental operation and high sensitivity to motion artifacts, potential clinical application has been hindered. An alternative approach to the detection of boron is to use ^{11}B compounds. The measurement of boronated agents BSH (sulfhydryl borone) and BPA containing naturally occurring boron has been successfully demonstrated [96]. However, if the boron delivery agents employed in clinic are to be used, this method would have insufficient sensitivity to be useful.

A different approach that has been explored with NMR is to the detect the protons associated with the ^{10}B carrier molecule (e.g., BPA) rather than to direct detect boron [96]. Preliminary results in blood samples and *in vivo* brain tissues of patients suggest that proton NMR would be a useful technique for noninvasive *in vivo* measurements in clinical BNCT.

2.2.2 Positron emission tomography

PET has been used to clinically investigate uptake of fluorine-18 labeled BPA fructose in brain tumors [76]. This technique assumes that ^{18}F-BPA mimics BPA *in vivo* based on a number of animal experiments. Its principle is based on the annihilation of positrons and electrons, resulting in two gamma rays which fly off in opposite directions. Counters set up around the patient detect the emitted gamma rays. Gamma rays arriving at the same time at the counters come from the same point in the body. Advanced computer software programs are then used to generate a detailed image of the part of the body being examined. All positron emitters are short-lived, from two minutes to a few hours, so the PET scanner have to be stationed close to where the radioisotope is produced, i.e. in the neighborhoods of a cyclotron. The spatial resolution achieved with this technique for boron quantification is about 6.5 mm in plane and 7 mm in depth [76]. Although the assumption of biokinetic compatibility of ^{18}F-BPA and BPA needs further validation, the PET technique is very attractive for *in vivo* measuring the dynamic spatial distribution of BPA.

2.2.3 Prompt gamma neutron activation analysis

PGNAA is often used to measure ^{10}B content in blood samples during the irradiation of patients. It uses the thermal or epithermal neutrons that come from the reactor to measure the flux of prompt gammas induced in the irradiated sample by $^{10}\mathrm{B}(\mathrm{n},\alpha)^{7}\mathrm{Li}$ and $^{1}\mathrm{H}(\mathrm{n},\gamma)^{2}\mathrm{H}$ reactions. The ratio of the boron to hydrogen count rates is used for boron quantification. Based on this technique, Verbakel *et al.* has developed the so called gamma-ray telescope to detect the gamma rays that are produced in tissue during the patient irradiation [91]. In this technique, locally measured gamma-ray emission rates from the boron and hydrogen have to be combined with the distribution of thermal neutrons inside the anatomy. Recently, this approach has been applied in GBM patients for sulfhydryl borane (BSH)-mediated BNCT, to measure and reconstruct boron concentra-

tions in different regions of the head. Since the boron gamma-ray measurement can be related directly to the local boron dose averaged over the field of view, it is believed that the gamma-ray telescope can be used as an *in vivo* dosimetry system for determination of the boron dose [91]. The spatial resolution of this technique is about 1.6 cm. A smaller collimator diameter would provide a higher resolution at the cost of efficiency, though.

Chapter 3

NCTPlan voxel model: verification and clinical validation

3.1 Introduction

The reconstruction technique that is used by the MacNCTPlan system to create the Monte Carlo model is based on the voxel reconstruction method (see section 2.1.2). As a common method employed in different TPS for BNCT, it was the subject of study in various published works, in which the influence of the voxel size and material mixing was assessed using standard simulation tests as reference data [40, 41, 93]. The first study carried out by Goorley *et al.* [40] demonstrated close agreement between the MacNCTPlan and BNCT_rtpe codes in evaluating a single clinical BNCT test case. However, Wojnecki and Green [93] reported that the spatial resolution of 1 cm^3 used by the voxel reconstruction technique in MacNCTPlan TPS may lead to differences of up to 20% in the thermal neutron fluence along the central beam line, for a rectangular phantom irradiated through one of its sharp edges.

In view of the results just mentioned, the MacNCTPlan voxel model was thoroughly benchmarked by CNEA [36]. In this process, some limitations and deficiencies were iden-

tified which motivated the development of an improved voxelization algorithm together with a detailed analysis of the performance of the voxel reconstruction method for a fixed voxel size of 1 cm^3. This chapter mainly focuses on the new algorithm for the voxel model. Since this new algorithm was implemented in MacNCTPlan's successor, the Neutron Capture Therapy Plan (NCTPlan) program [37], it will be referred to as "NCTPlan voxel model".

As in conventional radiotherapy, a thorough evaluation of the algorithms involved in dosimetry calculations is required for safe and accurate delivery of doses in BNCT. In order to provide a detailed insight into the accuracy of the new algorithm and demonstrate its clinical usability, a number of test were conducted as part of the verification and validation processes. In this chapter, a set of numerical test problems is presented. With the aim of assessing the accuracy of the model in a clinical-like case, results of a comparison between the in-phantom experimental dosimetry performed at the RA-6 BNCT facility [5, 7] and the corresponding computational dosimetry calculations are also presented.

3.2 Voxel model

3.2.1 MacNCTPlan material assignment model

In section 2.1.2, the geometry modeling technique used by MacNCTPlan to create the Monte Carlo model from CT medical images was introduced. It is based on the voxel reconstruction method that assigns an homogeneous mixed material to every single cell of the $21 \times 21 \times 25$ cm^3 three-dimensional array. To make the total number of mixed materials computationally manageable, the algorithm rounds the proportion of each primary material to the nearest 20% volume increment. If a material's proportion is an odd multiple of ten, the proportion is rounded up.

This rounding procedure does not guarantee that the total percentage of each cell adds up to 100%. For example, a cell composed of 12% air, 15% normal tissue and 73% bone

is rounded to 20% air, 20% normal tissue and 80% bone. Therefore, the final percentages of the three materials types together add up 120%. In addition to this example, there are cases in which rounded percentages add up 80% or 140%, instead of 100%. Since an admissible mixture should total 100%, a decision needs to be taken in these cases.

The original strategy followed by the MacNCTPlan voxel reconstruction algorithm can be summarized as follows. For each voxel, the algorithm computes the real proportions of the four primary material types in it (i.e., air, bone, tumor and normal tissue) from CT images, and rounds each proportion to a 20% volume increment. If the rounded percentages sum to 100%, they are assigned to the current voxel. If not, the algorithm assigns the previous voxel's material mixture to the current cell. Clearly, this approach can lead to serious errors in the material model.

3.2.2 NCTPlan material assignment model

General description

The strategy followed by the NCTPlan voxel reconstruction algorithm is based on the search for an "*admissible mixture*" that minimizes the following expression:

$$\sum_{i=1}^{4} \left| \frac{X_i^{\text{real}} - X_i^{\text{rounded}}}{X_i^{\text{real}}} \right|, \tag{3.1}$$

where X_i^{real} and X_i^{rounded} are the real and rounded proportions of primary material type i, respectively. This expression represents the sum of the absolute values of the relative material percentage differences.

When the set of X_i^{rounded} are the nearest rounded percentages, expression (3.1) is minimized, and the algorithm tries this configuration as its first choice. If this configuration is not an admissible mixture assignment (i.e., the rounded percentages do not sum to 100%), the algorithm adjusts the rounded percentages subject to the following criteria: (a) the original rounded percentage for air (i.e., the nearest rounded value) will not be changed since it is desirable to leave unchanged the material considered most dissimilar

in terms of affecting particle transport, and (b) if a real proportion of a material is zero, this material will not be created since it would be unnatural to introduce a material into a cell where it is not actually present.

In case of configurations summing 80%, one of the percentages that was rounded down needs to be rounded up. To decide which percentage should be adjusted, the algorithm rounds up each material percentage one at a time and computes expression (3.1) for each new configuration. If the minimum of (3.1) is unique, the algorithm selects the configuration that leads to this minimum. Otherwise, the algorithm selects the configuration that affects particle transport least (among configurations giving the same minimum).

The procedure explained above is analogous for the case of 120%, but rounding percentages down instead of rounding up. In cases of 140%, the algorithm proceeds rounding down two material percentages at a time and computing expression (3.1) likewise.

At this point, it may be argued whether changing one material at a time (or 2 in cases of 140%) will always lead to the best admissible configuration. In other words, could a better configuration be obtained by changing two or more percentages simultaneously? The answer is simple if it is noticed that for the nearest rounded percentages, expression (3.1) is minimum. In fact, the nearest rounded percentages minimize each term of (3.1). Therefore, any change made to one of these values will increase the sum of the relative differences, no matter what it is done to the other materials. If two percentages are changed simultaneously, the corresponding terms in (3.1) will increase and so the sum will increase, too. Thus, the fewer changes made, the better.

Physical considerations

It was mentioned above that in case two or more configurations give the same minimum, the algorithm will choose the configuration that affects particle transport least. The strategy followed is to evaluate which material percentage is more convenient to adjust in terms of reaction rates, i.e. to keep the macroscopic cross section as close as possible to

the real case. Among all the nuclides composing the 4 primary material types, hydrogen (H) and nitrogen (N) are the two most important for neutron transport. While nitrogen mainly contributes to neutron capture reactions ($^{14}\mathrm{N}(\mathrm{n},\mathrm{p})^{14}\mathrm{C}$), hydrogen contributes to both neutron capture and scattering reactions ($^{1}\mathrm{H}(\mathrm{n},\gamma)^{2}\mathrm{H}$, $^{1}\mathrm{H}(\mathrm{n},\mathrm{n}')^{1}\mathrm{H}$). In addition, since $^{10}\mathrm{B}$ is explicitly included in the Monte Carlo model because of its high neutron capture cross section, it is also considered in the strategy.

The reaction rate density $\dot{r}$ for a given element x and specific reaction j is

$$\dot{r}_j^x \left[\frac{\text{reactions}}{\text{cm}^3 s}\right] = \Sigma_j^x \phi, \tag{3.2}$$

where Σ_j^x is the macroscopic cross section , and ϕ the neutron flux. When reaction rates for all elements of a material type are combined by adding together the reaction rate density for each individual nuclide, the resulting value is the total number of reactions type j per unit time and volume in that material.

Considering only neutron capture reactions in hydrogen and nitrogen, the ratio of reaction rate densities between soft tissue (st) and bone (b) material types can be approximated applying (3.2) by:

$$\frac{\Sigma_c^{st}}{\Sigma_c^{b}} \simeq \frac{\left[N_H\ \sigma_c^H + N_N\ \sigma_c^N\right]^{st}}{\left[N_H\ \sigma_c^H + N_N\ \sigma_c^N\right]^{b}}, \tag{3.3}$$

where N_H and N_N are the number of H or N nuclei per unit volume of soft tissue or bone, and σ_c is the capture microscopic cross section for each element.

If expression (3.3) is evaluated for adult brain-to-adult skeleton-cranium and adult muscle-to-adult femur, using ICRU 46 material compositions [51], both ratios result in values greater than one. That means the number of reactions per unit time and volume in soft tissue is greater than that in bone (by $\sim 10\%$). Therefore, if only capture reactions in hydrogen and nitrogen were considered in the analysis, the algorithm's strategy should adjust the bone percentage and maintain the original rounded soft tissue percentage.

Now consider boron neutron capture and neutron scattering reactions. The first reaction is due to the presence of $^{10}\mathrm{B}$ in tissues, and consequently, the number of boron

capture reactions will be proportional to boron concentration. Since ^{10}B is not added to bone, there are no boron capture reactions to consider in this material. On the other hand, neutron scattering reactions are mainly due to the presence of hydrogen in tissues. Again, since soft tissue hydrogen content is greater than that of bone, scattering reactions in tissue will be greater than in bone. Therefore, taking into account all the reactions of interest in this analysis, it will be advantageous to adjust bone percentage and maintain the soft tissue original rounded proportion.

The previous analysis was done for the case in which the algorithm must decide to adjust percentages of soft tissue or bone. Which should be the strategy followed by the algorithm when normal and tumor tissues are compared? Since tumor and normal tissues are assumed to have the same elemental composition but a different ^{10}B concentration, the difference in their reaction rate densities will depend on tumor-to-normal ^{10}B ratio (see section 2.1.2). Typically, a ratio of 3.5 is assumed in clinical treatments [20]. Hence, the boron reaction rate density in tumor will result 3.5 times greater than that in normal tissue, and therefore the algorithm should decide to adjust the percentage of the latter.

To summarize the final algorithm's strategy for inadmissible mixtures, bone percentage is adjusted over soft tissue, and normal tissue is adjusted over tumor.

3.3 Verification of NCTPlan algorithm: MCNP Numerical test problems

Recent efforts in physical dosimetry standardization have used two different water phantom geometries: a simple rectangular phantom [44], and an ellipsoidal head phantom based on the Snyder model [89]. While the parallelepiped phantom is a simple medium to test Monte Carlo calculations, the ellipsoidal phantom provides a more realistic model, with its curved surfaces and heterogeneous composition.

The numerical test problems carried out to compare and verify the NCTPlan voxel

model are based in these two geometries. The following describes each reference problem in detail.

3.3.1 Parallelepiped phantom

Wojnecki and Green [93] have studied the performance of the MacNCTPlan voxel model for a parallelepiped phantom irradiated with monoenergetic and monodirectional neutron beams of 5 cm radius. This performance was assessed comparing thermal neutron fluences along the beam axis against the data derived for the exact geometry modelled by the reference computational tool MCNP. In order to evaluate the performance of the NCTPlan reconstruction algorithm and compare it with the older version, it was subjected to the same standard tests as those introduced in Wojnecki's work.

Reference problem #1

In order to reproduce Wojnecki's tests, a water-filled rectangular phantom of $14 \times 15 \times 19$ cm^3 and 8-mm- polymethyl-methacrylate walls was used in the simulations. Two different positions of the parallelepiped phantom with respect to the particle source were evaluated (referred to as "parallel" and "angular" positions). In the first case, particles are perpendicularly directed onto one face of the phantom while in the angular case, particles bombard one of its edges. Note that in the case of the angular position, the CT images of the phantom are rotated with respect to the parallel position and this leads to a different material model of the same geometry. All simulations were carried out for a 5 keV monodirectional beam of 50 mm radius, and 10 million histories were sampled in each run. Thermal neutron fluence profiles along the beam axis were used as the figure of merit for the comparisons. In the case of voxel models, the tally volume coincides with the volume of the homogenized cells, which is 1 cm^3. On the other hand, reference data were computed for a different tally volume: in a cylinder of 2 mm diameter and 1 mm high (in the following referred to as "punctual" fluence). Wojnecki and Green used reference

data tallied in 1 cm^3 volume. Note, however, that the punctual estimation is a better approximation of the fluence at a point. Since the goal of this chapter is to assess the accuracy of the NCTPlan voxel model, comparisons were carried out using the punctual reference data.

Simulations #1

Clearly, the material model that results from a CT study depends on the position of the voxel grid with respect to the position of the images. Then, the computed thermal fluence along the beam axis could vary because of this reason. For the completeness of the evaluation, different positions of the voxel grid were analyzed. In the case of the parallel position, simulations were carried out for ten locations of the voxel grid, starting with a voxel edge coincident with the phantom's entrance face (position 0), and moving the edge each 1 millimeter (position 1 to position 9). Following the same procedure, ten locations of the voxel grid were also computed in the case of the angular position.

3.3.2 Snyder head phantom

The Snyder head phantom consists of two ellipsoids which divide the head into regions of cranium and adult brain. Since each region is delimited by an ellipsoidal surface, the Snyder phantom can be exactly modeled with MCNP (or MCNPX [92]) transport code.

Reference problem #2

Using the analytical model of the Snyder head phantom and the Monte Carlo transport code MCNPX, neutron and photon flux and dose-rate distribution data were obtained in a rectangular tally grid of $21 \times 21 \times 25$ cells of 1 cm^3 each. This grid, which is overlaid on top of the geometry model, allows talling particles in cells with the same volume as those constructed by the voxel method. Since tallies are performed in a mesh independent of the tracking geometry, the Snyder phantom geometry is exactly modeled.

Three material types were used in this problem: air (as surrounding material), cranium and brain. Air composition was taken from Chadwick *et al.* [17], and brain and cranium compositions - adult whole brain and adult cranium - were taken from ICRU report 46 [51]. Kerma factors for brain tissue and ^{10}B reported in Ref. [41] were used to compute absorbed dose rates.

Monodirectional neutron and photon source beams, sampled uniformly in a disk of 20 cm in diameter, were used for the dosimetry calculations. The neutron source energy spectrum, which was primarily epithermal, was described by three energy distributions. In the thermal range (10^{-3} to 10^{-1} eV), neutron energies are sampled from a Maxwell distribution centered at 0.025 eV with a 10% relative intensity. The epithermal and fast components (10^{-1} to 10 keV and 10 keV to 2 MeV), assigned 89% and 1 % of relative intensities respectively, were sampled from 1/E energy distributions. Three energy peaks corresponding to 80 keV, 511 keV and 2.2 MeV describe the photon energy spectrum, with relative intensities of 5%, 87% and 8%. Neutron and photon total intensities were normalized to a flux of 10^{10} particles cm^{-2} s^{-1}. The particle source planes were positioned on top of the Snyder geometry, parallel to the axial plane.

Simulations #2

The Monte Carlo voxel representations of the analytical Snyder model were constructed using MacNCTPlan and NCTPlan algorithms from computer-generated 2D axial images of the geometry. The same intensity thresholds were selected in both TPS to segment the images into regions of air, soft tissue and bone. Material compositions, kerma factors and particles' source described in section 3.3.2 were used for dosimetry calculations.

Figures of merits

To illustrate qualitative differences between the material assignment algorithms, voxel representations of the Snyder model constructed with the two TPS's were compared,

analyzing the material mixture in each cell. In addition, detailed quantitative assessments were carried out through the evaluation of 1D and 3D flux and dose rate distributions. Dose-rate components were compared for two different profiles: one perpendicular to the particle source plane (coincident with the beam central axis), and one parallel to the source plane coincident with the anterior-to-posterior direction (1 cm below the phantom surface and 1.5 cm apart the central beam axis). In the three-dimensional case, relative frequency distributions of neutron and photon flux percentage differences were evaluated.

3.4 Comparison results of the numerical test problems

3.4.1 Parallelepiped phantom

Figures 3.1-3.5 summarize the results of the performance analysis for the parallelepiped phantom in parallel and angular positions. Statistical uncertainties in the simulation data amounted less than 1% and became imperceptible in all figures. The numerical reference -denoted as Reference- corresponds to the "punctual" thermal neutron fluence estimation along the beam axis derived from MCNP (see section 3.3.1). For clarity, thermal neutron fluence profiles for only five of the 10 grid computed positions are depicted in Figs. 3.1 and 3.4.

As it can be seen from Fig. 3.1, the thermal neutron fluence estimation is almost the same for all grid positions but it stands out that the best results are achieved when the voxel grid is adjusted to match up the phantom's entrance face (Position 0). Note that for this position the homogenization process does not involve an expansion of the phantom's volume since the surface boundary voxels do not contain air.

Figure 3.2 shows the percentage relative differences between the NCTPlan voxel method and reference data (Reference), for the 10 computed positions. As denoted in the legend

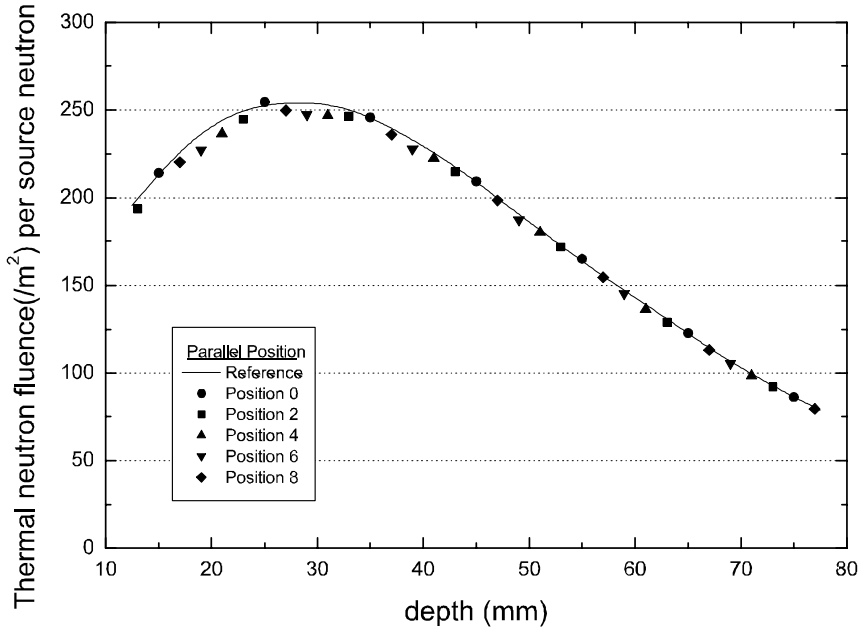

Figure 3.1: Comparison of the thermal neutron fluence profiles along the beam axis for the parallelepiped phantom in parallel position. Reference: MCNP punctual estimation. Positions 0, 2, 4, 6 and 8 are the different locations of the voxel grid with respect to phantom's entrance face.

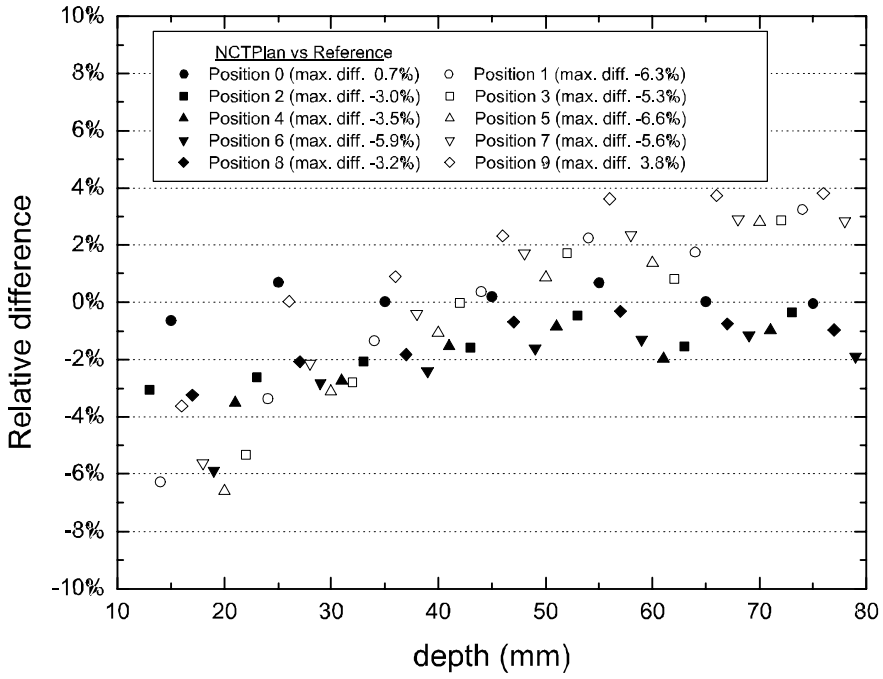

Figure 3.2: Percentage relative differences in thermal neutron fluences between the NCTPlan voxel model of the phantom in parallel position and its corresponding MCNP punctual reference data.

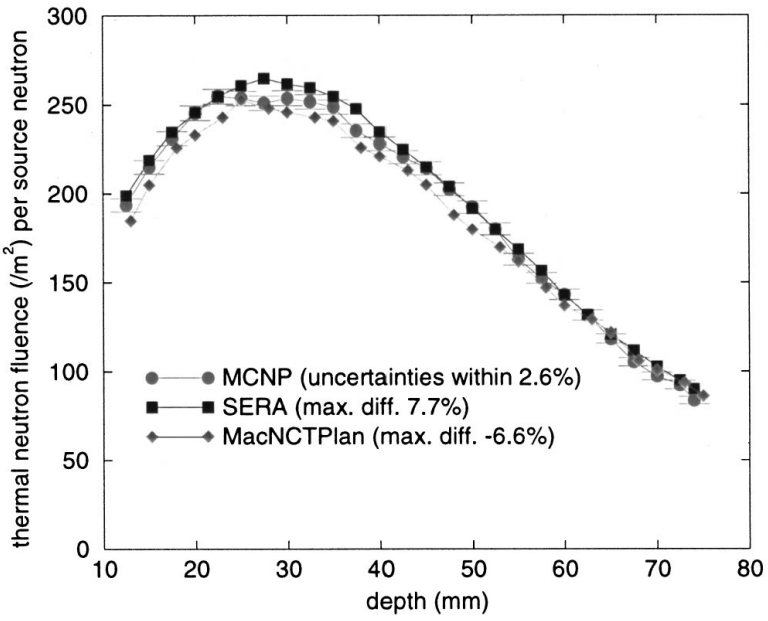

Figure 3.3: Thermal neutron fluence profiles along the beam axis for the parallelepiped phantom in parallel position. MCNP: 1 cm^3 averaged estimation. (Reprinted from Wojnecki and Green, *Medical Physics*, Vol. 29, No. 8, 2002, with permission of *Am. Assoc. Phys. Med.*)

of the graph, the maximum difference for each grid position ranges from -6.6% to 0.7%. In the range of depths considered in this analysis, position 5 provides the greatest maximum relative difference, i.e. -6.6%. This value agrees with the maximum difference between MacNCTPlan simulation and MCNP reference data reported by Wojnecki and Green [93], for the same simulation test (see Fig. 3.3).

Figure 3.4 shows the thermal neutron fluence profiles along the beam axis for the parallelepiped phantom in the angular position. Similarly to the parallel case, the fluence estimation is approximately the same for all grid positions but there seems not to be a preferred configuration. As shown in figure 3.5, the maximum relative difference between NCTPlan estimations and the reference data amounts -9.8%, considering all grid computed positions. This value, which represents the worst case in the analysis, is less than half the maximum value obtained by Wojnecki and Green for the MacNCTPlan algorithm, namely -21.1% (see Fig. 3.6). Moreover, the large deviation observed between

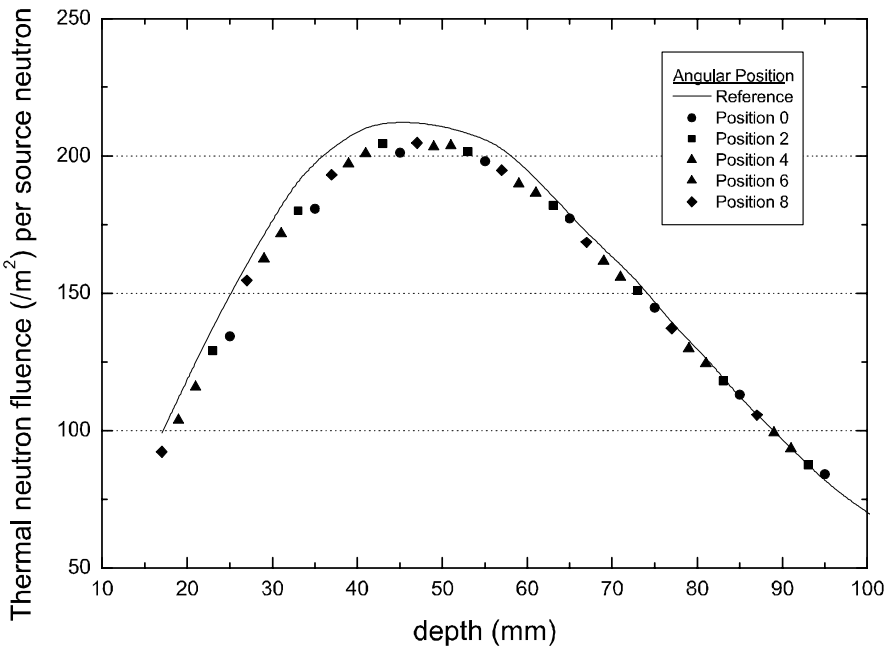

Figure 3.4: Comparison of the thermal neutron fluence profiles along the beam axis for the parallelepiped phantom in the angular position. Reference: MCNP punctual estimation. Positions 0, 2, 4, 6 and 8 are the different locations of the voxel grid with respect to phantom's entrance edge.

MCNP and MacNCTPlan results up to 60 mm in Fig. 3.6, is not present in the case of NCTPlan simulations. As Fig. 3.5 reveals, relative differences vary between -9.8% and -4.5% up to 25 mm, and fall below 6% in absolute value at deeper depths. Therefore, this analysis shows that the main reason for the lack of accuracy in the case of MacNCTPlan voxel model is a deficiency in the material assignment strategy. Although the downsizing of the 1 cm^3 voxel size would improve the accuracy of the MacNCTPlan algorithm, the proposed voxel algorithm leads to better results for any fixed size. In addition, the above results show that even in an extreme limit case, such as the irradiation of a sharp angled corner, the proposed 1 cm-based voxel model provides good results. Moreover, Wojnecki and Green have also presented the performance of the SERA TPS [78], which is a code specifically developed for BNCT that uses a reconstruction technique based on a pixel-by-pixel uniform volume element. As shown in Figs. 3.5 and 3.6, the accuracy obtained in the worst analyzed case with the NCTPlan algorithm is as good as that obtained with

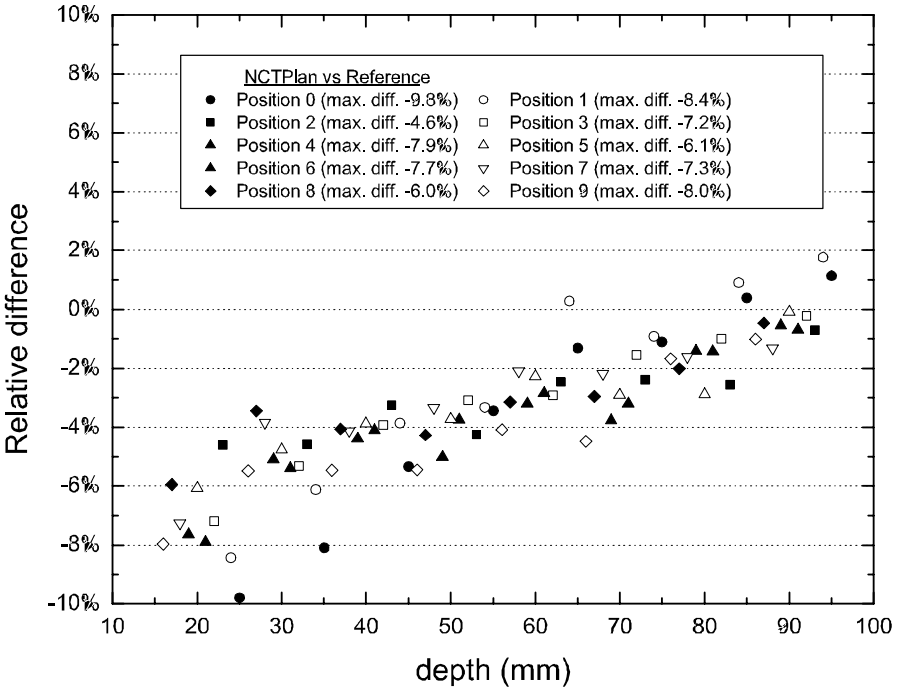

Figure 3.5: Percentage relative differences in thermal neutron fluences between the NCTPlan voxel model of the phantom in angular position and its corresponding MCNP punctual reference data.

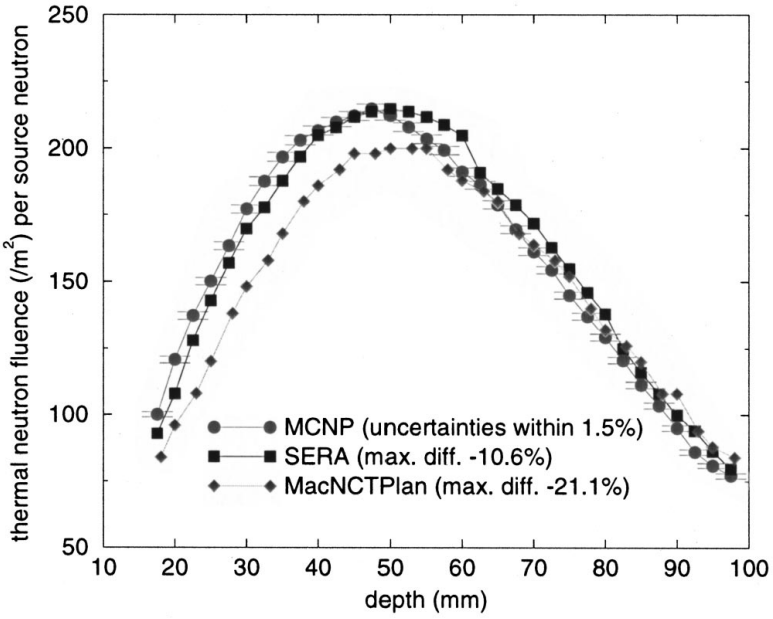

Figure 3.6: Thermal neutron fluence profiles along the beam axis for the parallelepiped phantom in the angular position. (Reprinted from Wojnecki and Green, *Medical Physics*, Vol. 29, No. 8, 2002, with permission of the *Am. Assoc. Phys. Med.*)

SERA's code, for the same simulation test. While the maximum relative difference in the angular position amounts -9.8% for the NCTPlan voxel model, a -10.6% of maximum difference was reported for the SERA system.

It should be stressed that all comparisons between NCTPlan and reference data are based on the referred punctual fluence estimation. The punctual estimation uses a very small tally volume of ~ 3 mm^3. Therefore, this track length estimate is a good approximation of the real thermal fluence at a point. On the other hand, the voxel model computes the thermal fluence in a 1 cm^3 volume. Since this track length estimate involves an average in a much larger volume around the axis containing maxima, the resulting thermal fluence is likely be lower than the punctual estimation (independently of the material homogenization effects). As a result, a better agreement between NCTPlan simulations and reference data should be obtained if a 1 cm^3 tally volume is used to compute reference values.

3.4.2 Snyder head phantom

Figure 3.7 shows (a) a cross section of the Snyder model (referred also to as analytical model), and the corresponding slices depicting (b) MacNCTPlan and (c) NCTPlan voxel representations. Different gray intensities correspond to different material mixtures. In addition, Fig. 3.7 (d) illustrates the comparison of the two voxel models highlighting those cells which received different material mixture assignments. Two effects are observed in this example. First, the NCTPlan algorithm produces a more symmetric voxel model which more closely matches the real geometry. Due to the symmetry of the Snyder model itself and with respect to the grid, it is reasonable to infer that voxel representations should maintain the same characteristic. Secondly, voxels with different material assignments are all located at the surface of the model (Fig. 3.7 [d]). These results suggest that differences between algorithms will be manifest in cells comprising various material interfaces.

Figures 3.8 and 3.9 (a)-(b) show the results of the numerical tests based on the compar-

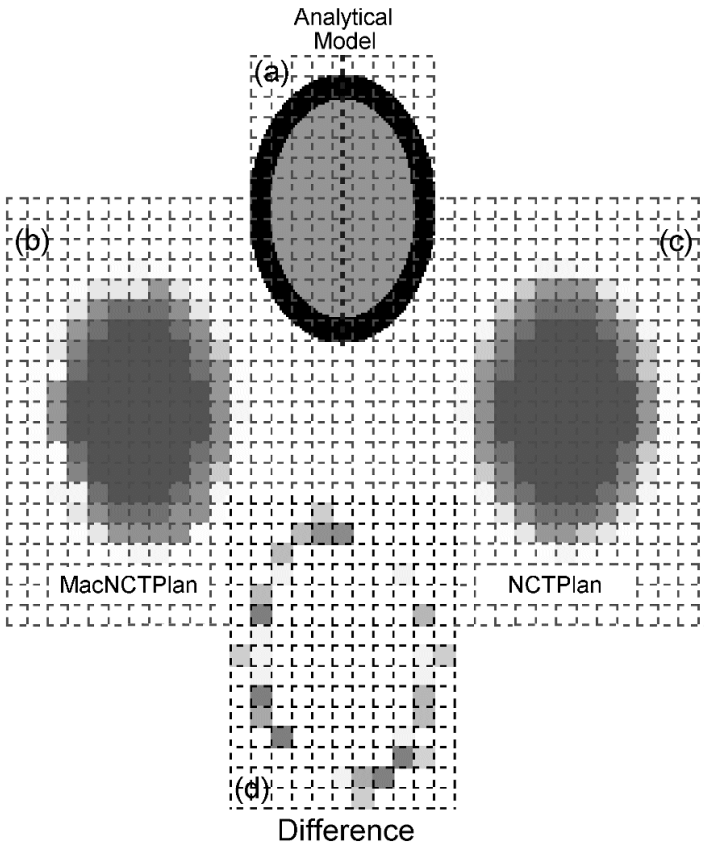

Figure 3.7: (a) Cross section of the analytical Snyder model, (b)-(c) slices of MacNCTPlan and NCTPlan Snyder voxel representations. Different gray intensities correspond to different material mixtures. (d) Differences between the two voxel models. Highlighted cells received a different material mixture assignment.

ison of one-dimensional dose-rates calculated for irradiation of the Snyder head phantom with an ideal epithermal neutron beam. Figure 3.8 illustrates the four dose-rate profiles along the beam central axis. Along this axis, MacNCTPlan and NCTPlan data appear to be identical and do not differ significantly from the reference data calculated in the analytical model. Figure 3.9 (a) shows boron and thermal neutron dose-rate profiles, and figure 3.9 (b) photon and fast neutron dose-rate profiles, for an axis parallel to the source plane. This comparison shows that the NCTPlan material assignment algorithm derives a computed dosimetry that closely matches the reference data. Average differences of less than 2% are obtained when dose-rate components are compared to reference values. On

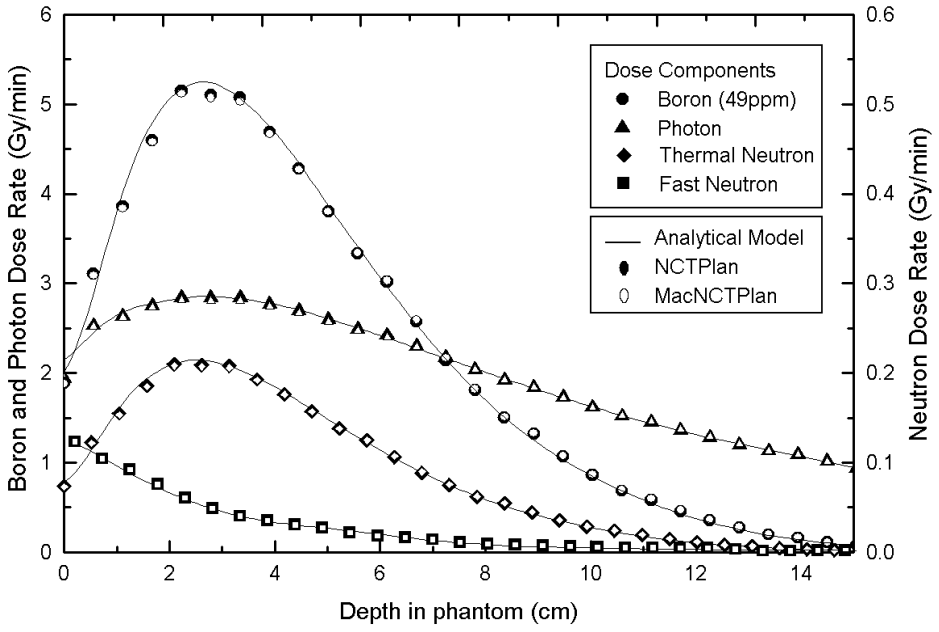

Figure 3.8: Comparison of dose-rate profiles calculated along the beam central axis of the Snyder head model.

the other hand, MacNCTPlan calculations tend to underestimate the reference dose-rates by up to 10%, particularly in dose components derived from thermal neutron interactions. This underestimation agrees with that reported by Wojnecki and Green [93].

In order to generalize the comparative study further, 3D distributions of neutron and photon flux were analyzed for the Snyder model. The volume considered for the analysis comprised all the voxels up to 8 cm in depth from the beam entrance point, and excluded those voxel containing only air. Although the complete voxel model may be compared to the reference data, the ipsilateral half of the model (receiving higher dose rates) was considered the most relevant volume. At 8-cm depth the maximum neutron flux is only 30% of the peak, and 0-8 cm represents a suitable range of depths for analyzing shallow and deep seated tumors.

Figures 3.10 and 3.11 show the relative frequency distributions of percentage difference in neutron and photon flux between the analytical model and the NCTPlan or MacNCTPlan model. Interesting features are shown in the histograms. First, the NCT-

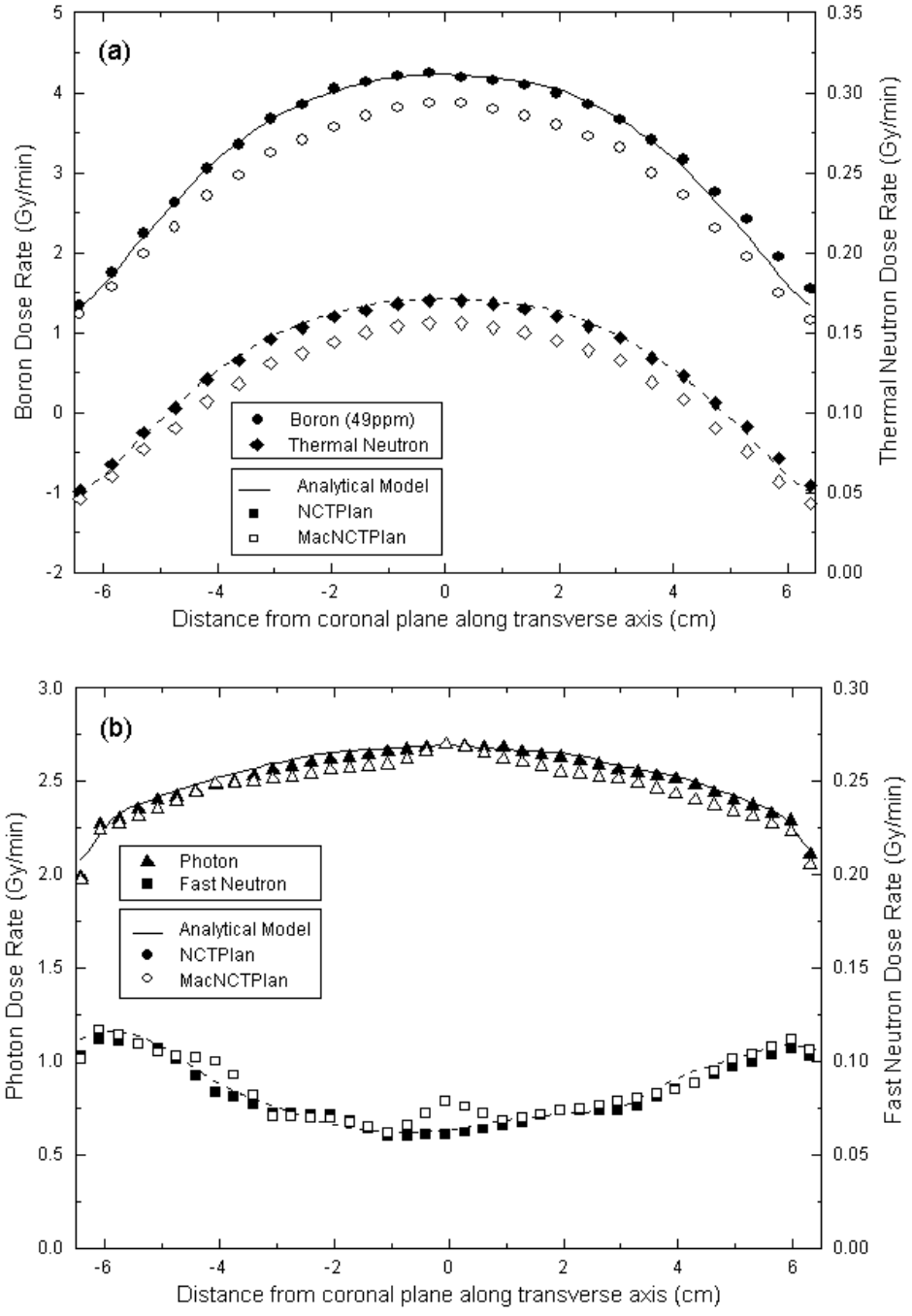

Figure 3.9: Comparison of (a) boron and thermal neutron dose-rate profiles, (b) photon and fast neutron dose-rate profiles, for the axis parallel to the source plane.

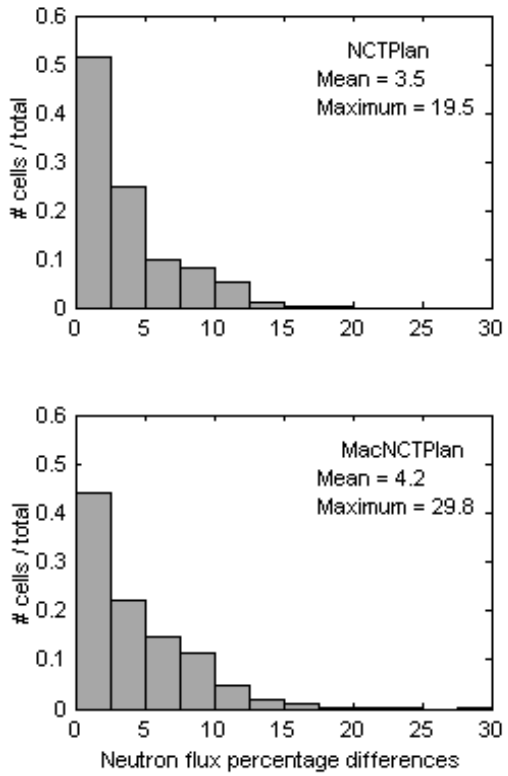

Figure 3.10: Relative frequency distributions of the absolute percent differences in total neutron flux for NCTPlan and MacNCTPlan compared to the analytical model of the Snyder head phantom.

Plan frequency distributions show less variability than the MacNCTPlan distributions. For example, 76% of NCTPlan cells have differences in neutron flux of less than 5% as opposed to 65% for MacNCTPlan. In addition, for both particle types, mean value of the difference distribution for NCTPlan is less than that for MacNCTPlan (see Figs. 3.10-3.11). Second, the maximum percentage differences in neutron and photon flux are 19.5% and 3.5 % for NCTPlan, and 29.8% and 4.2% for MacNCTPlan, respectively, occurring all at 8-cm depth. Note that both maxima are significantly lower for NCTPlan.

Finally, Fig. 3.12 plots total neutron flux percentage difference for (a) NCTPlan and (b) MacNCTPlan on a plane 25 mm below the top of the model. Figure 3.12 (a) shows the effect inherent to the voxel method: cells containing air interfaces, which in this

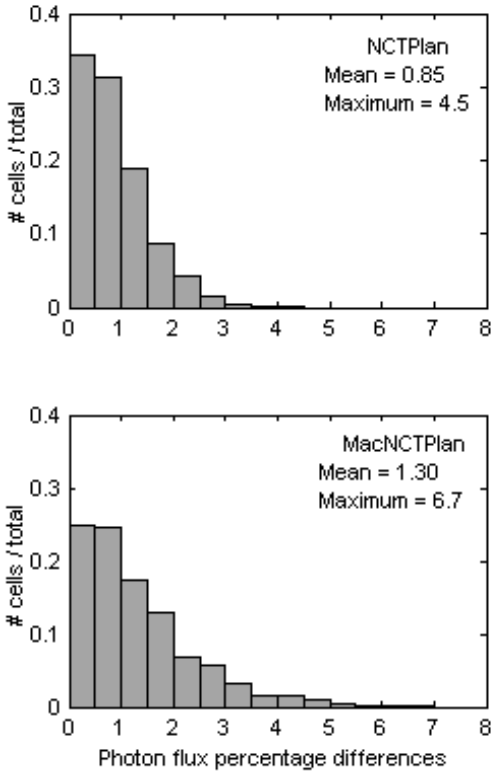

Figure 3.11: Relative frequency distributions of the absolute percent differences in total photon flux for NCTPlan and MacNCTPlan compared to the analytical model of the Snyder head phantom.

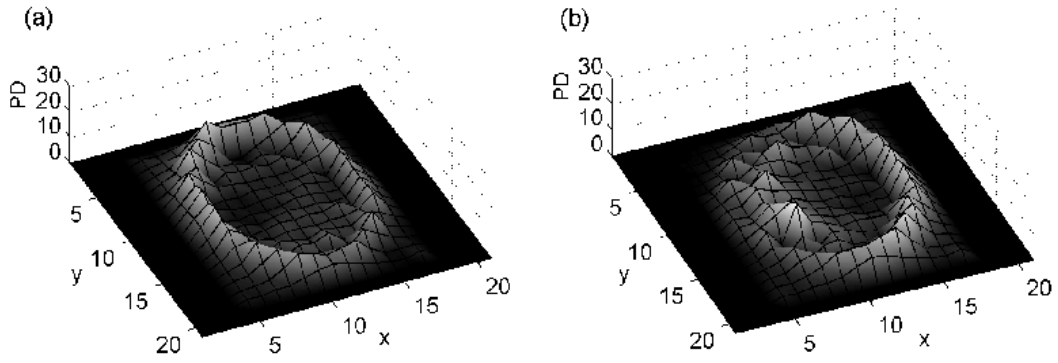

Figure 3.12: Surface plots of percent difference (PD) in total neutron flux for (a) NCTPlan and (b) MacNCTPlan versus the analytical model, at a depth of 2.5 cm below the top of the Snyder model.

problem are located on the surface of the model, are the most distorted by the material homogenization process. As a result, it is natural that superficial cells have the largest differences. On the other hand, the asymmetry of the percentage difference distribution stands out in figure 3.12 (b). This behavior is clearly related to the limitation in the MacNCTPlan material assignment algorithm and not with homogenization effects.

3.5 Experimental validation of NCTPlan algorithm

The BNCT facility of Argentina is currently dedicated to the treatment of cutaneous melanoma [35], and has been designed in order to provide a hyperthermal flux with a maximum thermal flux at shallow depths [7]. A more detailed description of the RA-6 BNCT facility is provided in Chapter 5. As part of its characterization, detailed experimental dosimetry was performed by neutron flux and dose measurements in water-filled acrylic phantoms, using foil activation and paired ionization chamber techniques [1, 85]. The results of the physical dosimetry, given by thermal neutron flux, fast neutron and total gamma absorbed dose rate profiles along the central beam axis and an off-central axis, were used as the experimental reference data in this work. In addition, the numerical data derived for the exact geometry modelled by the reference computational tool MCNP

was also included in this study.

The comparisons for the dose-rates components are made for those points inside the models where CPE conditions are fulfilled for photons (see section 2.1.2). In the case of thermal neutron flux measurements, an additional point on the surface of the phantom was included.

3.5.1 Beam physical dosimetry

Dose-rate and thermal neutron flux-depth distributions produced by the RA-6 hyperthermal beam were measured in two water-filled phantoms: a standard parallelepiped phantom selected by international BNCT community as the common phantom for dosimetry exchange (called reference phantom) [44], and a cylindrical phantom [5, 7, 66]. The reference phantom is an acrylic box of dimension 40×40 cm in height and width, 20 cm depth along the beam axis, and a wall thickness on the beam entrance side of 0.5 cm. This size phantom is sufficiently large to approximate a semi-infinite scattering medium for a 16 cm diameter aperture which is 1 cm larger than the RA-6 beam aperture [44]. The dimensions of the cylindrical acrylic phantom are 12 cm in diameter, 41.5 cm high and 0.3 cm thick. This geometry was selected for dosimetry measurements since represents a suitable approximation for extremities.

Neutron flux measurements were performed by foil activation, using the well-known cadmium difference method, and the paired ionization chambers technique [85]. Bare and Cd-covered gold wires were supported in acrylic holders inside the phantoms and their activities were determined by using a HPGe gamma spectrometer. The thermal (0 - 0.5 eV) neutron cross section and the cadmium factor were obtained through detailed neutron transport calculations by the Monte Carlo MCNP4C code. Doses were determined from ionization chamber responses, by the paired ionization chambers technique following the approach given by Rogus *et al.* [85]. The ionization chambers used were thimble-shaped, with 0.1 cm^3 active volume, manufactured by Far West Technology. The highest neutron

sensitive chamber was a tissue equivalent chamber, IC-18 model, flushed with methane-based tissue equivalent gas. The other chamber was a graphite, IC-18G model, flushed with carbon dioxide. Both chambers were polarized with a 250 DCV batteries array. Details about the determination of the sensitivity parameters of both ionization chambers are reported in [67]. Chambers were placed in a waterproof housing, positioned in such a way that the chamber axis was aligned with the measured axis. As the chamber response is an electrometric current, a Keithley electrometer, Model 6517A, was used. Readings, corrected by pressure and temperature, were recorded and processed.

Figure 3.13 shows the reference phantom positioned against the RA-6 beam exit port, supported by a table affixed to the its external face. Measurements were performed along the central beam axis and a 4 cm-lateral axis [5, 66]. Figure 3.14 shows the set up in the case of the cylindrical phantom. The cylinder was positioned vertically with no gap between the beam port and the phantom wall, and measurements were carried out along the central beam axis in 12 positions each separated by 0.5 cm [7].

3.5.2 Simulations

The Monte Carlo voxel representation of the reference phantom was constructed using computer-generated 2D axial images of the geometry. In the case of the cylindrical phantom, the model was generated from a set of 125 contiguous 2 mm CT scans. To simulate the physics of the test problems as closely as possible in terms of particle transport in both simulations, soft tissue and bone materials were assigned water and acrylic compositions [1], respectively. The computational radiation source described by discretized distributions was used to compute flux and depth-dose rate profiles (see section 5.1.2). Both gamma and fast neutron absorbed dose rates were specified for ICRU 46 adult muscle tissue [51].

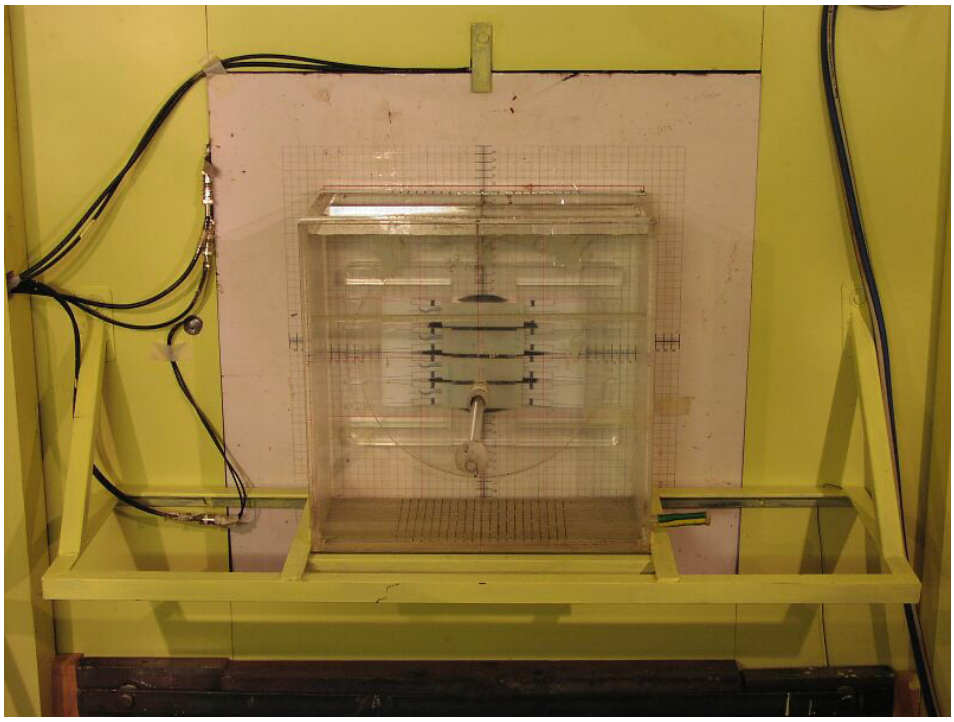

Figure 3.13: Reference phantom positioned in the RA-6 beam port.

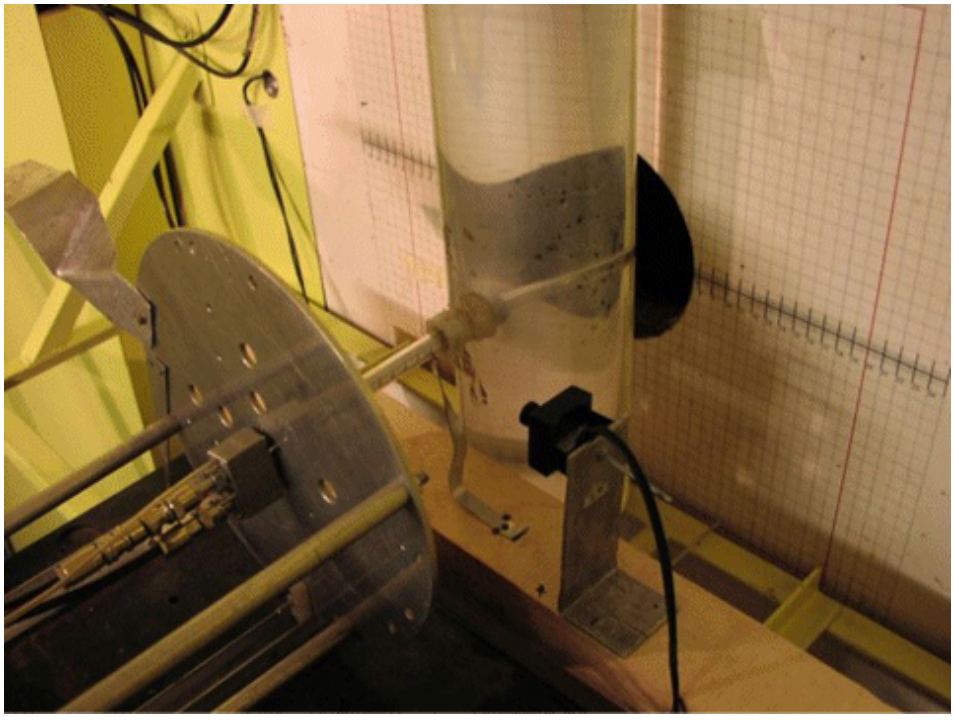

Figure 3.14: Cylindrical phantom positioned in the RA-6 beam port.

3.6 Comparison results based on the physical dosimetry of the RA-6 beam

3.6.1 Reference water phantom

Figures 3.15-3.20 comprise the results of the comparative study based on the physical dosimetry of the RA-6 hyperthemal neutron beam, measured along the central beam axis and a 4 cm-lateral axis in the parallelepiped phantom. All calculations were run to high statistical convergence, with statistical uncertainties for numerical values less than 1%. Figure 3.15 illustrates the thermal neutron flux profiles along the central beam axis. NCTPlan results agree most accurately with measurements, the absolute deviation to the experimental mean values being 2% on average, and the measurements uncertainties ±6% on average. Figures 3.16 and 3.17 correspond to fast neutron and total photon dose rate profiles along the central beam line, specified for ICRU 46 adult muscle tissue. Both components show a good agreement with measurements. In the case of the fast neutron dose rate component, the agreement between the three sets of data is excellent, the absolute deviation of NCTPlan data to the experimental mean values being 4% on average, and measurements uncertainties ±30%. For the total photon dose rate component, NCTPlan and MCNP profiles show a slight underestimation of the mean measurement values. Since both numerical results illustrate almost the same behavior, this effect is likely to be due to the photon intensity factor of the RA-6 beam model (i.e., the normalization factor), and thus easily fixed. Nevertheless, the absolute deviation of NCTPlan data to the experimental mean values is 5% on average, equal to the average measurements uncertainties (±5%). Figures 3.18-3.20 present the just mentioned comparisons for the 4 cm-lateral axis. All NCTPlan derived components show a very good agreement with measurements. The results for this axis are almost the same that for the previous case but the implications might be wider. Since the accuracy in the off-central axis is as good as in the central beam line, the NCTPlan performance in the whole model is very likely to be also good.

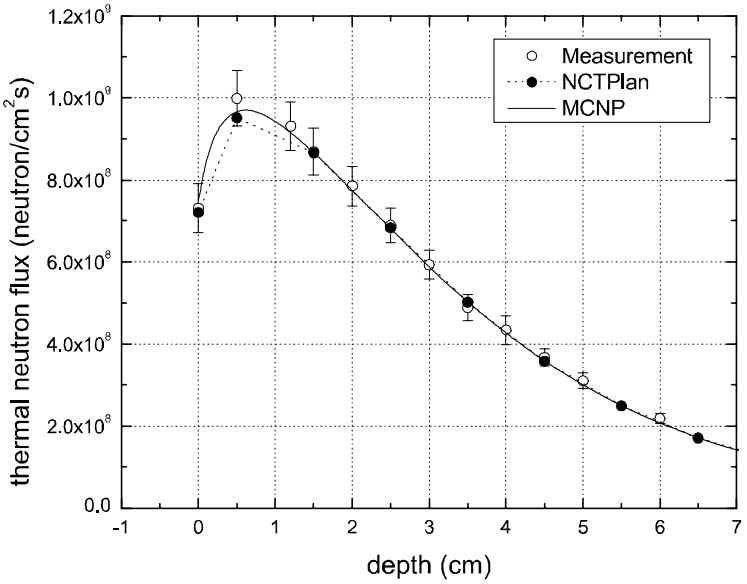

Figure 3.15: Comparison of measured and calculated thermal neutron flux along the central axis of the RA-6 beam in the reference phantom.

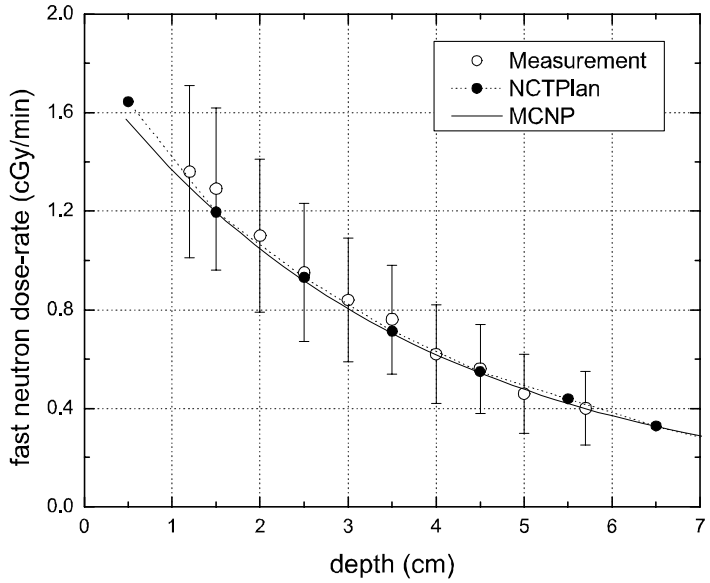

Figure 3.16: Comparison of measured and calculated fast neutron absorbed dose rate along the central axis of the RA-6 beam in the reference phantom. Dose rates are specified for ICRU 46 adult muscle tissue.

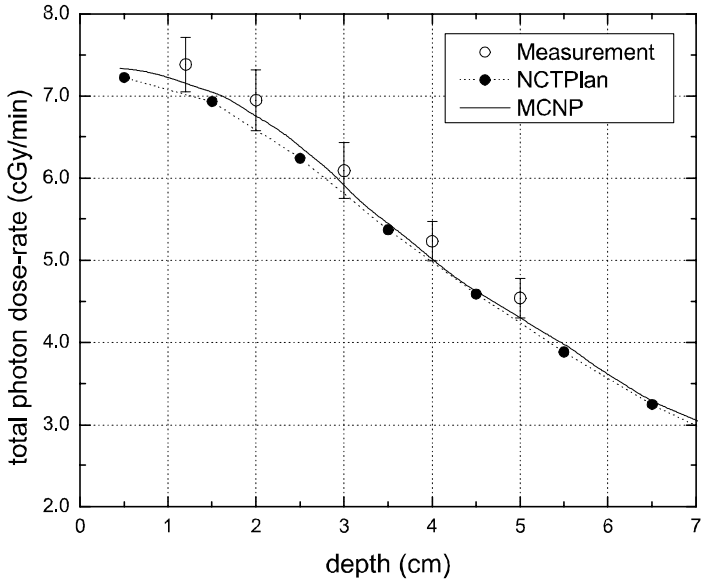

Figure 3.17: Comparison of measured and calculated total photon absorbed dose rate along the central axis of the RA-6 beam in the reference phantom. Dose rates specified for ICRU 46 adult muscle tissue.

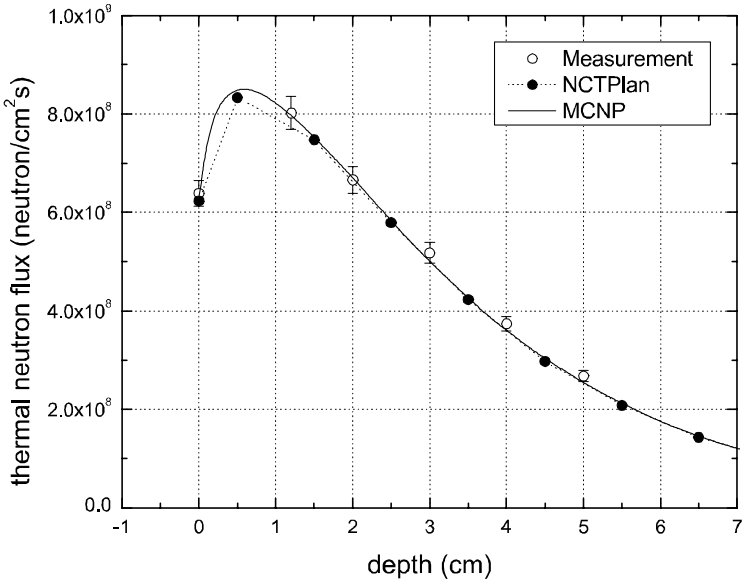

Figure 3.18: Comparison of measured and calculated thermal neutron flux along the 4 cm lateral axis in the reference phantom.

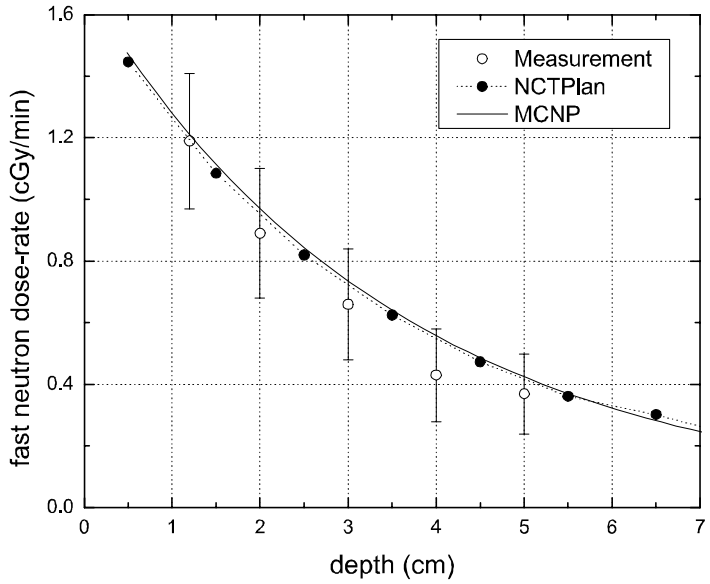

Figure 3.19: Comparison of measured and calculated fast neutron absorbed dose rate along the 4 cm lateral axis in the reference phantom. Dose rates specified for ICRU 46 adult muscle tissue.

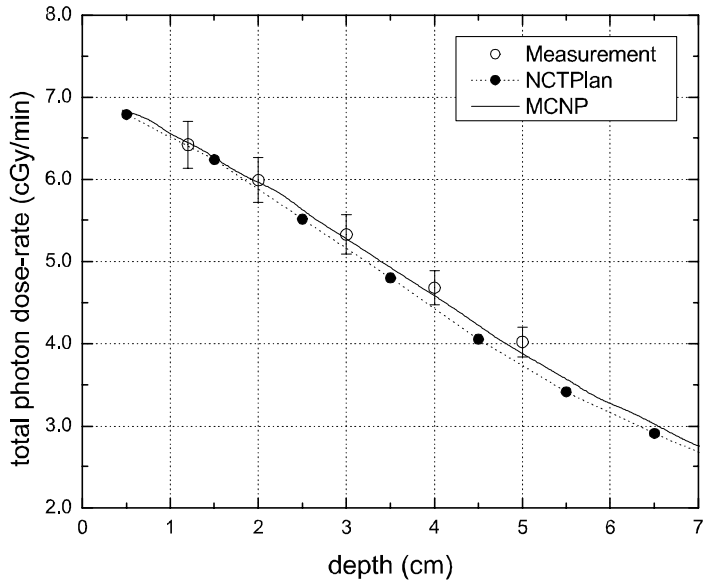

Figure 3.20: Comparison of measured and calculated total photon absorbed dose rate along the 4 cm lateral axis in the reference phantom. Dose rates specified for ICRU 46 adult muscle tissue.

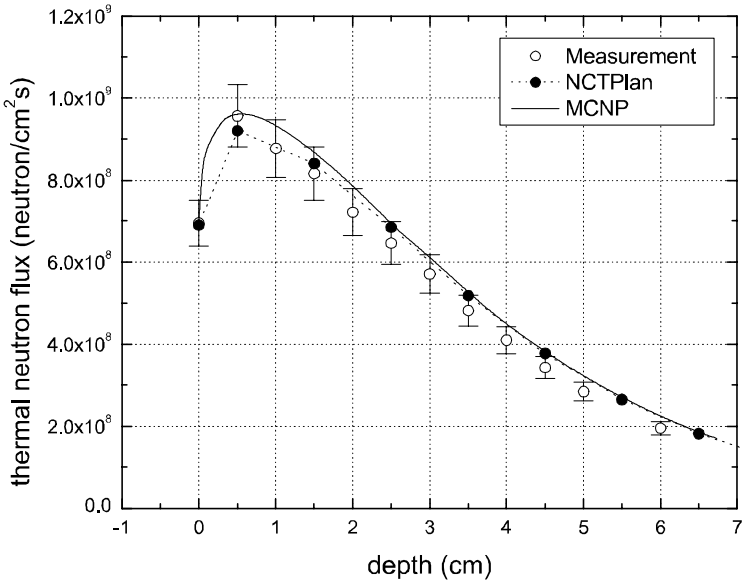

Figure 3.21: Comparison of measured and calculated thermal neutron flux along the central axis of the RA-6 beam in the cylindrical phantom.

3.6.2 Cylindrical phantom

Figures 3.21-3.23 show the results of the comparative study based on the physical dosimetry of the RA-6 hyperthemal neutron beam measured in a cylindrical phantom [7]. Statistical uncertainties for numerical values are less than 1%. Figure 3.21 illustrates the thermal neutron flux profiles along the central beam axis. NCTPlan data agree most accurately with measurements, the absolute deviation to the experimental mean values being 7% on average, and the measurements uncertainties ±8%. Figures 3.22 and 3.23 correspond to fast neutron and total photon dose rate profiles specified for ICRU 46 adult muscle tissue. Both components show an excellent agreement with measurements, the absolute deviation to the experimental mean values being 4% and 1% on average, and measurements uncertainties ±32% and ±1%, for fast and photon components respectively.

It is important to stress that the RA-6 beam model used in this comparison was normalized to measurements carried out in the international reference cubic water phantom

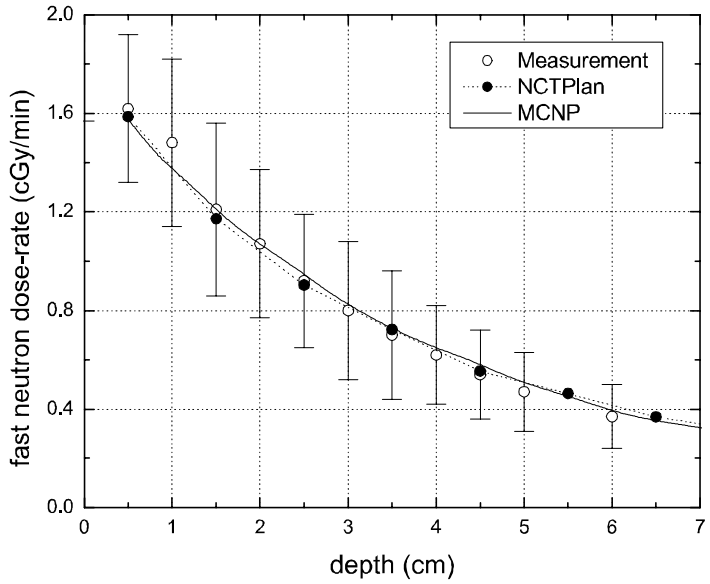

Figure 3.22: Comparison of measured and calculated fast neutron absorbed dose rate along the central axis of the RA-6 beam in the cylindrical phantom. Dose rates are specified for ICRU 46 adult muscle tissue.

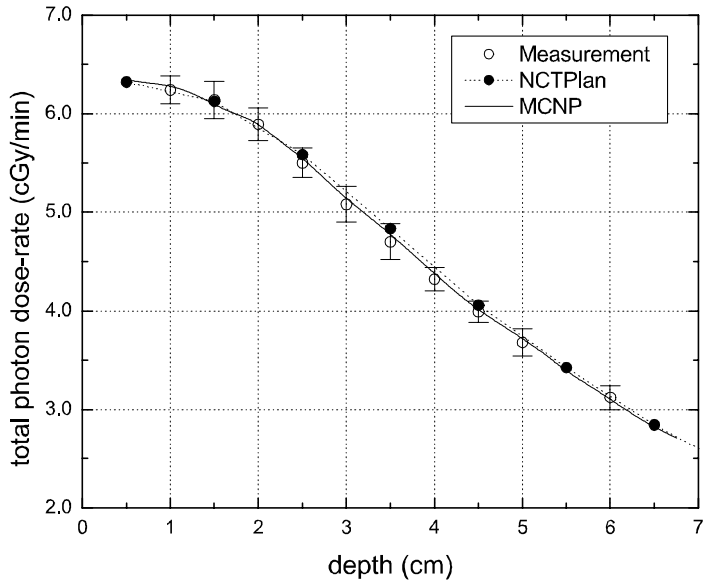

Figure 3.23: Comparison of measured and calculated total photon absorbed dose rate along the central axis of the RA-6 beam in the cylindrical phantom. Dose rates specified for ICRU 46 adult muscle tissue.

(section 5.1.2). No other normalization procedure was applied between MCNP results and measurement in the cylindrical phantom. Then, the agreement in figures 3.21-3.23 indicates the goodness of the beam model to derive the dosimetry in other geometries. In addition, NCTPlan calculations also match up measurements without the need of any scaling factor, which indeed demonstrates the accuracy of the 1 cm-based voxel model.

3.7 Concluding remarks

The performances of the 1 cm-based voxel reconstruction methods used in the MacNCTPlan and NCTPlan treatment planning systems for BNCT were compared and analyzed in detail. To assess the performances of these algorithms, they have undergone an extensive verification process in which numerical reference data was used, and one and three-dimensional flux and dose rate distributions were evaluated. As a result of this evaluation, the NCTPlan voxel model proved better independently of the particularities of the reference problems (i.e., particle sources and phantom geometries).

With the aim of assessing the accuracy of the NCTPlan model in a clinical-like case, comparisons between the in-phantom experimental dosimetry performed at the RA-6 BNCT facility and the corresponding computational dosimetry calculations were also carried out. As a result, the 1 cm-resolution of the NCTPlan voxel method proves accurate enough for all presented tests, involving a realistic BNCT particle source (i.e., the RA-6 beam) and both planar and curved phantom geometries.

For a global evaluation of NCTPlan voxel model with both numerical calculations and measurements, agreement is very good excluding very shallow depths in which, to achieve accuracy, the anatomy images need be positioned in a suitable way. The effect of the voxel model in surface boundary regions will be deeper developed in the following chapter.

The presented results are consistent with those obtained by Kiger *et al.* [56] in the verification and validation of the NCTPlan program using the fission converter neutron irradiation beam at MIT reactor.

To summarize, the NCTPlan voxel model was verified and validated using a suite of reference problems which comprises simple and complex geometries, ideal and realistic particle sources with very different characteristics (in spatial, angular and energy distributions, beam size, etc.), figures of merits based on one and three dimensional flux (or fluence) and dose rate distributions, and numerical and experimental reference data. This new version presents many improvements over MacNCTPlan algorithm which clearly justifies its implementation in NCTPlan TPS and clinical use.

Chapter 4

Voxel model: Theoretical analysis on surface boundary regions

4.1 Introduction

One natural consequence of the voxelization and homogenization procedures is the directional bias due to the cubic distortions introduced by partitioning a 3D geometry. For example, the $1cm^3$ voxel model of a filled sphere transforms its original smooth surface to a more stepwise surface. In addition, the volume and surface area of the voxelized sphere are always larger that the real ones, since most voxels lying in surface regions that share the interior and exterior of the sphere are assigned a homogenized material other than air. These kind of distortions and expansion effects mainly affect surface boundary areas. Therefore, it is reasonable to expect the voxel method to degrade its accuracy near boundary regions where a fine-scale information would be desirable.

The question of how good the accuracy of the voxel method is to derive the patients' dosimetry is not limited to the question of how much the voxel size and material mixing affects the particle transport itself. In order to assess the dosimetry for every point in the geometry, there are other factors that need be taken into account. Basically, the whole

process comprises the creation of the voxel model from a set of CT images, the calculation of average particle fluence or dose in every cell, and finally a method that extrapolates estimates to any point inside the geometry model. The voxel model involves the selection of the voxel size and the strategy used to assign a homogeneous material to each cell. The calculation of particle fluence and doses involves the selection of the Monte Carlo engine, the tally volume, the assignment of the average values to a point inside the tally volume (typically, the center of the volume), and the assumption that absorbed doses can be approximated by kerma [52].

Subject to this scenario, this chapter presents a detailed analysis of the performance of the voxel reconstruction method for a fixed voxel size of 1 cm^3, stressing the effect of the material homogenization on surface boundary regions. The aim is to propose a different strategy to better adjust the average fluence in the surface cells and therefore, to improve the prediction of the punctual fluence within the first millimeters of the surface. As the boron, neutron, and photon doses delivered by BNCT are directly determined from the particle fluences, it is clear that a better estimate of photon and neutron fluences will give a better estimation of the doses as well. A theoretical analysis of a parallelepiped phantom is carried out, taking into account the effects of homogenization and percentage rounding in the voxel model. This analysis will suggest the strategy to follow in order to improve fluence and dose estimates at shallow depths in the model.

4.2 Material homogenization

In this section, the material homogenization effect on surface boundary cells is investigated. The theoretical analysis starts with a simple ideal geometry, and then it considers more complex geometries. The validity of the results in clinical-like cases is discussed.

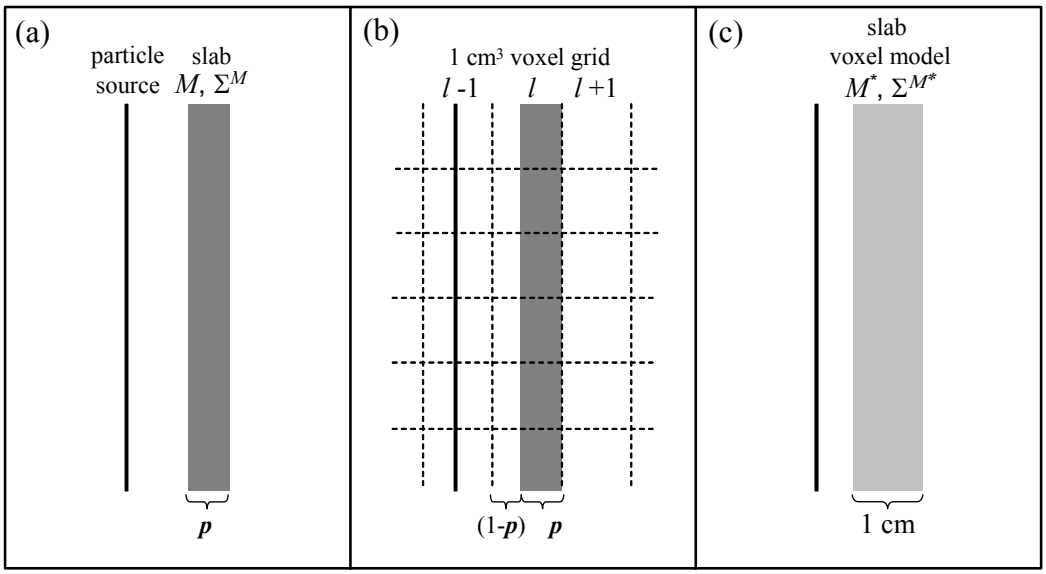

Figure 4.1: (a) Infinite p centimeter thick slab ($0 < p < 1$) irradiated with an infinite planar source, (b) setup used to generate the slab voxel model, (c) voxel representation of the slab.

4.2.1 Slabs

As a first approach to the problem, consider an infinite p centimeter thick slab ($0 < p < 1$) of material M and macroscopic total cross section Σ^M, irradiated with an infinite planar neutron or photon source (Fig. 4.1 [a]). Now consider the voxel model of the slab, that results from positioning the voxel grid in such a way that all the slab is contained in a layer l of voxels (Fig. 4.1 [b]). Before rounding the percentages of material M and air, each of the cells in l contains a proportion p of M and $(1-p)$ of air. The first step in the analysis is to determine how the average fluence for a slab portion of 1 cm^2 cross section and p cm thick is compared with the average fluence in a 1 cm^3 voxel of the homogenized slab.

To assess the effect of homogenization only, eventual rounding is ignored for the moment. The result of the voxelization is a new slab, which is 1 cm thick and is made of a homogeneous material M^* (Fig. 4.1 [c]). The macroscopic total cross section of this

mixture is

$$\Sigma^{M^*} = (1-p)\Sigma^{air} + p\Sigma^M,$$

where Σ^{air} is the macroscopic total cross section of air. Since $\Sigma^{air} \ll \Sigma^M$, the value of Σ^{M^*} is well approximated by $p\Sigma^M$. Now, the mean free path of a particle in the homogenized slab is

$$\lambda^* = \frac{1}{\Sigma^{M^*}} \approx \frac{1}{p\Sigma^M} = \frac{\lambda}{p},$$

where λ is the particle mean free path in the original slab. In other words, in the homogenized slab (which is $1/p$ times as thick as the original slab), the particle mean free path is $1/p$ times as long as the original one. Thus, the homogenized slab can be considered as a rescaling of the original slab.

The above result implies, for example, that the probability that a particle undergoes n reactions in any of the slabs is the same. Then, there is a one-to-one correspondence between tracks in the homogenized and real slabs, the only difference being that in the voxel model, trajectories between reactions are dilated by $1/p$. As a consequence of this, the mean track length $\overline{L^*}$ in the homogenized slab is $1/p$ times the mean track length $\overline{L}$ in the real slab. Then,

$$\overline{L^*} = \frac{\overline{L}}{p} \tag{4.1}$$

Now, the average fluence in a portion A of real slab (1 cm^2 of cross section and p cm thick) is proportional to the quotient between the mean track length in A and the volume of A [15]. Since tracks exiting A through the top face are compensated for by tracks entering A through the bottom face and vice versa (and the same happens with the other lateral faces), the average fluence can be computed as

$$\overline{\Phi} = \frac{N\overline{L}}{p\,\mathrm{cm}^3}. \tag{4.2}$$

Here N is the number of incident particles traversing the 1 cm^2 cross section of A. On the other hand, the average fluence in a 1 cm^3 voxel of the homogenized slab is equal, by the same reasons, to

$$\overline{\Phi^*} = \frac{N\overline{L^*}}{1\,\mathrm{cm}^3} = \frac{N\overline{L}}{p\,\mathrm{cm}^3}, \tag{4.3}$$

after substitution of expression (4.1). As a result, the average fluence in both volumes coincides. Therefore, in this case, the average fluence in the portion A of real slab can be well estimated as the average fluence in the 1 cm^3 homogeneous cell.

To put the above arguments into calculations, the following shows an example of this result, explicitly computing the average fluences in the real and homogenized slabs for the case of very low absorbing materials with small macroscopic scattering cross sections.

Example:

Consider an infinite p centimeter thick slab ($0 < p < 1$) of a low absorbing material M and macroscopic total cross section Σ^M, perpendicularly irradiated with a beam represented by an infinite planar source. If the particles' mean free path $1/\Sigma^M$ is sufficiently larger than p cm, they can be supposed to undergo at most one reaction inside the slab. Since M is a low absorbing material, only scattering reactions need be considered. In Appendix B, the probability that a neutron undergoes at most one reaction is computed. For simplicity, all particles will be treated as neutrons, but the analysis remains valid for photons.

As shown in equation (4.2), the average neutron fluence in a portion A of this slab (A has 1 cm^2 of cross section and is p cm thick) can be estimated as:

$$\overline{\Phi} = \frac{N\,\overline{L}}{p\,\mathrm{cm}^3}, \tag{4.4}$$

where N is the number of incident particles traversing the frontal 1 cm^2 cross section of A, and $\overline{L}$ is the mean track length of particles in the slab. This mean track length has then to be computed.

To simplify the notation in some formulas, let $\mathbf{p} = p$ cm be the slab thickness. The probability that a neutron does not suffer its first collision in the slab is $e^{-\mathbf{p}\Sigma^M}$. For these neutrons, the track length is exactly $\mathbf{p}$. On the other hand, a neutron has a collision inside the slab at r cm from the surface ($0 < r < p$) with a probability density of $\Sigma^M e^{-\mathbf{r}\Sigma^M}$(here, $\mathbf{r} = r$ cm). For such a particle, the track length is $\mathbf{r} + (\mathbf{p} - \mathbf{r})/\cos(\theta)$, where θ is the angle between the beam direction and the neutron direction after the collision. Angles θ between 0 and $\pi/2$ occur with a probability density of $2\sin(\theta)\cos(\theta)$. Consequently, the mean track length of a particle can be computed as:

$$\begin{aligned}
\overline{L} &= \int_0^p \int_0^{\pi/2} \left(\mathbf{r} + \frac{\mathbf{p}-\mathbf{r}}{\cos(\theta)}\right) 2\sin(\theta)\cos(\theta)\,\Sigma^M e^{-\mathbf{r}\Sigma^M} d\theta d\mathbf{r} + \mathbf{p}e^{-\mathbf{p}\Sigma^M} \\
&= \int_0^p \mathbf{r}\Sigma^M e^{-\mathbf{r}\Sigma^M} d\mathbf{r} \int_0^{\pi/2} 2\sin(\theta)\cos(\theta)\, d\theta \\
&\quad + \int_0^p (\mathbf{p}-\mathbf{r})\,\Sigma^M e^{-\mathbf{r}\Sigma^M} d\mathbf{r} \int_0^{\pi/2} \sin(\theta) d\theta + \mathbf{p}e^{-\mathbf{p}\Sigma^M} \qquad (4.5) \\
&= -\frac{\mathbf{p}\Sigma^M e^{-\mathbf{p}\Sigma^M} + e^{-\mathbf{p}\Sigma^M} - 1}{\Sigma^M} + 2\frac{\mathbf{p}\Sigma^M + e^{-\mathbf{p}\Sigma^M} - 1}{\Sigma^M} + \mathbf{p}e^{-\mathbf{p}\Sigma^M} \\
&= 2\mathbf{p} - \frac{1}{\Sigma^M} + \frac{e^{-\mathbf{p}\Sigma^M}}{\Sigma^M}. \qquad (4.6)
\end{aligned}$$

Substituting expression (4.6) into equation (4.4), the average fluence in the portion of slab A is therefore:

$$\overline{\Phi} = \frac{N}{p\,\mathrm{cm}^3}\left(2\mathbf{p} - \frac{1}{\Sigma^M} + \frac{e^{-\mathbf{p}\Sigma^M}}{\Sigma^M}\right) = \frac{N}{\mathrm{cm}^2}\left(2 - \frac{1}{\mathbf{p}\Sigma^M} + \frac{e^{-\mathbf{p}\Sigma^M}}{\mathbf{p}\Sigma^M}\right). \qquad (4.7)$$

Now, if the mean track length is computed in a 1 cm^3 cell of the slab voxel model, a material mixture M^* consisting of a proportion p of M and $(1-p)$ of air has to be considered. As previously observed, this can be seen as a new slab 1 cm thick with a macroscopic cross section of approximately $p\Sigma^M$. Therefore, proceeding as before, the mean track length is:

$$\overline{L^*} = 2\mathrm{cm} - \frac{1}{p\Sigma^M} + \frac{e^{-\mathbf{p}\Sigma^M}}{p\Sigma^M}, \qquad (4.8)$$

and consequently, the average fluence in a 1 cm^3 cell is:

$$\begin{aligned} \overline{\Phi^*} &= \frac{N}{1\,\mathrm{cm}^3}\left(2\mathrm{cm}-\frac{1}{p\Sigma^M}+\frac{e^{-\mathbf{p}\Sigma^M}}{p\Sigma^M}\right) \\ &= \frac{N}{\mathrm{cm}^2}\left(2-\frac{1}{\mathbf{p}\Sigma^M}+\frac{e^{-\mathbf{p}\Sigma^M}}{\mathbf{p}\Sigma^M}\right), \end{aligned} \tag{4.9}$$

which coincides with the average fluence obtained for the original slab (Eq. [4.7]).

It is worth mentioning that slabs and sources do not need be infinite for the average fluence in both real and homogenized volumes to coincide. If both the slab and the source are large enough, the portion of slab around the beam central axis behaves as in the idealistic situation. To verify these arguments, MCNP simulations were carried out using slabs with a 40×40 cm^2 cross section and two different particle sources: an ideal 5 keV monodirectional planar disk source of 10 cm radius, and the RA-6 reactor hyperthermal beam of 7.5 cm radius. Note that simulations with MCNP consider all possible reactions in the medium. Appendix C presents the details of these simulations. As a result, MCNP calculations derived differences smaller than 1% and 2.5 % between average fluences in real and voxel geometries for the ideal and real source, respectively. Since these values are of the same order as the statistical uncertainties for numerical values ($\sim 1\%$), average fluences can be considered the same in the original and voxelized slabs. This is consistent with above arguments.

4.2.2 Parallelepiped phantoms

Now, consider an infinite parallelepiped phantom (i.e., a half-space geometry), placed with respect to the voxel grid in such a way that its p superficial centimeters lie in the first layer of the 1 cm^3 cells ($0 < p < 1$). The average fluence in this boundary portion of the phantom can also be described with great accuracy. The main difference between this problem and the previous one is that, in addition to the particle flux coming directly from

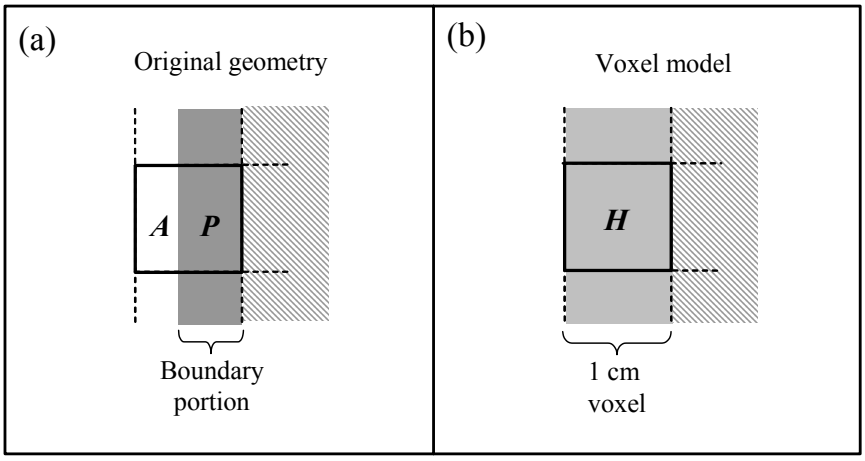

Figure 4.2: Surface portion of a parallelepiped phantom. (a) Original geometry: highlighted 1 cm^3 surface cell ($A \cup P$) contains a portion P of material M and a portion A of air, (b) Voxel model: highlighted 1 cm^3 surface cell (H) contains a homogeneous material composed by material M and air.

the source, there is also a particle flux due to backscattering in the region contained in the following layers. However, this flux can be considered as coming from a source in the back and acting on the thin slab of material contained in the first layer. In other words, the portion of phantom from the second layer on, acts on the first layer as another source. This source is the same for both the real and the homogenized case. The way this source acts on the first layer coincides with the one described for the thin slab. Therefore, the average fluence in a portion of phantom contained in a cubic cell of the first layer can be well estimated as the average fluence in the homogenized cell of the voxel model. Again, this causes no significant error even if the phantom is not infinite but only large enough.

To summarize, in order to adjust the average fluence in the surface cells, the following strategy proves accurate for the parallelepiped phantom: the average fluence in the boundary portion of phantom P contained in a cubic voxel is to be estimated by the average fluence in the whole cell H of the voxel model (see Fig. 4.2). Note that NCTPlan algorithm computes the average fluence in H and uses this value to estimate the average fluence in $A \cup P$ (i.e., the whole geometry contained in the 1 cm^3 cell). The new strategy

is to use the average fluence in H to estimate the average fluence in P.

Now, in most clinical applications, the patient's anatomy is positioned in such a way that, around the beam central axis, the surface is approximately flat and the central axis is perpendicular to the local region. Therefore, the conclusions of the present analysis also hold for these boundary areas.

4.2.3 Reassignment strategy

As the previously analysis suggests, the average fluence in a surface region is well approximated by the average fluence in the homogeneous voxel. Now, to evaluate the fluence in every point of the modeled geometry, the average fluence in the surface voxel must be assigned to some point in space in order to carry out the interpolation/extrapolation process. Instead of assigning it to the center of the voxel, as NCTPlan reconstruction algorithm does, the new strategy is *to assign it to the barycenter of the portion of the geometry contained in the voxel*. This gives as a result, a very accurate estimation of average fluences in boundary areas and also improves the punctual estimation of the fluence. The performance of this new strategy will be presented for reference problem #1 described in section 3.3.

4.3 Material percentage rounding

In all the previous reasoning, the effect of material percentage rounding was intentionally neglected. By the material assignment procedure described in Chapter 3, the infinite p centimeter thick slab ($0 < p < 1$) leads to a homogenized mixture in which the proportion of slab material M is rounded to a multiple of 0.2. Clearly, the effect of rounding is greater when p is an odd multiple of 0.1. In these cases, the algorithm rounds down 0.1 the proportion of slab material and rounds up the proportion of air (see section 3.2.2). Note that from all odd multiples of 0.1, the one in which rounding has a more drastic

effect is the case $p = 0.1$, since after rounding, the mixed material is only air.

To quantify this in an example, assume that p is an odd multiple of 0.1, the particle source is planar and monodirectional, and that incident particles hit the slab surface perpendicularly and have at most one scattering reaction inside the slab. From equation (4.7), the relative difference between the average fluences for p and $p-0.1$ can be obtained. This relative error is a decreasing function of p for $0.1 \leq p \leq 1$ (see Appendix B). Consequently, to estimate the error caused by rounding, it is enough to deal with the case $p = 0.1$.

The calculation of the error caused by rounding for $p = 0.1$ is now presented. As mentioned above, the voxel model of a 0.1 cm thick slab of material M is a 1 cm thick slab of air. The average fluence in a homogenized cell (1 cm^2 of cross section and 1 cm thick) is proportional to the quotient between the mean track length in the cell and the volume of the cell. Since in air it can be assumed that there are no scattering reactions, the average fluence per particle entering the cell is 1 cm^{-2}. On the other hand, the average fluence in a portion 1 cm^2 of cross section and 0.1 cm thick of the real slab can be estimated as in the example. The assumption of at most one scattering reaction inside the slab is readily fulfilled for neutrons in the case $p = 0.1$ (this is shown in Table B.1 of Appendix B). Then, from Eq. (4.7), the average fluence per particle entering the cell is

$$\frac{\overline{\Phi}}{N} = \frac{1}{0.1\,\mathrm{cm}^3}\left(0.2\ \mathrm{cm} - \frac{1}{\Sigma^M} + \frac{e^{-0.1\mathrm{cm}\ \Sigma^M}}{\Sigma^M}\right) \tag{4.10}$$

$$= \left(2 + \frac{e^{-0.1\mathrm{cm}\ \Sigma^M} - 1}{0.1\mathrm{cm}\ \Sigma^M}\right)\frac{1}{\mathrm{cm}^2}. \tag{4.11}$$

Since the exponent in Eq. (4.10) is small, the second order expansion of the exponential can be applied to obtain that this last expression is approximately $\left(1 + 0.1\mathrm{cm}\ \Sigma^M/2\right)$ cm^{-2}. Therefore, the relative error due to rounding is

$$\frac{1 + 0.1\mathrm{cm}\ \Sigma^M/2 - 1}{1 + 0.1\mathrm{cm}\ \Sigma^M/2} = \frac{0.1\mathrm{cm}\ \Sigma^M}{2 + 0.1\mathrm{cm}\ \Sigma^M}. \tag{4.12}$$

For values of Σ^M between 0 and 2 cm^{-1}, this represents in the worst case an error of 9%.

The derivation of equation (4.12) involves several assumptions. However, numerical MCNP simulations for a slab of variable thickness p cm ($0.1 < p < 1$), irradiated with two different neutron beams (a 5 keV monodirectional neutron beam of 10 cm radius and the RA-6 BNCT reactor source), show the decreasing behavior of the relative error as a function of p, and maximum errors of 7.9% and 9.7% for the case $p = 0.1$, respectively (see Appendix C for details). Again it should be stressed that these simulations are quite general considering ideal and real neutron sources and all possible reactions in the medium.

Finally, it is worth noting that with minor changes, the rounding error analysis can be carried out for any voxel cell size and any rounding percentage p. For example, equation (4.12) shows that the error due to rounding is approximately proportional to the rounded percentage. Therefore, this error can be reduced to a half by rounding material proportions to the closest 10% (instead of the closest 20%), and to a quarter by rounding to the closest 5%. As a counterpart, the number of mixture materials to handle would substantially increase: they would be 286 and 1771 respectively.

4.4 Reassignment strategy results for surface voxels

The performance of the reassignment strategy is now presented for the parallelepiped phantom (see reference problem #1, section 3.3). Figure 4.3 illustrates the operation of the strategy proposed in section 4.2 to improve the prediction of the punctual and average fluences within the first millimeters of the phantom surface. As can be observed, the thermal neutron fluences computed by the original voxel method for the parallel positions of the parallelepiped phantom (positions 0, 2, 4, 6 and 8) overestimate the reference values within the first 4 millimeters. The percentage relative differences between the

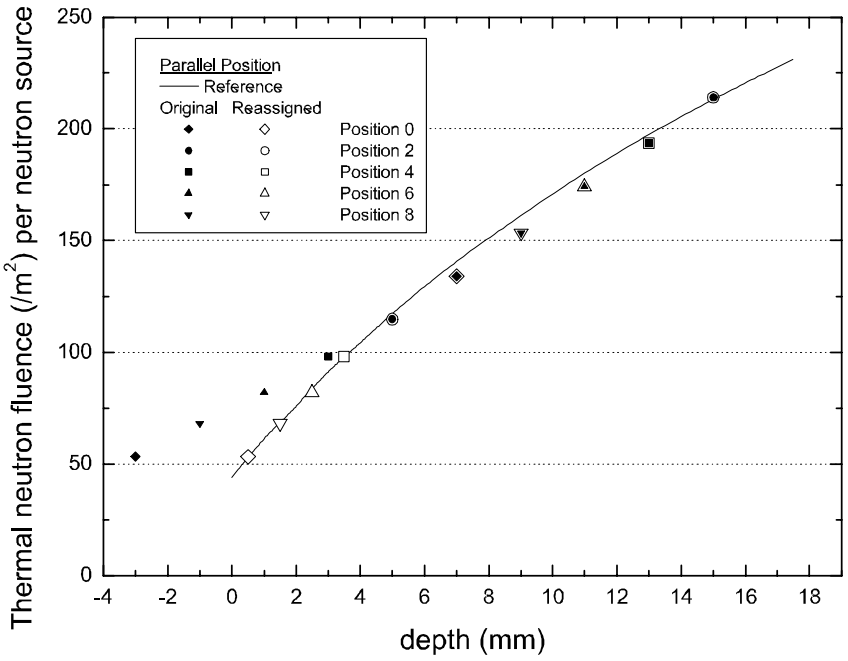

Figure 4.3: Comparison of the original and reassigned thermal neutron fluences in the first millimeters of the phantom surface. Reference corresponds to MCNP punctual estimation

original voxel model data and the punctual fluence (Reference) range from 54% at 0 mm depth to 5% at 4 mm depth. However, these differences would be smaller if they were computed using an averaged fluence as the reference (1 cm^3 averaged tally). As shown in Fig. 4.3, when the new strategy is applied to compute fluence values at shallow depths, the agreement between Reference and the reassigned data is excellent. Percentage relative differences between these latter are 2% on average for positions 0, 2, 4, 6 and 8, and 12% on average for the remaining five positions. Note that for the odd grid positions, the differences between real and rounded material percentages in surface cells are maximum. If material percentages were not rounded for these cases, the resulting average deviation would be as low as for the even positions. These results show that the deviation of the original voxel model from Reference, though unavoidable, is not only due to the homogenization in surface cells but also (and mainly) to the assignment of the average values to the center of the cells. It is important to remark that the largest deviations for

the original assignment (e.g., 54%) are forced by positioning the phantom with respect to the grid in a most disadvantageous way, i.e., cells at the beam entrance do not minimize the proportion of air. As a consequence, even if the rule to minimize the proportion of air at the beam entrance by adequately positioning the phantom are not followed, accuracy is obtained with the proposed reassignment.

Although the parallelepiped phantom in the angular position does not satisfy the conditions of the analysis leading to the reassignment, the new strategy can be used to adjust the punctual fluence in cases in which the geometric center of the surface voxel lies outside the phantom. For these cases, the percentage relative differences between the original voxel model data and the punctual fluence range from 140% to 56%. Again, the voxel method overestimates reference values. The same holds when the 1 cm^3 averaged fluence is used as the reference, but the maximum deviation is 32% in this case. Applying the strategy to reassign fluence values at shallow depths, the absolute value of the percentage relative differences decrease to 14% on average, with a maximum value of 23% at the surface of the phantom. Again, the largest deviations are intentionally obtained by positioning the phantom against the rules described above.

4.5 Discussion

In standard treatment planning systems for conventional radiotherapy, the time spent in dosimetry calculations is around 5 minutes. On the other hand, for a typical BNCT treatment plan, 50 million particle histories are usually tracked. This derives statistical uncertainties of 0.1% and 2.5% for high and low dose regions, respectively. The process of photon and coupled neutron-photon fields takes approximately 2 hours on a 2.4 GHz Pentium IV processor with 512 Mb RAM. This execution time is achieved using a modified version of MCNP4B, and it can be reduced if calculations are processed on a cluster of computers [39]. Since the factor of speedup is roughly the same as the number of computers used, a runtime similar to that involved in conventional radiotherapy could be

attained. In attempting to improve the accuracy of the voxel model, two lines of action naturally arise: to reduce the 20% step used for rounding material percentages and to decrease the voxel size.

A reduction in the rounding percentages increases the number of material mixtures to be considered in calculations. If the percentage step is set to 10%, the resulting number of materials is 286. The impact of this change in the computing time is not important, but the amount of memory utilized by the Monte Carlo code considerably increases. However, this should not be a problem for a reasonable modern computer and, as described in section 4.3, this change could reduce relative errors to a half in some surface areas. A percentage step of 5% would produce 1771 different material mixtures, which is impractical from the point of view of computation time and memory usage.

In Ref. [41], Goorley *et al.* have studied the effect of decreasing the voxel size in the Snyder model. They have shown that MCNP execution times and required memory significantly increase if voxel size is reduced. For example, the improvements in dosimetry results are small for a 4 mm voxel model over the 8 mm, and the memory required increases of about 6 times. In Ref. [62], Kumada *et al.* remarked that a reduction in the voxel size could lead to better results in the surface, but they reported that calculations performed with a voxel side of 0.5 cm would take approximately 10 times as long as with the 1 cm^3 voxel. These drawbacks to the downsizing of the voxel size are important and contrast to the minimum computational cost of the reassignment strategy presented in this chapter. Another important point to consider for the voxel size selection, and thus the tally volume, is related to the size of the sensitive volume of ionization chambers employed in experimental measurements. The output current represents a spatial averaging of neutron-photon interactions occurring in a typical volume of the order of centimeters [7]. Therefore, any reasonable comparison between experiment and calculation should involve tally volumes of this order of magnitude.

Another procedure to improve the accuracy at the surface follows from the results

presented throughout the previous and present chapters. It is a simple rule that does not affect the execution time and memory usage. The anatomy images should be positioned with respect to the voxel grid in such a way that cells at the beam entrance point are filled with a mixture with minimum proportion of air. NCTPlan allows the user to examine the voxelized model, indicating the material mixture produced for each cell in it. The fact that the relative error caused by rounding decreases as the material proportion p increases (or the same, as the proportion of air decreases) clearly supports this rule.

4.6 Concluding remarks

In all BNCT treatments carried out at present, the skin is considered one of the organs at risk. Moreover, in the case of cutaneous melanoma in extremities, skin is essentially the organ that limits the delivered dose to the patient. Since surface boundary areas are those where homogenization can have a more distorting effect, the performance of the voxel model in these regions was analyzed with special emphasis in this chapter.

A theoretical analysis was carried out to assess the distortion caused by homogenization and also to estimate the errors due to the materials percentage rounding process. Based on this analysis, a new strategy for the treatment of surface cells was proposed without any detriment to MCNP execution times. The performance of the new strategy was tested in two irradiation problems. For the parallelepiped phantom in parallel position, the large thermal neutron fluence deviation present at shallow depths (from 54% at 0 mm depth to 6% at 4 mm depth) was reduced to 2% on average. Reassigning fluence values in the case of the phantom in angular position produced the maximum deviation in the thermal fluence to decrease from 140% to 23% at the surface of the phantom. This case of sharp angle corners represents, however, an extreme limit of those encountered in clinical situations.

The previous and present chapter results suggested a rule to position images with respect to the grid in order to get the best performance. Even if these rules are not

followed, as in the cases just presented, the reassignment provides very accurate estimates.

The mentioned results represent a substantial improvement to the performance of the NCTPlan voxel model in surface areas. Since the NCTPlan TPS is currently used in several BNCT projects, and in particular in the cutaneous melanomas protocol of extremities in Argentina, the new strategy will be implemented in the newer version of the NCTPlan code.

Chapter 5

Clinical trials at the RA-6 reactor

As introduced in previous chapters, metastatic melanoma remains a highly lethal disease, with an incidence that continues to increase faster than any other cancer. Almost all adjuvant treatments fail to control this malignancy [82]. If proven effective, Boron Neutron Capture Therapy would represent a potentially useful modality for treating this disease [29].

In an effort to evaluate the applicability of using a nuclear research reactor for the treatment of cutaneous melanomas, the Comisión Nacional de Energía Atómica of Argentina has developed a new BNCT facility at the RA-6 reactor in the Centro Atómico Bariloche. The first BNCT facility was built a few years ago, and it was developed as an epithermal beam [6, 14]. This facility was used for *in vivo* experiments with small animals [23, 61]. Recently, the original epithermal beam has been thermalized, resulting in a mixed beam -named *hyperthermal* beam- of lower-energy neutrons, and thus with a lesser degree of penetration into tissues. Since the hyperthermal beam configuration has been designed to optimize the dose distribution at 1 cm depth, this beam is expected to inure to the benefit of surface tumor treatments [13]. However, the clinical efficacy of this beam under the BNCT modality for cutaneous melanomas will depend not only on beam quality but also on the boron compound distribution.

In 2003, the CNEA-Instituto Roffo Phase I/II clinical trial of BNCT was approved by the Administración Nacional de Medicamentos, Alimentos y Tecnología Médica (ANMAT # 3976, 2003) and by the Autoridad Regulatoria Nuclear (ARN #21190, 2003). The protocol was designed to evaluate the efficacy and toxicity of BNCT for cutaneous skin melanomas in extremities. Eligible patients are included if their melanomas are either unresectable or resectable but surgery is not feasible due to the presence of multiple lesions, and such patients are not receiving local radiotherapy and/or any systemic treatment for such disease. In addition, all patients to be included in the trial are required to sign an informed consent form.

Between October 2003 and April 2005, three patients with biopsy-proven nodular melanoma of the extremity were treated to six separate sites as part of the Phase I/II BNCT clinical trial. This chapter reports on the first skin melanoma treatments performed at the RA-6 BNCT facility. Those treatments whose results are used in the following chapters will be described in detail. Since clinical trials involve different areas of preparation, the main foci of beam design/dosimetry and treatment planning approach are discussed, including a brief description of the BNCT procedure in Argentina.

5.1 RA-6 Reactor

5.1.1 Beam design

RA-6 is a pool type reactor, with 500 kW of nominal power, and fuel 90% enriched in U235. In 2001, the original epithermal beam was modified to produce the current hyperthermal neutron beam, that provides a thermal neutron flux peak with about 1.0 x 10^9 cm^{-2} s^{-1} at approximately 1 cm depth.

In the design of the beam two boundary requirements were considered: to use the same internal filter of the epithermal beam, and to have easily removable modifications to restore the epithermal beam. The beam port configuration of the BNCT facility is shown

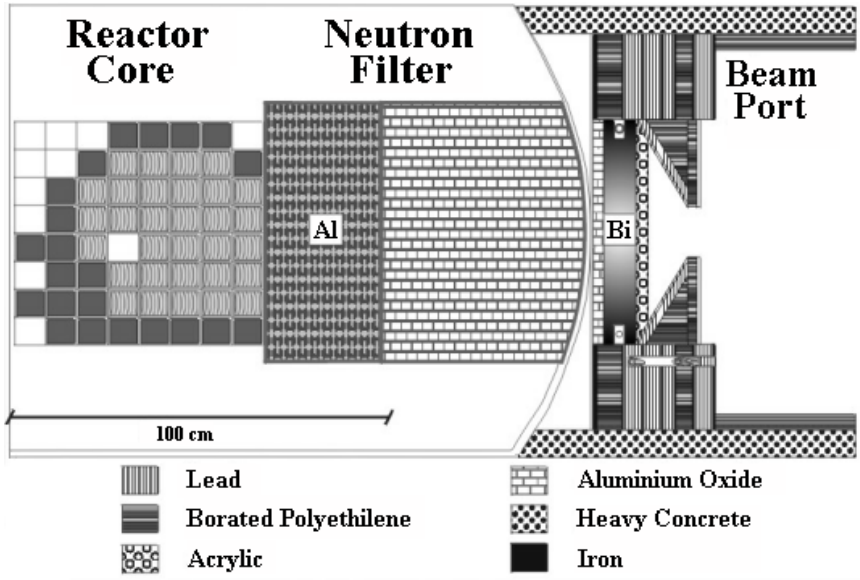

Figure 5.1: Scaled, schematic representation of the RA-6 BNCT facility showing the main components of the beam port.

in Fig. 5.1. The primary neutron filtering and moderating materials used in the beam line are aluminum and aluminum oxide. The acrylic cylindrical block of 62 cm in diameter and 3 cm thick, just downstream of the final bismuth gamma shield can be inserted or removed to produce a hyperthermal or epithermal neutron beam, as desired [7, 13]. The array of the selected materials provides the desired beam tuning, collimation as well as shielding outside the beam.

5.1.2 Beam model and physical dosimetry

In order to determine the RA-6 source model and reference physical dosimetry for treatment planning calculations with NCTPlan TPS, a series of coupled computations and measurements were performed using MCNP4C radiation transport code [9], and standard phantoms and measurement methods [7].

Neutron and photon distribution sources were defined on a disk of 15 cm radius and have circular symmetry. Both distribution sources follow the same discretization scheme.

The total source intensity is sampled from a relative frequency histogram of 20 radial bins. Within each radial bin, the positions of the particles are sampled from a distribution that is a function of the distance from the particle to the beam center. Energy and angular distributions are provided for 4 radial intervals, with limits at 5, 7.5, 10 and 15 cm. For each of these intervals, the relative frequency of 49 energy groups is given. These multiple energy bins are different for neutrons and photons. In addition, for each radial interval, 3 different angular distributions were calculated: one for thermal neutrons (0-0.5 eV), one for epithermal neutrons (0.5 eV-10 keV), and one for fast neutrons (10 keV-17 MeV). Regarding photons, the energy limits considered have been 0.6 MeV, 3 MeV and 10 MeV. All angular distributions (i.e., the distribution of angles between the particle direction and a vector normal to the source surface) are given in 10 angular sectors with the same probability.

The source verification and normalization process was carried out using the experimental dosimetry derived in the cubic water phantom (see section 3.5.1). As described in Chapter 3, dose and neutron flux-depth distributions produced by the RA-6 hyperthermal beam were also measured in a cylindrical water-filled phantom. Since this geometry represents a suitable approximation for extremities, this system was selected as a reference for performing the beam physical dosimetry, along with the cubic phantom.

5.2 Computational dosimetry for cutaneous melanoma patients

In order to compute the dosimetry for skin melanomas patients, the following assumptions regarding materials compositions, kerma factors, RBE and CBE factors, and tolerance and therapeutic doses were made.

5.2.1 Materials

Three material types were chosen to model peripheral melanomas: air, muscle and bone. Air composition was taken from Chadwick *et al.* [17]. Muscle and bone compositions were taken from ICRU reports 44 and 46 [50, 51], and correspond to adult muscle and adult femur compositions, respectively. The bases for selecting muscle as a representative material for soft tissue are as follows.

As described by Goorley *et al.* [41], while variations in the hydrogen concentration can affect neutron transport due to its large cross section and high atomic density, small variations in nitrogen will have little impact. Therefore, as hydrogen concentration and density are almost the same for muscle and skin ($\sim$ 10% by mass, $\sim$ 1.05 g/cm^3), no significant difference should be expected in terms of particle transport assuming that all soft tissue is muscle. Melanoma elemental composition, as described by Maughan *et al.* [71, 72], has on average 9.4% of hydrogen content and 1.04 g/cm^3 of physical density. Thus, differences between muscle and melanoma hydrogen density are no greater than 0.8% resulting in a relatively negligible effect from the radiation transport viewpoint.

5.2.2 Kerma factors

The neutron kerma factors used to convert neutron flux into absorbed dose rates were derived from ICRU 63 elemental kerma data, as described in Ref. [41]. Adult skin composition taken from ICRU report 46 was the tissue type used to specify absorbed dose rates [51]. Two different considerations motivated this selection. First, the organ at risk (OAR) considered by physicians when treating peripheral melanomas is the skin. Second, skin has the highest nitrogen content compared to muscle and bone. As variations in nitrogen proportionally change thermal neutron kerma factors and consequently the derived dosimetry, selecting skin kerma factors will always overestimate absorbed doses in muscle and bone. It should be noted that this does not apply to melanoma tissue type. Maughan *et al.* reported 5.6% and 5.9% of nitrogen content for two melanomas

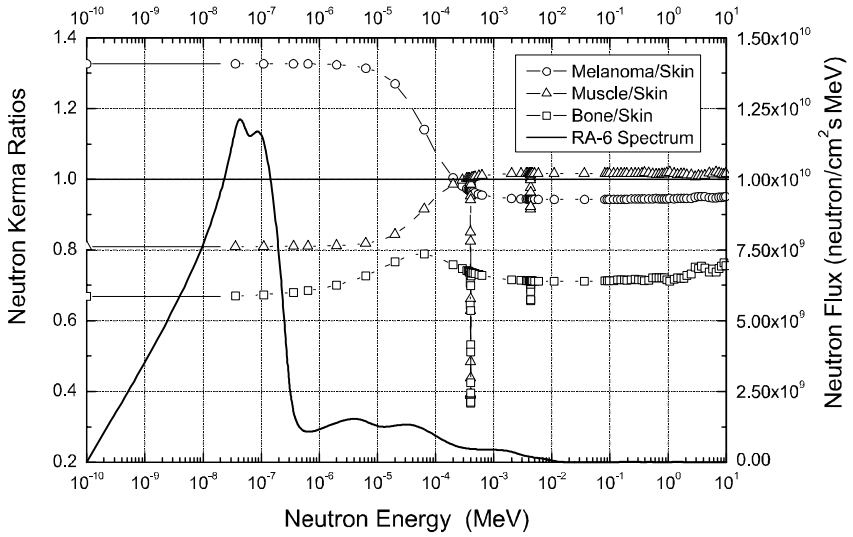

Figure 5.2: Neutron kerma ratios for melanoma, muscle and bone to skin tissue types. The RA-6 neutron source is shown as a function of particle energy in MeV and it is referred to the right Y-axis. In the neutron energy range of 10^{-10} and 10^{-4} MeV, muscle-to-skin and bone-to-skin kerma ratios are less than one while melanoma-to-skin is greater than one.

of different histologies [71]. Hence, the nitrogen content of this tissue type is on average 33% higher than that of skin. Therefore, the thermal neutron dose that arises primarily from $^{14}\mathrm{N}(\mathrm{n},\mathrm{p})^{14}\mathrm{C}$ reaction will be underestimated in the tumor.

Figure 5.2 shows neutron kerma ratios for melanoma, muscle and bone tissue types to skin tissue type. The energy distribution of the RA-6 neutron source is also shown in the plot. In the range of 10^{-10} and 10^{-4} MeV neutron energies, where the most significant part of the neutron spectrum is located, both muscle-to-skin and bone-to-skin kerma ratios are less than one. In contrast, for the same energy range melanoma-to-skin neutron kerma ratio is greater than one, reflecting that the elemental composition of melanoma tissue has a higher nitrogen content than that of skin. Although changes in the energy distribution of the neutron source are expected due to neutron interactions with the medium, only moderation effects will occur leading neutrons to a lower energy range. Thus, an overestimation of absorbed doses in muscle and bone -as well as an underestimation of doses in tumor- should be expected accordingly, if only skin neutron

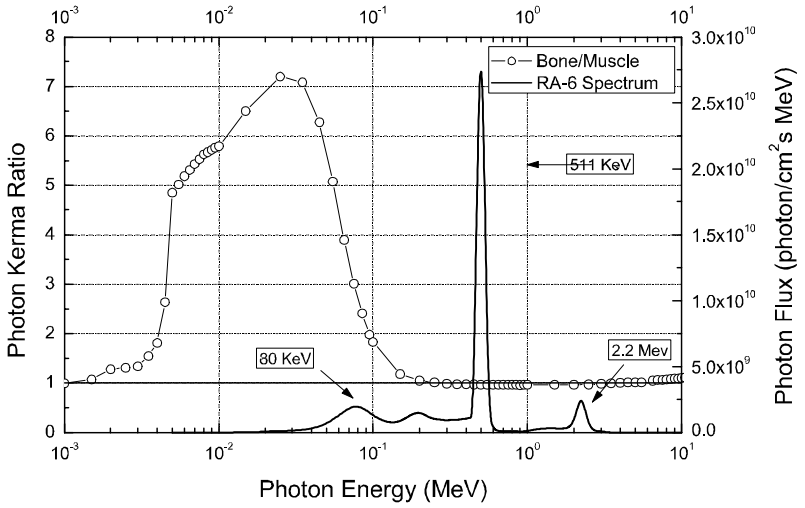

Figure 5.3: Photon kerma ratio between bone and muscle tissue types. The RA-6 structural photon source is shown as a function of particle energy in MeV and it is referred to the right Y-axis. Differences between kerma factors are evident for photon energies in the range of 1 and 200 keV where the kerma ratio is greater than one.

kerma factors are taken into consideration.

Muscle photon kerma factors used in calculations are derived from the mass energy absorption coefficients (μ_{en}/ρ) reported in Attix, appendix D.3 [1]. Since the values of μ_{en}/ρ depend on the atomic number of the material, some differences will be expected between muscle and bone photon kerma factors. The incidence of using muscle instead of bone kerma factors in the computed structural photon dose rates was estimated by integrating each material kerma factor times the RA-6 structural photon source. Differences of 1% were found in the dose rate estimations, showing that the effect of considering muscle instead of bone kerma factors is negligible from the perspective of dose calculation.

Figure 5.3 shows the ratio between bone and muscle photon kerma factors versus energy in MeV. The energy distribution of the RA-6 structural photon source is also shown in the plot, and it is referred to the right Y-axis. Differences between kerma factors are evident for photon energies in the range of 1 and 200 keV where the kerma ratio is much greater than one. The main contribution to the difference in the absorbed

RBE/CBE Factors	Skin (Normal Tissue)	Melanoma (Tumor Tissue)
Photons	1	1
Thermal Neutrons	3	3
Fast Neutrons	3	3
Boron Reaction	2.5	3.8

Table 5.1: RBE and CBE weighting factors assumed for normal skin and malignant melanoma [20, 29, 34].

doses based on muscle instead of bone comes from low energy photons (50-200 keV). However, due to the characteristics of the RA-6 photon spectrum, this difference is no greater than 1%. Prompt gammas, which are produced mainly by neutron capture in hydrogen, will also contribute to the photon dose component. Nonetheless, as induced photons contribute to the high-energy peak of 2.2 MeV, negligible differences should be expected. Pair production due to 2.2 MeV photons is not important for low-Z materials such as biological tissues. Thus, its contribution to 511 keV peak will be negligible.

Boron kerma factors computed from the ENDF/B-VI nuclear data library [86] for the $^{10}\mathrm{B}(\mathrm{n},\alpha)^{7}\mathrm{Li}$ reactions were used to estimate the boron dose component.

5.2.3 Biological effectiveness factors and boron concentrations

To calculate the biologically weighted dose (RBE Gy), RBE and CBE weighting factors listed in Table 5.1 were assumed [20, 29, 34].

In most BNCT clinical trials mediated by the administration of BPA-F complex, the estimate of the boron concentration in skin and tumor tissues is based on the $^{10}\mathrm{B}$ concentration in blood, and relies on the assumption that its level can be described as single static ratios, named skin-to-blood and tumor-to-blood $^{10}\mathrm{B}$ concentration ratios. Based on Fukuda's work [31], these ratios were assumed to be 1.5 and 3.5 for skin and tumor, respectively.

5.2.4 Tolerance and therapeutic doses

It was mentioned above that skin is considered the critical normal structure (OAR). As the CNEA melanoma clinical trial is a Phase I/II, the maximum tolerable dose (MTD) for skin was adopted as a therapeutic dose, regardless of the boron concentration in tumor. To evaluate the dose distribution in the skin, a superficial 5 mm thick layer of tissue is considered.

According to the skin toxicity analysis of Douglas with photons [26], Fukuda *et al.* assumed 18 RBE Gy as the MTD in skin for a field size of 100 cm^2 [29]. Although this tolerable dose corresponds to a uniform dose distribution over the field size, it was considered the starting point for the dose prescription in the clinical trials of Argentina. It is known that the skin tolerable dose decreases as the field size increases [21]. The beam aperture of the RA-6 reactor is 15 cm in diameter and, as a consequence, it would represent at least a field size of ~ 176 cm^2. Thus, the empirical model proposed by Cohen and Kerrich [21] was used in order to scale the value of 18 RBE Gy. The empirical model states that dosage is adjusted for field size by a factor Z^y, where Z is the field length (or side of equivalent square) and $y = -0.33$ for skin. As a result, a value of ~ 16.5 RBE Gy was obtained and applied to the first BNCT treatment in Argentina. Regarding the tumor control dose, 20 RBE Gy was the dose assumed for a 90% of tumor control probability in lesions with mean diameters of 1 cm or lower [29].

5.3 Overview of a BNCT treatment

The procedure begins at the radiation oncology department of the Instituto Roffo, where candidates are proposed to subject themselves to BNCT for palliative radiotherapy, pursuant to the CNEA-Roffo Phase I/II clinical trial for extremity skin melanomas. Informed consent forms are provided to subjects for their review, and all questions are answered prior to any involvement in the study. Subjects who decide to participate in the study

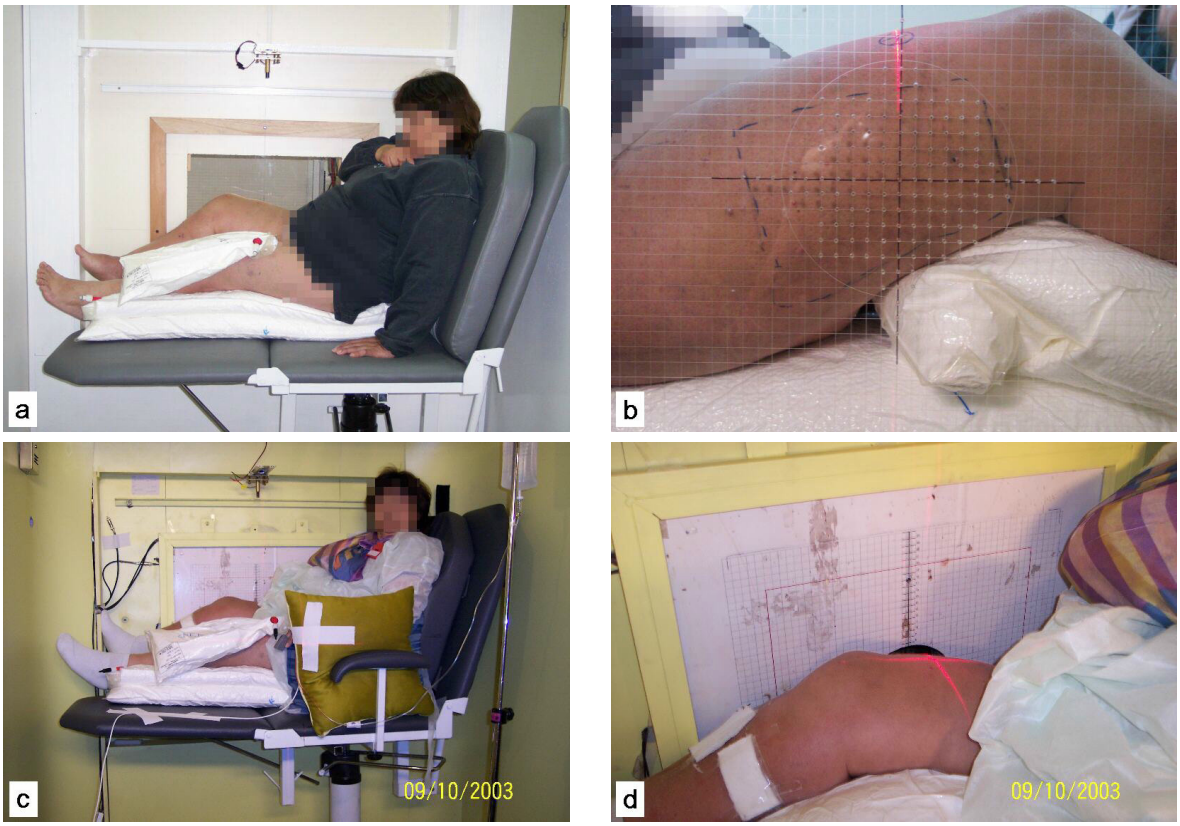

Figure 5.4: (a) Patient positioning at the SR, (b) beam's eye view at the SR, (c) patient set up at the IR, and (d) reactor exit port at the IR.

are required to sign the informed consent document.

Once a subject is enrolled in the clinical trial, the first step is to determine the positioning of the patient. This procedure is carried out at the Centro Atómico Constituyentes in Buenos Aires. The positioning is determined in a simulation room (SR) that replicates the geometry of the BNCT irradiation room (IR) at the reactor. As shown in Fig. 5.4, the SR presents the additional advantage of a beam's eye view through a transparent acrylic window. This window is gridded with a reference X-Y coordinate system that mimics the gridding at the reactor exit port (see Figs. 5.4 [b] and [c]). A series of holes machinated through the acrylic window allows marking the patient's skin for reference purposes, and determining distances in the beam direction (Z-axis) to each external skin mark.

After the radiation oncologist defines the region to be treated, the optimal patient position for the treatment is determined and fixed by means of positioning devices. Reference marks are set in accessible and accurate positions for repositioning in the IR, and radio-opaque fiducial markers are placed for computational dosimetry, which allow to define the orientation of the beam axis for treatment planning.

Once the patient positioning was determined in the SR, a planning CT study of the patient's extremity is performed, trying to reproduce the same deformation of the anatomy with the help of the positioning devices and fiducial markers. A set of 125 contiguous 2 mm CT scans of the patient anatomy is acquired by a helicoidal scanner and subsequently images are cleaned and processed to be used in the treatment planning system. Dose calculations and treatment plan evaluation are performed using the NCTPlan v. 1.3 treatment planning system [37], and the DVH Tool system [38] (a code developed by CNEA specifically for the calculation of Dose-Volume Histograms (DVH) in BNCT). Based on the CT study of the patient's extremity and an average concentration profile of ^{10}B in blood, treatment plans are obtained subject to the above-mentioned assumptions. The irradiation time is computed by integrating the boron-dependent maximum dose rate times the average ^{10}B concentration profile to obtain the prescribed MTD. The time-to-MU conversion factor is obtained from the reading of the beam monitoring fission chamber at the reactor reference power. To evaluate the dose distribution in the skin, a cumulative dose-volume histogram for a superficial 5 mm thick layer of tissue is computed.

The treatment team and the patient travel together to the Centro Atómico Bariloche and at the arrival day, a positioning set-up is implemented. Patient repositioning in the IR is accomplished by placing the patient and the positioning devices on the couch, and locating the external marks with reference to the grid (see Figs. 5.4 [c] and [d]). Fine adjustments to the patient's orientation are made, and the appropriate distances from each point to the grid are verified. On the following day, the patient is treated. Patients receive a 14 g m^{-2} BPA dose, infused intravenously over 90 minutes, and during this

time, blood samples are extracted in spans of 10-15 minutes. These samples are analyzed for boron content, and blood boron concentration values are plotted versus time. At the end of the infusion, and during patient preparation and positioning in the IR, additional blood samples are taken and analyzed until the start of irradiation. Based on the blood samples analyzed before the start of irradiation, which is approximately 90 minutes after the end of the infusion, a preliminary treatment time is computed. Since blood sampling during irradiation is not feasible, the open 2-compartment model developed by Kiger *et al.* [55] is employed to fit the boron concentration measurements in blood. While the BPA infusion is performed, the reactor is started up, and the beam monitoring system tested. Owing to the absence of a beam shutter, the reactor is then set to critical state at very low power, in order to allow access of personnel to the irradiation room for the patient positioning. Next, the reactor power is increased to its reference value, and the patient irradiation is performed until the updated monitor units are reached. Thus, the final MU value includes the patient exposition during the initial transient, and it is determined on the basis of the last blood sample once the irradiation has begun. During the course of the irradiation, two TV cameras and intercom, an EKG, and a pulse oximeter continuously monitor the patient. In order to estimate the gamma dose distribution on different parts of the patient's body, a set of TLDs 700 are utilized during each irradiation (typically located outside the external beam port).

After the irradiation, additional blood samples are taken every six hours allowing a retrospective evaluation of the treatment to be completed. Finally, the patient is hospitalized for medical supervision until the following day, when she/he and the treatment team travel back to Buenos Aires.

5.4 Irradiations

5.4.1 Patient #1

Clinical case and outcome

The subject was a 54-year-old woman who had her fifth toe of her right foot amputated on November 13, 1999, because of a skin melanoma 2 cm deep and 3 cm wide. In July 2001, she received a right-side groin dissection due to a 7-lymph-node massive metastasis. In January 2003, the patient developed multiple subcutaneous node involvement on the right leg. Owing to pain and bleeding caused by those nodes, the patient was examined at the radiation oncology department of Instituto Roffo for palliative radiotherapy. Since a multiple nodes progression at the level of the external face of her right thigh was observed, she was proposed to subject herself to BNCT.

Prior to BNCT, thirty nine melanoma nodules were clearly identified (Fig. 5.5 [a]). Only 25 of the nodules lay within the region defined by physicians as the target of the treatment. However, the 39 mentioned nodules were labelled and measured in size for tumor control and dose evaluation purposes. Tumor nodules were too small to appear in medical images. Then, to determine mean tumor diameters some approximations were applied. First, the superficial diameter of each nodule was measured assuming their shapes were well represented by small circles. Since tumor biopsies revealed that nodules were very shallow of 2 or 3 millimeters in depth, i.e. similar to their superficial diameters, each mean nodule diameter was assigned its superficial dimension. Local tumor responses at 3 months follow-up were assessed clinically by inspection and palpation by three different radiation oncologists (Fig. 5.5 [b]). Responses were graded based on standard World Health Organization (WHO) criteria as follows: CR = complete response (i.e., 100% tumor remission); PR = partial response (more than 50% tumor remission); NC = no change (from 50% tumor remission up to 25% tumor progression), PD = progressive disease (more than 25% tumor progression). Table 5.2 in page 99 summarizes details on

Figure 5.5: (a) Patient # 1 with a multiple node progression at the lateral face of her right thigh. Prior to BNCT treatment, 39 nodules of interest were labeled and measured in size, and (b) Response three months after BNCT (see Table 5.2).

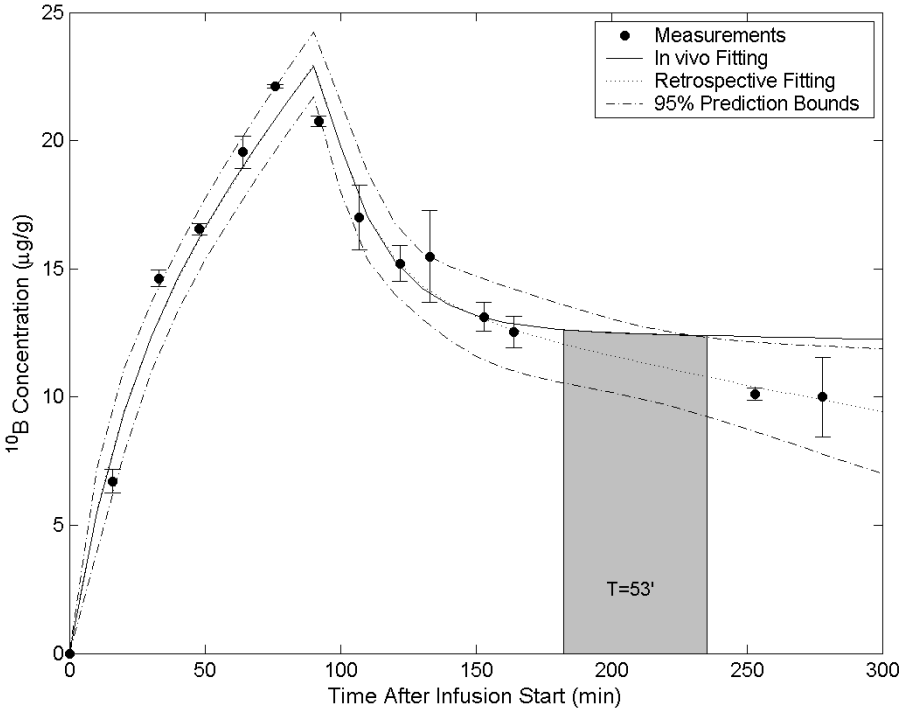

Figure 5.6: Measured blood ^{10}B concentration-time profile with the *in vivo* and retrospective fitted model results for patient #1. Predictions bounds at 95% level are shown for the retrospective curve.

tumor sizes and responses.

Skin and tumor doses: retrospective analysis

Figure 5.6 shows the measured concentration-time profile of ^{10}B in blood and the fitted model results. Blood samples taken up before the start of the irradiation were used to determine the model prediction of ^{10}B concentration for computing the irradiation duration. To achieve the prescribed MTD of 16.5 RBE Gy, the computed treatment time was 53 minutes. Based on the complete set of blood samples and the fitting with the 2-compartment model a retrospective estimation of the maximum dose delivered to the skin as well as the average doses to the nodules was carried out.

Tumor spatial coordinates are usually determined in the treatment planning system

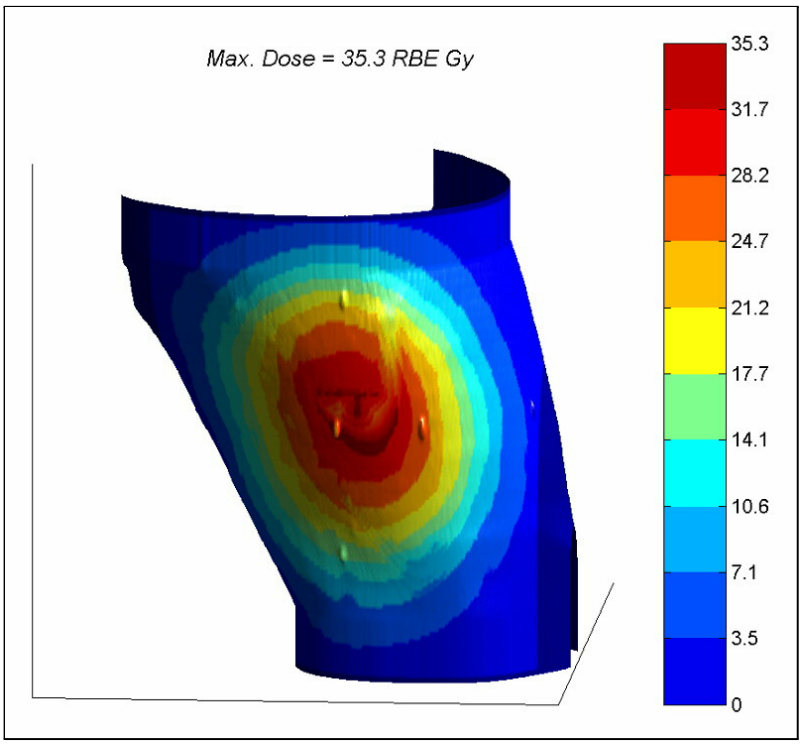

Figure 5.7: Surface tumor dose distribution for a 3.5 tumor-to-blood ^{10}B concentration ratio in patient #1.

from the ROIs delineated by physicians on CT images. In this particular case, delineation of tumors were not feasible due to their small size (see Table 5.2). Therefore, tumor doses were assumed uniform over each tumor volume, and were determined by superimposing the superficial tumor dose distribution on the picture of the patient's extremity. First, the patient anatomy was computationally reconstructed from CT scans using MATLAB software (The Mathworks, Natick, MA). Then, the dosimetry data output derived from NCTPlan was evaluated on the surface of the reconstructed anatomy for a 3.5 tumor-to-blood ^{10}B concentration ratio (Fig. 5.7).

For computing biologically weighted doses, assumptions described in section 5.2 were used. The average value of ^{10}B in tumor used for these calculations was computed based on the retrospective fitting shown in Fig. 5.6. Using fiducial markers as references, an image registration between the picture of the patient's extremity (Fig. 5.5 [a]) with the

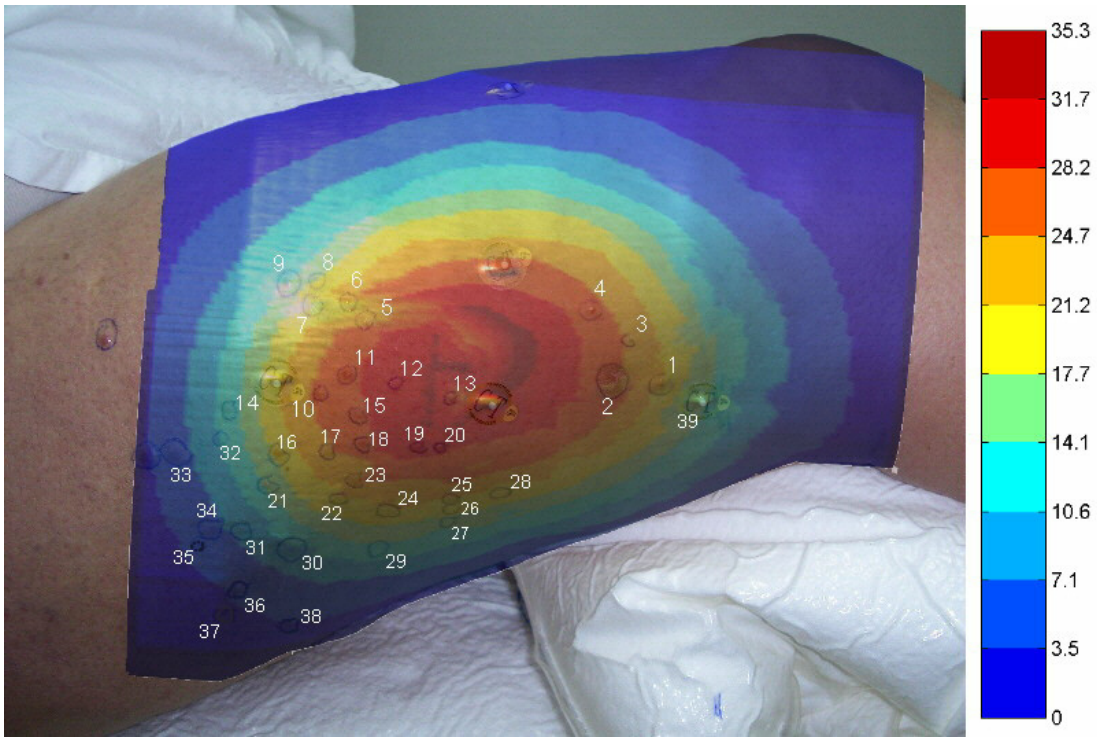

Figure 5.8: Surface tumor dose distribution superimposed on the patient's extremety prior to BNCT treatment.

dose distribution plot (Fig. 5.7) was performed. Figure 5.8 depicts the result of this procedure. From the detailed analysis of this figure, a set of 39 average tumor doses was derived.

5.4.2 Patient #2

Clinical case and outcome

The patient was a 75-year-old woman with a nodular melanoma progression at the front side of her inferior right leg. In June 2004, the patient was examined at the radiation oncology department of Instituto Roffo for palliative radiotherapy, and was proposed to subject herself to BNCT. At the time of the treatment, the patient presented 10 nodules at the target area, although a total of 12 were labelled and delineated on the CT scans

performed prior to the irradiation for evaluation purposes (Fig. 5.9 [a]). Tumor sizes were computed using the DVH Tool System [38].

Local tumor response at 14 weeks follow-up was assessed clinically by visual inspection, and verified by sequential CT scans. The standard WHO criteria described above was used to score responses (see Fig. 5.9 [b]).

Skin and tumor doses: retrospective analysis

According to the normal tissue dose escalation protocol, a MTD of 22 RBE Gy was prescribed to this patient. Figure 5.10 shows the measured concentration-time profile of ^{10}B in blood and the fitted model results. The resulting treatment time based on the blood samples taken up before the start of the irradiation was 76 minutes. Using the complete set of blood samples and the fitting with the 2-compartment model a retrospective estimation of the maximum dose delivered to the skin as well as the doses to the nodules was carried out.

NCTPlan TPS [37] was used to compute normal and tumor doses. The average value of ^{10}B in tumor used for these calculations was computed based on the retrospective fitting shown in Fig. 5.10. The 3D dose distribution for each nodule was obtained using the DVH System [38]. Then, maximum, minimum and mean doses could be determined in each volume of interest (VOI).

5.5 Dosimetry and clinical results

5.5.1 Patient #1

According to the retrospective analysis, the patient received a maximum dose to the skin of 15.8 RBE Gy, with a 95% confidence interval of [14.8, 16.8] RBE Gy which contains the prescribed MTD (16.5 RBE Gy). This interval was computed from the 95% prediction

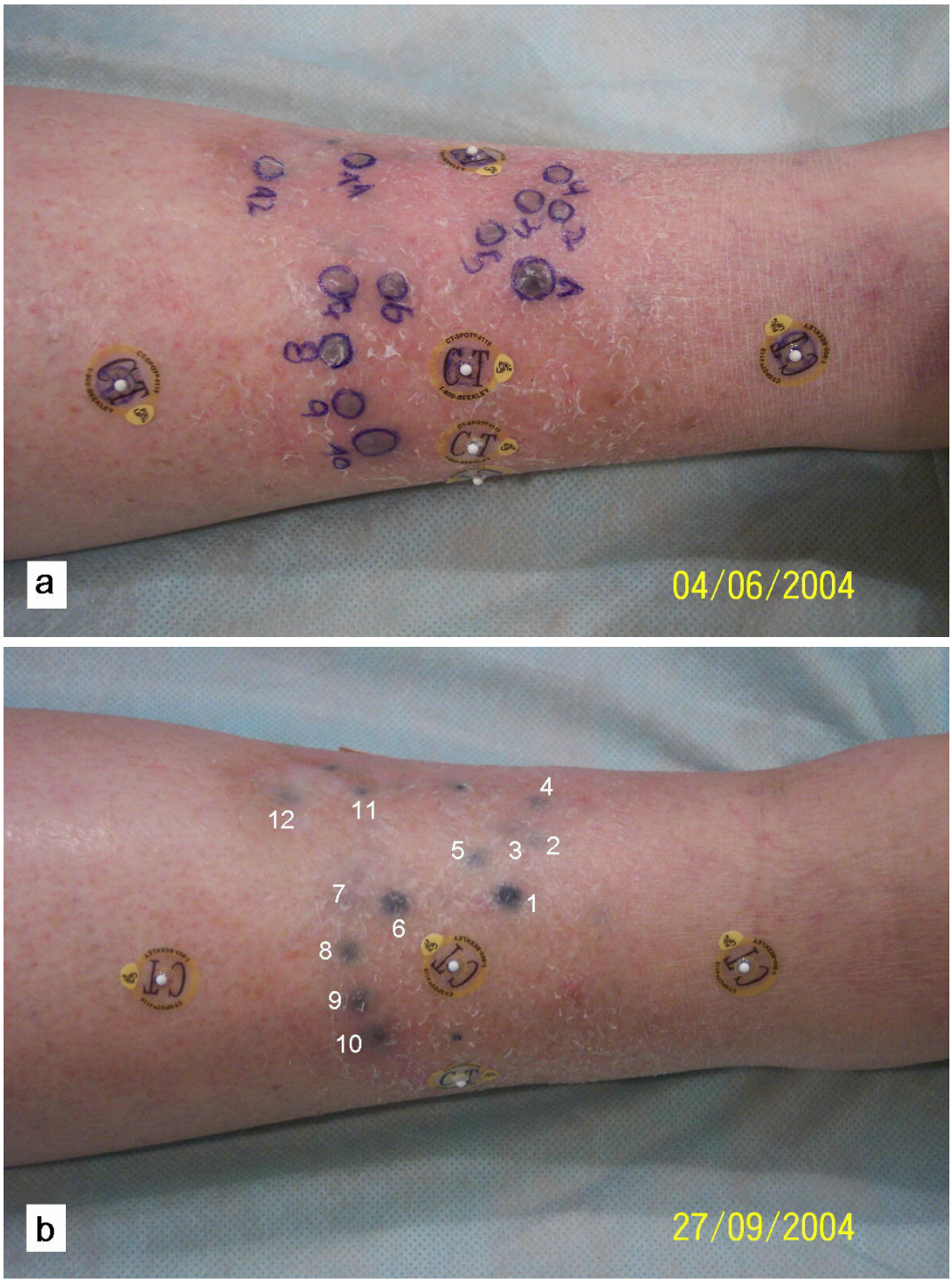

Figure 5.9: (a) Patient # 2 with a multiple node progression at the front side of her inferior right leg. Prior to BNCT treatment, 12 nodules of interest were labeled for evaluation purposes, and (b) Response fourteen weeks after BNCT (see Table 5.3).

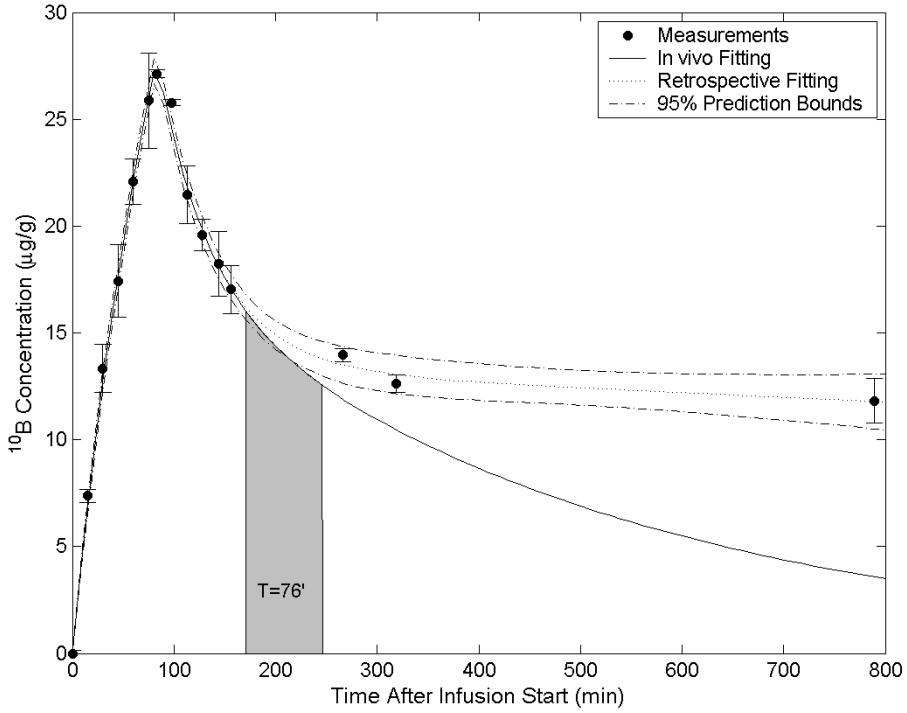

Figure 5.10: Measured blood ^{10}B concentration-time profile with the *in vivo* and retrospective fitted model results for patient #2. Predictions bounds at 95% level are shown for the retrospective curve.

bounds for the fitted curve (see Fig. 5.6). The mean of the maximum dose to the skin was 4.2 % lower than the MTD. This retrospective value corresponded to a mean skin ^{10}B concentration of 17.1 ppm which was 8.9% lower than the predicted value during the course of the irradiation. A grade 1 RTOG/EORTC skin acute reaction was detected after the first day of treatment, and the maximum radiation-induced reaction over 1 year follow-up was scored as dry desquamation. Table 5.2 presents the derived absorbed tumor dose for each of the 39 indexed nodules (see Fig. 5.8), along with original tumor sizes and tumor responses 3 months after BNCT.

As mentioned before, 25 out of 39 labelled nodules were considered the target of the treatment. After three months follow-up, 21 out of 25 nodules were in complete clinical response, 1 in partial response and the remaining with no change. As a consequence of

Nod. ID	d (mm)	Tumor Dose (RBE Gy)	Tumor response (3 months)	Nod. ID	d (mm)	Tumor Dose (RBE Gy)	Tumor response (3 months)
1	3.4	20.3	NC	21	2.7	13.2	NC
2	10.3	25.6	CR	22	2.9	20.3	CR
3	2.4	23.8	CR	23	3.0	22.0	CR
4	3.1	25.6	NC	24	3.7	20.3	CR
5	3.1	23.8	CR	25	4.0	20.3	CR
6	3.2	22.0	CR	26	2.2	18.6	CR
7	3.2	18.6	CR	27	2.1	15.0	CR
8	3.3	16.8	CR	28	3.4	20.3	CR
9	4.4	13.2	PR	29	3.7	11.5	CR
10	3.3	25.6	CR	30	4.5	9.7	NC
11	4.0	27.3	NC	31	3.4	7.9	NC
12	2.8	29.1	CR	32	3.2	9.7	PR
13	2.7	30.9	CR	33	5.2	6.2	NC
14	3.7	11.5	CR	34	4.1	6.2	NC
15	2.9	27.3	CR	35	2.2	4.4	PD
16	3.5	16.8	NC	36	4.0	4.4	PD
17	2.8	23.8	CR	37	3.3	2.7	PD
18	3.5	25.6	CR	38	3.0	2.7	PD
19	2.8	29.1	CR	39	2.5	16.8	NC
20	2.8	29.1	CR	—	—		———

d = mean tumor diameter; CR = complete response; PR = partial response; NC = no change; PD = progressive disease.

Table 5.2: Details on tumor sizes, doses and responses for patient #1.

these encouraging results, a second irradiation was performed in a different location of the extremity of the same patient two months after the first irradiation. The prescribed MTD was 20 RBE Gy and the actual maximum dose delivered to the skin was 18.5 RBE Gy (this is, the expected value of the maximum dose to the skin). Owing to the large disease progression outside the irradiated field, the observation time for in-field progression was very short (less than 2 months). Again, a very low toxicity to the normal skin was observed. Regarding tumor responses, 12 out of 21 nodules had an objective local tumor response (CR+PR) and 9 had no change. It should be stressed that most of the mean

Nod. ID	v (cm^3)	d (mm)	Tumor Dose (RBE Gy)	Tumor response (14 weeks)
1	0.46	9.5	[45.9, 53.5]	NC
2	0.09	5.6	[32.6, 36.9]	CR
3	0.21	7.4	[30.7, 37.3]	NC
4	0.41	9.2	[20.6, 30.3]	NC
5	0.30	8.3	[38.0, 45.0]	NC
6	0.29	8.3	[47.7, 56.0]	NC
7	0.66	10.8	[45.0, 54.0]	NC
8	0.19	7.2	[47.7, 55.0]	PR
9	0.12	6.1	[47.6, 53.4]	NC
10	0.87	11.8	[37.6, 50.3]	NC
11	0.60	10.5	[18.4, 36.5]	NC
12	0.78	11.4	[16.5, 27.9]	PD

v = tumor volume;
d, CR, PR, NC, and PD as in Table 5.2.

Table 5.3: Details on tumor sizes, doses and responses for patient #2.

tumor diameters involved in the second irradiation were much larger (> 10 mm) than those in the first treatment.

5.5.2 Patient #2

On the contrary to the first irradiation, the predicted pharmacokinetic profile during irradiation was below the retrospective fitting (see Figs. 5.6 and 5.10). According to these results, the patient received a maximum dose to the skin of 22.6 RBE Gy, with a 95% confidence interval of [22.0, 23.3] which contains the prescribed MTD (22 RBE Gy). The mean of the maximum dose to the skin was 2.7% higher than the MTD. This retrospective dose corresponded to a mean skin ^{10}B concentration of 22.1 ppm which was 4.7% higher than the predicted value during the course of the irradiation. Dull erythema was observed one day after treatment (grade 1 RTOG/EORTC reaction). No skin toxicity was detected over seven months follow-up. Table 5.3 shows the original tumor volumes computed from

the contours delineated by physicians on CT scans. Assuming that each nodule can be represented as a sphere, approximated mean tumor diameters were computed from the original determined volumes. In this patient, each tumor dose is reported as an interval, ranging from the minimum to the maximum dose in the nodule (Table 5.3). Note that in BNCT the dose distribution varies significantly with depth, and then, the dose uniformity level present in conventional radiotherapy is virtually impossible to achieve, particularly in large tumor volumes. Local tumor responses at 14 weeks follow-up are shown in Table 5.3. The results of the treatment at this time showed stabilization of the disease in the target area and 1 complete remission. Owing to the slow evolution of the tumor response in this patient, physicians considered a 14-week follow up not enough time to assess the final treatment endpoint. Therefore, the clinical outcome of this patient is still under evaluation.

Chapter 6

Determination of tumor-to-blood ^{10}B concentration ratios

6.1 Introduction

It is widely known in radiotherapy that the probability of tumor control strongly depends on the absorbed dose in tumor tissues. In the particular case of BNCT, a large fraction of this dose is due to the densely ionizing particles that result from the reaction $^{10}\mathrm{B}(\mathrm{n},\alpha)^{7}\mathrm{Li}$. In most BNCT clinical trials mediated by the administration of BPA-F complex, the estimate of the boron concentration in tumor for treatment planning and during the irradiation of a patient is based on the ^{10}B concentration in blood, and relies on the assumption that its level can be described as a *single static* ratio, named tumor-to-blood ^{10}B concentration ratio. This ratio will be referred to as "tumor-to-blood ratio" or simply "the ratio".

Some authors have reported that *static* tissue-to-blood uptake ratios do not completely reflect the dynamic ^{10}B loading and washout behavior expected in tumor and normal tissues [55]. However, Fukuda *et al.* [31] measured skin-to-blood and tumor-to-blood ratios in melanoma patients, and observed a relatively constant value during 6 hours after

the end of the boron compound infusion. In addition, this assumption as well as the *single value* for the ratio have been accepted and applied so far, due to the difficulty of *in vivo* boron quantification in different tissues and volumes during the treatment. Therefore, the better this ratio is known, the more accurately the absorbed dose can be computed, and consequently, a more efficient treatment will be delivered.

In order to determine the tumor kinetics of the boron compound, and therefore the tumor-to-blood ratio, different groups have performed pharmacokinetic studies in tumor and blood tissues [11, 18, 31, 69]. In these studies, biopsy specimens are resected for boron analysis after BPA administration, and in some cases, patients must undergo surgery to obtain tissue samples. This technique to estimating the tumor-to-blood ratio is the most natural and direct. However, it is sometimes costly, time-consuming and invasive for the patient.

In this chapter, a new approach to determine the tumor-to-blood ^{10}B concentration ratio is presented. It consists of a maximum likelihood estimate [84] from the clinical outcome of a BNCT treatment. In other words, the estimated ratio is the value that makes the clinical output most probable or likely. The present estimation is based on the clinical outcome of the first skin melanoma BNCT treatment performed in Argentina [35], described in Chapter 5.

6.2 Procedures

6.2.1 Clinical case description

As described in Chapter 5, the first patient treated at the RA-6 reactor presented superficial nodular melanomas at the level of the external face of the right thigh. In this patient, the clinical response of 39 nodules was assessed at 3 months follow-up, and it was graded based on the standard WHO criteria (see Table5.2). For the purpose of the method that is introduced, tumor responses are interpreted in a binary fashion, i.e., as

Nod. ID	Tumor response (3 months)	Nod. ID	Tumor response (3 months)
1	Non-CR	21	Non-CR
2	CR	22	CR
3	CR	23	CR
4	Non-CR	24	CR
5	CR	25	CR
6	CR	26	CR
7	CR	27	CR
8	CR	28	CR
9	Non-CR	29	CR
10	CR	30	Non-CR
11	Non-CR	31	Non-CR
12	CR	32	Non-CR
13	CR	33	Non-CR
14	CR	34	Non-CR
15	CR	35	Non-CR
16	Non-CR	36	Non-CR
17	CR	37	Non-CR
18	CR	38	Non-CR
19	CR	39	Non-CR
20	CR		

d = mean tumor diameter; CR = complete response;
Non-CR = non-complete response (PR+NC+PD).

Table 6.1: Details on tumor responses for patient #1. See Table 5.2.

complete response (CR) for complete disappearance and regression of pigment plaque and tumor, and non-complete response (non-CR) otherwise. Following this scoring, clinical responses reported in Table 5.2 are rewritten as shown in Table 6.1.

6.2.2 Tumor dose as a function of tumor-to-blood ratio.

Throughout, r will denote a value of the tumor-to-blood ^{10}B concentration ratio. For a fixed value of r, the absorbed dose in a point inside a tumor can be computed from a 3D

derived dosimetry as:

$$D_{tumor}(x,y,z) = D_{b-ind}(x,y,z) + r\, C_{blood}\; D_{b-dep}(x,y,z), \tag{6.1}$$

where D_{b-ind} and D_{b-dep} are the boron-independent and boron-dependent (normalized to 1 ppm) biologically weighted dose, respectively, and C_{blood} is the average value of blood boron concentration during the irradiation time. Equation (6.1) shows that the tumor dose dependence on the boron concentration ratio r is linear.

In section 5.4.1, the procedure followed to determined the 39 tumor doses for $r = 3.5$ was presented. These doses are listed in Table 5.2. Applying the same procedure as before, a new set of 39 tumor doses was determined for the case $r = 2.5$. Then, from Eq. (6.1) and the two sets of 39 tumor doses, the linear equation of every nodule dose as a function of r was computed.

6.2.3 Tumor control probability model

In 1985, Overgaard *et al.* [80] presented a detailed analysis of conventional radiotherapy in 204 lesions of malignant melanoma in 114 patients with regard to radiobiological parameters such as total dose, dose per fraction[1], treatment time, tumor volume and fractionation models. In this work, they have shown that neither total dose, treatment time nor various modifications of the nominal standard dose concept [28] have any well-defined correlation with response. However, they have found a significant relationship between dose per fraction and response so that high doses per fraction yielded a significantly better response. The lack of treatment time influence allowed them to analyze their data according to the linear-quadratic model[2] yielding an α/β ratio of 2.5 Gy. Using this ratio, a volume corrected iso-effect formula for malignant melanomas was presented

[1]Dose per fraction: In a multifraction treatment, the dose is divided into a number of fractions in order to spare normal tissues (due to repair and repopulation effects), and to increase damage to the tumor (due to reoxygenation and reassortment effects). For details see Ref. [42].

[2]Linear-quadratic model: the cell survival curve is given by $S = e^{-\alpha D - \beta D^2}$, where S is the fraction of cells surviving a dose D, and α and β are constants. The α/β ratio is the dose at which cell killing by the linear (α) and quadratic (β) contributions are equal.

ETD (Gy)	Response (%)		
	None	Partial	Complete
≤ 50	78	19	3
51-70	41	33	26
71-90	13	46	41
91-110	16	26	58
111-130	4	16	80
131-150	8	0	92
> 150	0	7	93

Table 6.2: Relationship between extrapolated total dose and tumor response [80].

(Eq. [6.2]). They introduced the concept of extrapolated total dose (ETD), a quantity by which different fractionation regimens can be intercompared. The ETD comprises the effect of tumor size, total dose, and dose per fraction on tumor response. In other words, two fractionated regimens that have the same ETD are supposed to lead to the same level of injury or control. It can be calculated as:

$$ETD = D_{tumor}\frac{d+\alpha/\beta}{\alpha/\beta}\left(\frac{M}{1\,\mathrm{cm}}\right)^{-0.33}, \tag{6.2}$$

where D_{tumor} and d are the tumor total dose and dose per fraction (in Gy), respectively, M is the mean tumor diameter (in cm), and α/β is 2.5 Gy for melanomas.

In addition to the ETD concept, they also reported experimental data relating the extrapolated total dose and tumor response. This latter was recorded as either none, partial (i.e., $\geq 50\%$ reduction of tumor volume), or complete response (i.e., total disappearance of tumor). The observation time was between 2 and 180 months, with the short observation occurring mainly in patients who had disseminated disease and were treated with palliative intention. Table 6.2 summarizes their results.

Based on the concept of ETD and the reported experimental data of achieving *complete response*, an expression for the tumor control probability (TCP) as a function of the tumor-to-blood ratio (r) was derived in the present work as follows. In cases of single irradiation as the ones considered in the current analysis, D_{tumor} equals d in equation

(6.2). Since the ETD is a function of D_{tumor} and, as Eq. (6.1) shows, D_{tumor} is a function of the tumor-to-blood ratio r, the ETD can be expressed as a function of r. In order to determine an explicit function for the tumor control probabilityin terms of the ETD, a two-parameter model based on a logit function was proposed. From data of achieving complete response in Table 6.2, Fukuda *et al.* [33] presented a dose response curve, giving a 50% cure probability at the ETD level of 83 Gy and 90% at 180 Gy. Thus, the expression for the TCP as a function of the extrapolated total dose is obtained finding the parameters that satisfy these dose-response relationships. Expression (6.3) shows the tumor control probability as a function of the ETD with its resulting parameters.

$$TCP(r) = \frac{1}{1 + \left(\frac{83}{ETD(r)}\right)^{2.83}}. \tag{6.3}$$

Note that for each nodule i ($i = 1, ..., 39$), there is a different function TCP_i, since parameters D_{tumor} and M in equation (6.2) differ from one nodule to another. Figure 6.1 shows the TCP function for nodules 2, 4 and 19. Nodule 2 absorbed the same dose as nodule 4, but is about three times as large (see Table 5.2). On the other hand, while nodules 4 and 19 have similar sizes, the latter received a higher dose. This explains the differences between the TCP functions for these three nodules.

6.2.4 Maximum likelihood estimate method

In order to determine the tumor-to-blood ^{10}B concentration ratio r from the clinical outcome of the first BNCT treatment, a maximum likelihood estimate method (mle) for the set of random variables X_i ($i = 1, ..., 39$) is applied. The variables X_i are defined as:

$$X_i = \begin{cases} 1 & \text{if nodule } i \text{ shows complete response} \\ 0 & \text{otherwise} \end{cases}.$$

One feature of this problem is that the random variables X_i are not identically distributed, since for the same concentration ratio r, the probability of success is different for

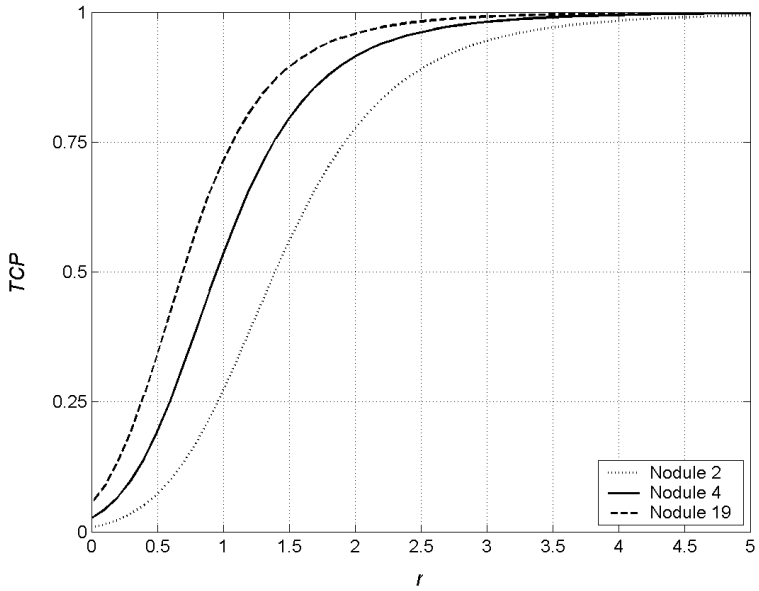

Figure 6.1: Tumor control probability as a function of r for nodules 2, 4 and 19. See Fig. 5.8.

each nodule (Fig. 6.1). For a given r, the nodule i has a probability $TCP_i(r)$ of complete response (i.e. probability of success). Therefore, each X_i is a Bernoulli random variable with probabilities $P(X_i = 1|r) = TCP_i(r)$ and $P(X_i = 0|r) = 1 - TCP_i(r)$.

Let x_i denote the (actual, not random) clinical response of nodule i (see Table 6.1). Independence between responses in different nodules is assumed. Therefore, the *a priori* probability of obtaining the set of results $(x_1, ..., x_{39})$ is a function of r, i.e. the likelihood function $L(r)$, and can be computed as:

$$\begin{aligned} L(r) &= P(X_1 = x_1, ..., X_{39} = x_{39}|r) \\ &= \prod_{i=1}^{39} P(X_i = x_i|r) \\ &= \prod_{i=1}^{39} (TCP_i(r))^{x_i} (1 - TCP_i(r))^{(1-x_i)} . \end{aligned} \tag{6.4}$$

Thus, expression (6.4) represents the joint probability that each random variable X_i takes the observed value x_i for a given r.

The *maximum likelihood estimate* $\hat{r}$ for the tumor-to-blood ^{10}B concentration ratio is

then the value that maximizes L. In other words, $\hat{r}$ is the ratio that makes the clinical outcome most probable or likely.

To find a confidence interval for the ratio, the sampling distribution of $\hat{r}$ is estimated by means of a parametric bootstrap method, proceeding as follows.

A large number of repetitions of the clinical case is randomly simulated. In each repetition, the response of nodule i ($i = 1, ..., 39$) is sampled using the tumor control probability $TCP_i(\hat{r})$ (that is, the TCP obtained with the estimated tumor-to-blood ^{10}B ratio $\hat{r}$). Thus, X_i is assigned the value 1 with probability $TCP_i(\hat{r})$ and 0 with probability $1 - TCP_i(\hat{r})$. For every set of 39 simulated responses, the maximum likelihood estimate is computed just as it was done with the actual responses. This large set of maximum likelihood estimates gives an estimation of the sampling distribution of $\hat{r}$ which allows to find its confidence intervals.

Finally, the expected number of nodules with positive response is computed for the estimate $\hat{r}$ and is compared with the actual number of positive responses (Table 6.1). Results are presented in section 6.3.

6.2.5 Experimental measurements of tumor-to-blood ratios.

As part of the pharmacokinectic studies of boronophenylalanine-fructose in melanoma patients carried out in Argentina [64], a biodistribution test was performed to the patient considered for the present analysis prior to the BNCT treatment .

BPA preparation and infusion

L-p-boronophenylalanine 99% isotopically enriched in ^{10}B was obtained from Boron Biologicals (BB), its successor Ryscor Science (RS) (Raleigh, NC) and Glyconix (New York, NY). The BB and RS products were recrystallized to avoid contamination or decomposition during a few years of storage. Chemical purity of the resulting products was verified by high performance liquid chromatography (HPLC). A fresh solution of BPA-F was pre-

pared for the patient according to the recommended procedure [18]. Pyrogen/sterility tests were also carried out on incoming reagents and the final solution. The infusion was used within 48 h of preparation.

The patient received a BPA administration of 300 mg kg^{-1} infused over 90 min via a perfusion pump. Following the protocol, blood samples for boron analysis were collected every 10 or 15 min for about 300 min.

Tissue sampling

Punch biopsies of normal skin and tumor were performed between 160 and 190 min after the end of BPA administration. In order to obtain information about the possible inhomogeneity of boron uptake between nodules, tumor tissue samples were extracted from three different nodules.

Boron analysis

Boron measurements were performed by inductively coupled plasma optical emission spectroscopy (ICP-OES) employing an axially viewed plasma. Blood samples were prepared by dilution of about 0.3 g of blood to 5 ml with water containing Triton X-100 (0.1% v/v) and appropriate concentrations of strontium (Sr) and yttrium (Y) to be employed as internal standards. Tissue masses between 7 and 30 mg were digested for 2 h at 60°C with a mixture of concentrated nitric and sulfuric acids, and the digest diluted to 1.0 ml with a Triton X-100 solution containing also Sr and Y. Analyte emission intensity was measured at 249.677 nm boron line. Matrix matched boron standards of concentrations between 0.1 and 10.0 mg ml^{-1} were employed for calibration.

To predict ^{10}B concentration in blood the pharmacokinetic two-compartment open model [55] was applied to fit the experimental biodistribution data.

Punch biopsies were carried out during a period of 30 min. Since the boron concentration in blood decreased very slowly during tissue sampling, a mean value of 15 ± 1

Sample ID	r
1	1.8 ± 0.4
2	2.6 ± 0.5
3	2.4 ± 0.5
Mean $\pm$ SD	2.2 ± 0.3

Table 6.3: Experimental measurements of tumor-to-blood ^{10}B concentration ratios (r) for patient #1.

ppm of boron was used to compute the ratios. Table 6.3 summarizes tumor-to-blood ratios obtained for the 3 different nodules. Note that Mean $\pm$ SD refers to the weighted unbiased estimator for the unknown mean along with its standard deviation.

6.3 Clinical application results

The results of the tumor-to-blood ^{10}B ratio estimation based on the clinical outcome of a nodular melanoma patient are now presented.

Figure 6.2 shows the behavior of the likelihood function (described in Eq. [6.4]). The maximum likelihood estimate for the tumor-to-blood ^{10}B concentration ratio is $\hat{r} = 2.1$, value at which $L(r)$ attains its maximum.

Confidence intervals for $\hat{r}$ are obtained from the sampling distribution calculated with the parametric bootstrap method. Figure 6.3 depicts this estimated distribution. Two confidence intervals are evaluated from the sampling distribution: a 95% confidence interval and a one standard deviation interval. The obtained results are as follow.

$$\begin{aligned} r &\in [1.6,\ 3.0] \ \text{(95\% interval)} \\ r &= 2.1 \pm 0.3 \ \text{(1SD interval)} \end{aligned}$$

The expected number of positive responses for $\hat{r}$ is 23.5, which is in close agreement with the observed number of positive responses in this clinical case, i.e. 23 (see Table 6.1).

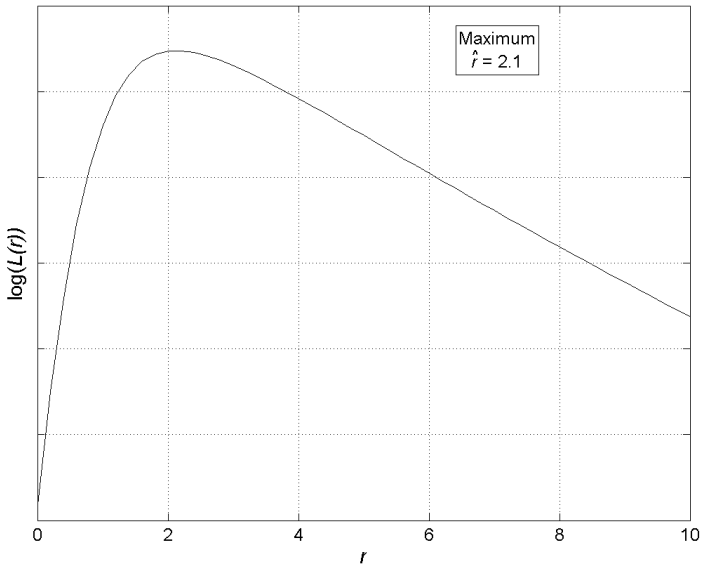

Figure 6.2: Likelihood function $L(r)$ computed for the clinical outcome of a nodular melanoma patient. $L(r)$ attains its maximum at $\hat{r} = 2.1$.

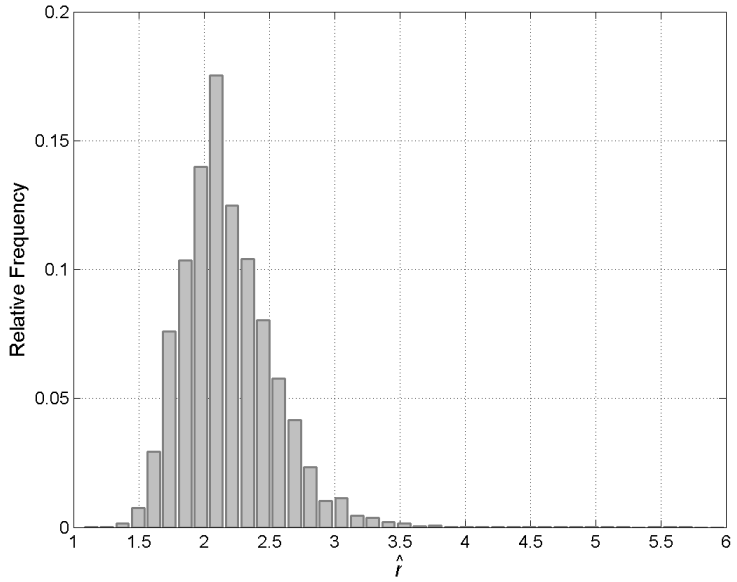

Figure 6.3: Sampling distribution of the maximum likelihood estimate $\hat{r}$. The 95% confidence interval is [1.6, 3.0]. The standard deviation is 0.3.

6.4 General discussions

Comparison of the estimate with experimental data

In section 6.3, the maximum likelihood estimate of the tumor-to-blood ^{10}B concentration ratio along with confidence intervals were presented. Considering one SD confidence interval, the statistical-based ratio is 2.1 ± 0.3.

To compare the estimate with the experimental values, some considerations must be taken into account. First note that the sampling distribution from which confidence intervals were derived does not represent the variability of r between nodules or patients. Instead, it shows the variability of the mle due to the randomness of the process. Thus, the standard deviation of $\hat{r}$ represents the uncertainty on the estimate. Second, the statistical-based ratio is based on the clinical outcome of a *single* patient. Then, the estimate may be expected to be close to the experimentally-derived ratio from tumor punch biopsies performed in the same patient under consideration. It should not necessarily coincide with the mean of a set of experimental measurements performed in different patients nor the 3.5 value generally assumed in BNCT..

Table 6.3 shows the experimental ratios obtained for the analyzed patient. A ratio of 2.2 ± 0.3 (Mean $\pm$ SD) was found for this case, which shows an excellent agreement with the statistical-based result.

In addition, different groups have studied the biodistribution of BPA-F in melanoma patients. Mallesch *et al.* [69] reported on the distribution and pharmacokinetics of BPA in twelve patients including cases of cutaneous metastatic melanoma, metastatic melanoma to the lymph nodes and cases of cerebral metastasis. They showed that for all melanoma, whether melanotic or amelanotic, the BPA uptake was significantly higher than the blood, with an average tumor-to-blood boron concentration ratio and standard deviation of about 4.4 ± 3.2. In addition, boron concentration kinetics of BPA was analyzed in twenty two melanoma patients with primary or metastatic melanomas by Fukuda *et al.* [31]. Among the 22 patients, four of them had metastatic melanoma after surgical treatment of primary

lesions. The other 18 primary melanomas consisted of different histological types: nodular melanomas, acral lentiginous maligna melanomas, lentigo maligna melanomas, superficial spreading melanoma and ocular-type melanomas. This group found that tumor-to-blood ratios were roughly consistent at around values of 2-4, irrespective of the time after injection, BPA dose, and route of administration. They reported a mean value (±1SD) of 3.4 ± 0.8, and a relatively constant behavior during 6 hours after the end of BPA administration. As part of the Phase I trial with melanoma patients carried out by Harvard/MIT, Busse *et al.* [11] reported tumor-to-blood ratios for three patients with cutaneous melanoma. They found an average tumor-to-blood ratio (±1SD) of 3.3 ± 0.8. Finally, CNEA analyzed tumor-to-blood ratios in five patients all with nodular melanoma [54, 64, 87]. The obtained result in this case (excluding the data of the patient considered for the mle analysis) was 2.4 ± 0.7 (Mean ± SD).

Under the previous considerations, the statistical-based ratio is consistent with the data published by the different groups. The estimate is smaller than the mean ratios of the experimentally-derived samples, except for the sample mean obtained by CNEA. The fact that the statistical-based ratio involved only a nodular melanoma (NM) makes its smaller value expectable. There is some evidence that the tumor control rate in NM is apparently worse than in non-NM [46]. The most likely explanation presented by Hiratsuka *et al.* [46] was that the uptake of boron in NM would be lesser than that in other types of melanoma. CNEA findings of tumor-to-blood ratios in nodular melanoma patients would be consistent with Hiratsuka's hypothesis.

Tumor-to-blood ratio estimate interpretation

The present analysis is based on a number of assumptions, the most important being independence between nodules' responses, uniform boron concentration throughout each tumor volume and also between different tumors (single ratio), and a constant or static tumor-to-blood ratio during irradiation time. Although some of them may not necessarily

reflect reality, such as the case of boron uniformity between nodules, these assumptions are currently used in BNCT. In this context, the estimated value of r should be interpreted as a kind of *effective* ratio in the following sense: although it might be different from all 39 actual ratios, it is the ratio that assigned each nodule a TCP as compatible as possible with the actual response.

On the other hand, tumor biopsies are not necessarily performed to treated patients. Then, the statistical-based ratio may be useful, for example, to perform a retrospective analysis of the specific treatment from which it was derived. This would allow to have better estimates of the doses that were delivered to nodules than the *a priori* values inferred from a treatment planning based on an initial guess of the ratio.

Performance of the method

The sensitivity of the proposed method to variations on the steps concerned in the calculations was studied. At significant changes in the TCP fitting parameters, the differences in the estimation were negligible. Moreover, only minor changes were detected when nodules doses are perturbed up to 20%. The deviation due to these perturbations is lower than the standard deviation of the estimated ratio.

6.5 Concluding remarks

The maximum likelihood estimate method here presented to determining the tumor-to-blood ^{10}B concentration ratio does not involve surgery or tumor punch biopsy. This makes the approach particularly attractive because it is minimally invasive for patients compared to the experimental method. The mle can be performed after any BNCT treatment provided the number of nodules is large enough. For each treated patient one effective ratio can be predicted and used for retrospective analysis purposes.

In addition to be able to perform a retrospective analysis for each treated patient,

it would be also desirable to have, at the stage of treatment planning, a ratio that best predicts the clinical outcome of a new patient. A distribution of effective ratios can be obtained from applying the mle method to a good number of patients. If a single value of the tumor-to-blood ratio is considered appropriate to compute doses and $TCPs$, then the mean of the effective ratio sample could be selected for the next patient. The validity of the assumption on a single ratio, however, is deeply analyzed in the next chapter.

Chapter 7

Effects of tumor-to-blood ratio variability and dose inhomogeneity

7.1 Introduction

As in other forms of radiotherapy, the eventual success of the Boron Neutron Capture Therapy is associated with the ability of delivering high doses to the tumors while sparing surrounding normal tissues. To achieve this goal, BNCT takes advantage of the high LET products of the $^{10}\mathrm{B}(\mathrm{n},\alpha)^{7}\mathrm{Li}$ reaction, and the preferential boron uptake by tumor cells [2, 20]. A large fraction of the dose in BNCT is due to the interaction of the radiation field with the boron compound. Then, it is essential to have reliable estimates of the boron concentration either in normal and tumor tissues.

As mentioned in Chapter 6, *in vivo* quantification of the boron concentration in tissues during the treatment is very difficult. Although a promising technique is being evaluated in glioblastoma patients [91], it is of limited use in the routine clinical applications at present. Some approximations are then introduced for the dose calculations, essentially by means of parameters that have been historically determined by experimental measurements. This is the case of the tumor boron concentration, which is computed from the

boron in blood and its level is described as a static ratio between both concentrations.

It is usual to consider a single value of the tumor-to-blood ratio in order to compute absorbed doses and tumor control probabilities ($TCPs$) in BNCT treatments. The single value that is used in these cases is generally the arithmetic mean of some set of experimental measurements, such as those referenced in section 6.5. Since the dose depends linearly on the ratio r, the computation of the expected absorbed dose as the dose corresponding to that single value of r is adequate. However, a description of the distribution of ratios (due to measurements uncertainties and to biological diversity) is necessary to obtain confidence intervals for the dose, and also to describe the probability distribution of possible doses. Moreover, as observed by Culbertson *et al.* [22], the dependence of the TCP on the dose is highly nonlinear, which makes the computation of these probabilities from a single value of the ratio very questionable.

In addition to the tumor-to-blood ratio variability, the dose inhomogeneity over the target volume may also affect the tumor control probability. For a typical BNCT treatment, the maximum and minimum values of the tumor dose distribution differ significantly (typically, more than 20%), particularly in large tumors [59]. In these cases, the average dose is generally used as a representative value and the TCP is computed as if the dose in the tumor were uniformly equal to the average. This can lead to very inaccurate results, as will be shown in this chapter.

In this chapter, a comprehensive framework for incorporating the variability of the tumor-to-blood ratios into the calculation of absorbed doses and TCP in BNCT treatments is described. Furthermore, a tumor control probability model is presented that considers the effect of the ratio variability as well as the possible dose inhomogeneity throughout the tumor volume. Specifically, the introduced concepts are applied to cases of malignant melanomas, and are illustrated in the first BNCT treatments of skin melanoma carried out in Argentina.

7.2 Probabilistic distribution of tumor-to-blood ratios

It has been shown in section 6.2.2, that the absorbed dose in a point inside a tumor depends linearly on the boron concentration ratio r, and it can be computed as

$$D_{tumor} = D_{b-ind} + r D_{b-dep} C_{blood}, \tag{7.1}$$

where D_{b-ind} and D_{b-dep} are the boron-independent and boron-dependent (normalized to 1 ppm) biologically weighted dose, respectively, and C_{blood} is the average value of blood boron concentration during the irradiation time. Considering that the tumor-to-blood ratio is a random variable R with mean $E(R) = \bar{r}$, the tumor dose turns out to be also a random variable, and its expected value is

$$E(D_{tumor}) = D_{b-ind} + \bar{r} D_{b-dep} C_{blood}. \tag{7.2}$$

To obtain confidence intervals for D_{tumor}, a good description of the distribution of ratios is necessary. Table 7.1 shows a collection of experimentally-determined tumor-to-blood ^{10}B ratios obtained in melanoma patients by different groups [11, 29, 54, 64, 69, 87]. This data set corresponds to BPA delivery agent and comprises various melanoma types in different locations, and a diversity of infusion protocols and drug doses. The mean value considering the whole set of data is $\bar{r} = 3.58$. This collection derives an empirical distribution of r that can be used for the purpose of computing confidence intervals in melanoma treatments. However, it would be more useful to find a known distribution describing the behavior of r, since it will make it easier to compute any statistical element of the distribution. Moreover, it will enable to describe the probability density of the random variable D_{tumor}.

7.2.1 Lognormal behavior of the ratio and dose distributions

It is clear from the data in Table 7.1, and also for the case of glioblastoma patients [18], that the ratio between tumor and blood ^{10}B concentration would be better described as a

Tumor-to-blood ^{10}B concentration ratios			
Mallesch *et al.* (1994) [69]	Busse *et al.*[a] (1997) [11]	Fukuda *et al.*[b] (1999) [31]	CNEA (2002-2004) [54, 64, 87]
0.5	2.4	1.3	1.4
1.0	3.6	2.4	1.8
1.1	4.0	2.8	1.8
1.6		3.2	1.9
2.0		3.3	2.0
2.0		3.3	2.4
2.1		3.4	2.4
2.3		3.7	2.4
2.3		3.8	2.5
2.4		3.9	2.6
2.4		3.9	2.8
3.1		4.0	2.8
3.3		4.3	4.1
4.1		4.4	
4.4			
4.8			
4.9			
5.1			
5.8			
5.9			
6.3			
6.3			
6.8			
9.1			
15.7			

[a] Ratios computed from published tumor and blood ^{10}B concentrations.

[b] Data extracted from the graph.

Table 7.1: Experimental measurements of the tumor-to-blood ^{10}B concentration ratios for melanoma patients published by different groups.

distribution function instead of a single value. What is not evident from the data, however, is which type of distribution describes the behavior of the ratios best. There are some arguments with empirical basis that may help guide the choice of a specific distribution. For example, the selected distribution should only have density for positive real values of r. In addition, experimental data in Table 7.1 shows a right-biased distribution. This would restrict the search to groups such as those of gamma or lognormal probability density functions.

In the case of melanoma patients, the lognormal distribution is the probability function that happens to describe the variability of the ratios best (Table 7.1). The goodness of fit to select between candidate groups was assessed with the Lilliefors test [84].

The experimental data is then fitted to a lognormal distribution. Therefore, the probability density of the ratios is given by

$$f_R(r) = \frac{1}{r\sigma\sqrt{2\pi}} e^{-\frac{(\ln(r)-\mu)^2}{2\sigma^2}}, \tag{7.3}$$

where μ and σ are the fitting parameters of the lognormal distribution. This distribution together with equation (7.1) allows to find an expression for the probability density of the absorbed dose at any point (see Appendix D). In can be expressed as

$$f_D(d) = \frac{1}{(d - D_{b-ind})\,\sigma\sqrt{2\pi}} e^{-\frac{\left(\ln\left(\frac{d-D_{b-ind}}{D_{b-dep}\ C_{blood}}\right)-\mu\right)^2}{2\sigma^2}}. \tag{7.4}$$

Expression (7.4) completely describes the behavior of the dose. However, it is easier to compute confidence intervals directly from those of the tumor-to-blood ratio. Since ratios follow a lognormal distribution, confidence intervals can be computed with any statistical software. From the increasing relation between dose and ratio shown in equation (7.1), it follows that the limits of a confidence interval for the dose is the result of applying equation (7.1) to the limits of the confidence interval for the ratio. Note that the lognormal distribution is asymmetric and this asymmetry is inherited by the dose probability distribution. Therefore, it may be questionable to express dose results as MEAN±SD. A 68% confidence interval would be more appropriate.

7.2.2 Tumor control probability

Tumors with homogeneous dose

A tumor control probability model, such as the one introduced in section 6.2.3, gives the probability of controlling a tumor for a fixed homogeneous absorbed dose. If the dose is homogeneously distributed over the tumor volume, the tumor control probability can be considered a function of the average absorbed dose. This applies for example to tumors sufficiently small that the absorbed dose can be assumed constant (and equal, therefore, to the average dose).

Equation (7.1) shows that the dose is a function of the ratio r. Consequently, the tumor control probability is a function of r, too. As pointed out above, a single value of r is commonly used to compute tumor control probabilities (for example, the mean value $\bar{r} = 3.58$ of the empirical distribution from table 7.1). To take into account the variability of the ratios, the tumor control probability as a function of r, $TCP(r)$, must be considered a conditional density: $TCP(r) = TCP|_{R=r}$. Therefore, the tumor control probability should be calculated as:

$$\begin{aligned} TCP &= \int_0^{+\infty} TCP|_{R=r} f_R(r) dr \\ &= \int_0^{+\infty} TCP|_{R=r} \frac{1}{r\sigma\sqrt{2\pi}} e^{-\frac{(\ln(r)-\mu)^2}{2\sigma^2}} dr. \end{aligned} \tag{7.5}$$

Note that this expression is valid for any TCP model under consideration (i.e., for any form of $TCP|_{R=r}$).

Tumors with inhomogeneous dose

In conventional radiotherapy, efforts are made to deliver an almost uniform dose to tumors. Since under this condition the average absorbed dose is a representative dose of the target volume, most TCP models do not need to deal with large dose inhomogeneities. In BNCT, the dose distribution varies significantly with depth, and then, the dose uniformity condition is virtually impossible to achieve, particularly in large tumor volumes.

Therefore, the known TCP models in standard radiotherapy must be adapted to handle this inhomogeneity.

Usually, TCP models consist on a formula to calculate the tumor control probability as a function of the tumor volume (v) and the absorbed dose (D). A general form for $TCPs$ is

$$TCP = g(v^c h(D)), \tag{7.6}$$

where c is a parameter of the model, and g and h are strictly monotone functions. Very different TCP models, such as those based on Poisson statistics [4] and the empirical model presented by Overgaard *el al.* [80], can be written in this form. Recall that the TCP described with Poisson statistics has the usual expression

$$TCP = e^{-c_1 v^{c_2} S}, \tag{7.7}$$

where S is the clonogen surviving fraction (which is a function of D), and c_1, c_2 parameters of the model. Overgaard's model has the form (see Eqs. [6.2] and [6.3])

$$TCP = \frac{1}{1 + \left(\frac{83}{\left(\frac{\pi}{6}\right)^{1/9} D \frac{D+\alpha/\beta}{\alpha/\beta} v^{-1/9}} \right)^{2.83}}. \tag{7.8}$$

If the absorbed dose is not homogeneous throughout the tumor volume, a first try is to compute the TCP substituting the average dose in equation (7.6). This leads to wrong results (generally, to an overestimation of the TCP, as will be shown below). Another approach to the inhomogeneous case is to split the tumor volume into smaller subvolumes so that the dose can be considered constant in each subvolume. Then, equation (7.6) is used to compute the control probability of each subvolume. In this step, one is assuming that the control probability of each subvolume is the same if the subvolume is isolated or if it is part of a greater tumor volume. If, additionally, one assumes that responses of different subvolumes are independent, the TCP is simply the product of the control probabilities of the subvolumes. However, these assumptions are not always accepted and

are not compatible with most TCP models [4]. To see this, following Bentzen *et al.* [4], split a tumor with constant dose D in two subvolumes with volume v_1 and v_2. Under the mentioned assumptions, one should have

$$g\left((v_1+v_2)^c h(D)\right) = g(v_1^c h(D)) g(v_2^c h(D)). \tag{7.9}$$

For example, Overgaard's model does not satisfy equation (7.9). Moreover, Bentzen *et al.* [4] observed that for the Poisson model, the validity of equation (7.9) is equivalent to parameter c_2 in equation (7.7) being equal to 1. They also present evidence showing that $c_2 = 1$ does not reflect the behavior of clinical results, which means that clinical responses do not satisfy the independence assumption.

A general approach to compute $TCPs$ in the inhomogeneous case is now presented. Take a tumor T with volume v and average absorbed dose $\bar{D}$. Split the tumor T in n subvolumes $T_1, \ldots, T_n$ of equal size $\frac{v}{n}$, so that absorbed dose is almost constant in each T_i. Denote by D_i the dose in the subvolume T_i and let $\tilde{v}_i$ be defined by the relation

$$g(\tilde{v}_i^c h(\bar{D})) = g\left(\left(\frac{v}{n}\right)^c h(D_i)\right). \tag{7.10}$$

In other words, an isolated tumor volume $\tilde{v}_i$ with absorbed dose $\bar{D}$ would have the same TCP as an isolated tumor volume $\frac{v}{n}$ with absorbed dose D_i. Since g is strictly monotone (and consequently injective), it follows that $\tilde{v}_i$ can be computed as

$$\tilde{v}_i = \frac{v}{n}\left(\frac{h(D_i)}{h(\bar{D})}\right)^{1/c}.$$

Now, each T_i isolated with an absorbed dose D_i responds in terms of TCP in the same way as a tumor $\tilde{T}_i$ with size $\tilde{v}_i$ and dose $\bar{D}$. Consider the subvolume T_1. As mentioned above, the TCP of T_1 isolated can differ from the probability of controlling T_1 as a part of the tumor volume T, due to possible interaction between subvolumes and dependence between subvolume responses. However, since T_1 with dose D_1 is equivalent, in terms of TCP, to $\tilde{T}_1$ with dose $\bar{D}$, if T_1 is replaced by $\tilde{T}_1$ in tumor T, the probability of controlling the

whole tumor should not be expected to change (i.e., the interaction and interdependence of $\tilde{T}_1$ with the rest of the tumor can be assumed to be the same as those of T_1). Repeating this with T_i, $i = 2, \ldots, n$, it follows that the original tumor T, which is the union $\cup_{i=1}^{n} T_i$, will respond in the same way as the union $\cup_{i=1}^{n} \tilde{T}_i$. To compute the control probability of $\tilde{T} := \cup_{i=1}^{n} \tilde{T}_i$, note that the dose in $\tilde{T}$ is uniform and equal to $\bar{D}$, and that the size of $\tilde{T}$ is $\tilde{v} = \sum_{i=1}^{n} \tilde{v}_i$. Therefore, this probability is given by $g(\tilde{v}^c h(\bar{D}))$. By the previous considerations, the TCP of the original tumor T is also $g(\tilde{v}^c h(\bar{D}))$.

The volume $\tilde{v}$ involved in the TCP calculation can be computed in a more accurate and simple way. Since

$$\tilde{v} = \sum_{i=1}^{n} \tilde{v}_i = \frac{v}{n} \sum_{i=1}^{n} \left(\frac{h(D_i)}{h(\bar{D})} \right)^{1/c},$$

by letting $n \to \infty$, $\tilde{v}$ can be expressed as

$$\tilde{v} = \int_T \left(\frac{h(D(\mathbf{x}))}{h(\bar{D})} \right)^{1/c} d\mathbf{x} = \frac{1}{h(\bar{D})^{1/c}} \int_T h(D(\mathbf{x}))^{1/c} d\mathbf{x}, \tag{7.11}$$

where $D(\mathbf{x})$ is the spatial dose distribution. Therefore, the expression for the TCP is

$$\begin{aligned} TCP &= g(\tilde{v}^c h(\bar{D})) \qquad (7.12) \\ &= g\left(\left[\int_T \left(\frac{h(D(\mathbf{x}))}{h(\bar{D})} \right)^{1/c} d\mathbf{x} \right]^c h(\bar{D}) \right) \\ &= g\left(\frac{1}{h(\bar{D})} \left[\int_T h(D(\mathbf{x}))^{1/c} d\mathbf{x} \right]^c h(\bar{D}) \right) \\ &= g\left(\left[\int_T h(D(\mathbf{x}))^{1/c} d\mathbf{x} \right]^c \right). \qquad (7.13) \end{aligned}$$

The only assumption of this model, the fact that replacing a subvolume by an equivalent (in terms of TCP) subvolume does not affect the overall TCP, is much weaker than the assumptions needed for equation (7.9). In fact, it is implied by the independence assumption. To see this, take tumor T with volume v, and subvolumes $T_1, \ldots, T_n$ of size $v_1, \ldots, v_n$ and constant doses $D_1, \ldots, D_n$. Let $TCP(v_1, \ldots, v_n; D_1, \ldots, D_n)$ denote the

probability that tumor T is controlled. Under the independence assumption

$$TCP(v_1, \dots, v_n; D_1, \dots, D_n) = TCP(v_1; D_1) \dots TCP(v_n; D_n).$$

Applying equation (7.10), each term of the product can be replaced to obtain

$$\begin{aligned} TCP(v_1, \dots, v_n; D_1, \dots, D_n) &= TCP(\tilde{v}_1, \bar{D}) \dots TCP(\tilde{v}_n, \bar{D}) \\ &= TCP(\tilde{v}_1, \dots, \tilde{v}_n; \bar{D}, \dots, \bar{D}) \\ &= TCP(\tilde{v}, \bar{D}), \end{aligned}$$

which shows the desired result. On the other hand, the proposed model is compatible with any TCP function of the form 7.6.

It should be also noted that this model satisfies some desirable properties:

- *For a uniform dose, the TCP given by equation* (7.12) *coincides with that of equation* (7.6). If in equation (7.11) D is set to be uniform, then $D(\mathbf{x}) = \bar{D}\ \forall \mathbf{x} \in T$. Thus,

  $$\tilde{v} = \int_T 1 \, d\mathbf{x} = v.$$

  Substituting v into Eq. (7.12) and denoting D as the constant dose in the tumor volume, one obtains the TCP given by Eq. (7.6).

- *For any spatial dose distribution, the TCP given by Eq.* (7.12) *does not depend on the dose to which volumes are normalized.* Suppose that in equation (7.10), $\tilde{v}$ is defined in terms of, say, the minimum dose in the tumor instead of the average dose. As shown in the derivation of equation (7.13), the term that would depend on the minimum dose would be simplified. Thus, the obtained TCP would be the same as in Eq. (7.13).

- *If the dose is not uniform over the tumor volume, equation* (7.6) *applied to the average dose overestimates the TCP.* Indeed, the different TCP models of the form

(7.6) can be represented, after some manipulation, with an increasing function g, a negative value of c, and an increasing and convex function h. Some calculus shows that in this case, $h(D)^{1/c}$ is also a convex function. Therefore, the average value of $h(D)^{1/c}$ on T will be greater than the value that the function $h(\cdot)^{1/c}$ takes at the average value of D, that is:

$$\frac{1}{v}\int_T h(D(\mathbf{x}))^{1/c}d\mathbf{x} \geq h(\bar{D})^{1/c}$$

which is Jensen's inequality. As a consequence,

$$\tilde{v} = \frac{1}{h(\bar{D})^{1/c}}\int_T h(D(\mathbf{x}))^{1/c}d\mathbf{x} \geq v,$$

with strict inequality unless the dose is constant. This means that the TCP obtained for a volume v and a dose $\bar{D}$ will be greater than the TCP for a volume $\tilde{v}$ and a dose $\bar{D}$, which shows the overestimation of the TCP when average dose is used without changing the volume in equation (7.6).

This last result can be reformulated to obtain the following statement, which also shows the consistency of the model: *among all spatial dose distribution with the same average dose, the constant one gives the highest TCP.*

Finally, the ratio variability and dose inhomogeneity are combined as follows. For each fixed value of r, the average dose $\bar{D} = \bar{D}(r)$ and the value of the dose at each point $D = D(\mathbf{x}, r)$ can be obtained. Therefore, equation (7.12) can be used to obtain the conditional tumor control probability $TCP(r) = TCP|_{R=r}$. Now, the tumor control probability is computed as in equation (7.5):

$$TCP = \int_0^{+\infty} g\left(\left[\int_T h(D(\mathbf{x}, r))^{1/c}d\mathbf{x}\right]^c\right) f_R(r)dr. \tag{7.14}$$

7.3 Application to clinical melanoma cases

7.3.1 A clinical case with homogeneous dose distributions over tumors

In this section, the previous concepts are applied to the first cutaneous melanoma patient treated with the RA-6 hyperthermal beam at Centro Atómico Bariloche [35].

As described in detail in section 5.4.1, delineation of tumors on CT images for patient #1 was not feasible due to their very small size (see Table 5.2). Then, tumor doses were assumed uniform over each tumor volume. This description should be considered as a good approximation to the real case, since the dose inhomogeneity in a volume of 2 mm mean diameter is likely to be much lower than 5%, which is the standard goal in conventional radiotherapy. As a consequence, this example will make apparent the effect of ratio variability in dose and TCP computations.

First, the tumor dose corresponding to both the single ratio and variable ratio models is computed. For the single ratio, the mean of the experimental data in Table 7.1 ($\bar{r} = 3.58$,) is used. In the variable ratio model, the expected values of the dose, together with their confidence intervals, are computed from the lognormal distribution of ratios described in 7.2.1. Recall that the dose corresponding to $\bar{r} = 3.58$ coincides with the expected value of the dose distribution.

Tumor control probabilities are computed for the two models. The TCP model for melanomas presented in section 6.2.3 (and rewritten in Eq. [7.8]) is considered in both cases, with $\alpha/\beta = 2.5$ Gy. For the single value model, the TCP of each nodule is obtained from equation (7.8) replacing D by the dose computed for $\bar{r} = 3.58$. In the lognormal model, expression (7.8) gives the conditional density $TCP|_{R=r}$, and the tumor control probability is computed as shown in Eq. (7.5). The final expression for the TCP is

$$TCP = \int_0^{+\infty} \frac{1}{1 + \left(\frac{83}{ETD(r)}\right)^{2.83}} \frac{1}{r\sigma\sqrt{2\pi}} e^{-\frac{(\ln(r)-\mu)^2}{2\sigma^2}} dr, \tag{7.15}$$

where

$$ETD(r) = \left(\frac{\pi}{6}\right)^{1/9} D\frac{D+\alpha/\beta}{\alpha/\beta}v^{-1/9}.$$

Finally, based on the TCP results, the expected number of nodules with positive response is computed for the single-valued model and the lognormal model. Both calculations are compared with the actual number of positive responses. Section 7.5.2 presents the obtained results.

7.3.2 A clinical case with inhomogeneous dose distributions over tumors

In section 7.2.2, a framework for incorporating the variability of the tumor-to-blood ratios and non-uniform dose conditions into the calculation of TCP was introduced. In order to quantify the impact of these issues in a clinical case, the presented concepts are applied to the second melanoma patient treated with the RA-6 BNCT beam.

As described in section 5.4.2, the patient was a 75-year-old woman with a nodular melanoma progression at the front side of her inferior right leg. At the time of the treatment, the patient presented 12 nodules that were labelled for evaluation purposes (10 out of 12 lay within the target area). Tumor dose calculations were carried out using NCTPlan treatment planning system [37]. The 3D dose distribution for each nodule as well as their volumes were obtained prior to the irradiation using the DVH Tool [38].

For the sake of simplicity, tumor control probabilities are presented for two nodules of comparable size: one located in a high dose region near the beam entrance point (nodule 10, Table 5.3), and one located in a low dose region near the periphery of the target area (nodule 12, Table 5.3). Probabilities are computed using expression (7.14), taking g to be the logit function given in Eq. (7.8). Then, $c = -\frac{1}{9}$ and h is the function given by

$$h(\mathbf{x}, r) = \left(\frac{\pi}{6}\right)^{1/9} D(\mathbf{x}, r)\, \frac{D(\mathbf{x}, r) + \alpha/\beta}{\alpha/\beta}, \tag{7.16}$$

with $\alpha/\beta = 2.5$ Gy for melanomas. Four levels of approximations are taken into account for the calculations of $TCPs$. In TCP_1 neither the tumor dose inhomogeneity nor the ratio variability are taken into account. For TCP_2 only tumor dose inhomogeneities are included in calculations while in TCP_3 only variations of the tumor-to-blood ratios are considered. Finally, TCP_4 comprises all the mentioned variabilities. Results are shown in section 7.5.3

7.4 Estimation of the ratio distribution from clinical responses

In Chapter 6, a new approach to determine tumor-to-blood ratios was introduced. It is a statistical method that uses maximum likelihood estimation based on the clinical outcome of BNCT treatments. In that chapter, the hypothesis of a single value of r was assumed. Then, using the data of the first BNCT treatment carried out in Argentina, the value of r that best adjusted the clinical outcome was determined. The obtained value of r was interpreted as a kind of effective ratio in the sense that, although it might be different from all 39 actual ratios, it was the ratio that assigned each nodule a TCP as compatible as possible with the actual response.

To go further with this approach, the mle method is now applied to determine the parameters of the lognormal distribution function for the ratio that best predict the clinical response. Consider as in section 6.2.4 the random variables X_i $(i = 1, \ldots, 39)$ given by

$$X_i = \begin{cases} 1 & \text{if nodule } i \text{ shows complete response} \\ 0 & \text{otherwise} \end{cases}$$

and fixed values of μ and σ (as defined in Eq. [7.3]). Each X_i is a Bernoulli random variable with $P(X_i = 1|\mu, \sigma) = TCP_i(\mu, \sigma)$ and $P(X_i = 0|\mu, \sigma) = 1 - TCP_i(\mu, \sigma)$, where TCP_i is the tumor control probability of nodule i obtained from Eq. (7.5), with

the conditional probability given by Eq. (6.3). Let x_i denote the actual clinical result of nodule i. Assuming independence between the response of different nodules, the likelihood function is given by:

$$\begin{aligned} L(\mu,\sigma) &= P(X_1 = x_1, \ldots, X_{39} = x_{39}|\mu,\sigma) \\ &= \prod_{i=1}^{39} P(X_i = x_i|\mu,\sigma) \\ &= \prod_{i=1}^{39} TCP_i\,(\mu,\sigma)^{x_i}\,(1 - TCP_i\,(\mu,\sigma))^{(1-x_i)} \end{aligned} \tag{7.17}$$

Again, the maximum likelihood estimates for μ and σ are the values $\hat{\mu}$ and $\hat{\sigma}$ that maximize the likelihood function. Proceeding as described in section 6.2.4, confidence intervals for $\hat{\mu}$ and $\hat{\sigma}$ are determined applying a parametric bootstrap method.

7.5 Results and discussion

7.5.1 Lognormal fitting

A lognormal distribution is fitted to the experimentally-determined tumor-to-blood ratios (Table 7.1) by a maximum likelihood method. The parameters obtained in this way are $\mu = 1.11$ and $\sigma = 0.58$, with 95%-confidence intervals of $[0.96, 1.26]$ and $[0.48, 0.70]$, respectively. The Lilliefors test accepts the lognormal fitting at all possible levels. Figure 7.1 shows the cumulative distribution function (CDF) of the lognormal random variable with the obtained parameters (named, measurement-based distribution), together with the empirical cumulative distribution function. The agreement is amazingly good. Recall that the fitted data were obtained by collecting all the experimental measurements published in [11, 29, 54, 64, 69, 87]. It was not necessary to omit any experimental value, although intuition could consider some of them outliers. These results suggest that both the empirical and lognormal distributions can be used indistinctly to compute confidence intervals for the ratios and doses, the lognormal distribution having the advantage of being expressed with an explicit formula.

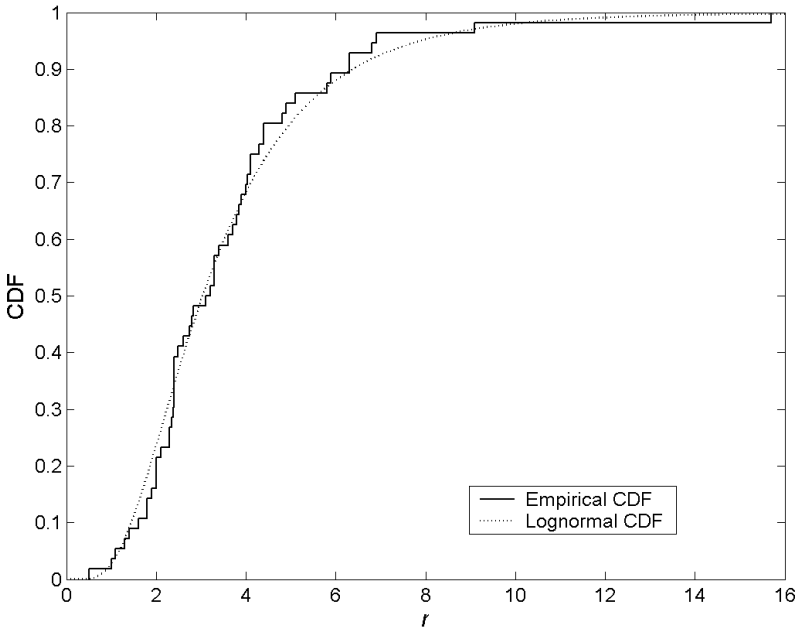

Figure 7.1: Comparison of the empirical and fitted lognormal cumulative distribution functions.

A 68% confidence interval for the ratio is $[1.71, 5.37]$. Therefore, a 68% confidence interval for the absorbed dose is obtained by computing the absorbed dose at the ends of the interval for the ratio. This way to report the dose is more consistent than the usual MEAN±SD, since the dose probability distribution is far from being symmetric.

7.5.2 The effect of the tumor-to-blood ^{10}B ratio variability

Table 7.2 shows the expected absorbed dose for each of the 39 nodules present in patient #1 case, together with a 68% confidence interval computed from the measurement-based lognormal distribution of r. Recall that the expected absorbed dose or MEAN is the dose for $\bar{r} = 3.58$ (see Eq. [7.2]). Note also the asymmetry of the confidence interval which, as already pointed out, is more representative than the MEAN±SD. In addition, the width of the confidence interval reveals how the variability of the ratios affects the reported absorbed doses.

Nod. ID	Dose RBE Gy	Nod. ID	Dose RBE Gy
1	$20.7^{+8.4}_{-8.8}$	21	$13.4^{+3.1}_{-3.2}$
2	$26.1^{+10.5}_{-11.0}$	22	$20.7^{+8.4}_{-8.8}$
3	$24.3^{+9.8}_{-10.2}$	23	$22.4^{+9.1}_{-9.4}$
4	$26.1^{+10.5}_{-11.0}$	24	$20.7^{+8.4}_{-8.8}$
5	$24.3^{+9.8}_{-10.2}$	25	$20.7^{+8.4}_{-8.8}$
6	$22.4^{+9.1}_{-9.4}$	26	$18.9^{+7.7}_{-8.1}$
7	$18.8^{+5.3}_{-5.6}$	27	$15.2^{+6.2}_{-6.5}$
8	$17.1^{+6.9}_{-7.3}$	28	$20.7^{+8.4}_{-8.8}$
9	$13.4^{+3.1}_{-3.2}$	29	$11.7^{+4.8}_{-5.0}$
10	$26.1^{+10.5}_{-11.0}$	30	$9.9^{+4.0}_{-4.2}$
11	$27.9^{+11.1}_{-11.7}$	31	$8.1^{+3.3}_{-3.4}$
12	$29.6^{+11.8}_{-12.4}$	32	$9.8^{+1.6}_{-1.7}$
13	$31.4^{+12.6}_{-13.2}$	33	$6.3^{+2.6}_{-2.7}$
14	$11.6^{+2.4}_{-2.5}$	34	$6.3^{+2.6}_{-2.7}$
15	$27.9^{+11.1}_{-11.7}$	35	$4.5^{+2.0}_{-1.9}$
16	$17.0^{+4.5}_{-4.7}$	36	$4.5^{+2.0}_{-1.9}$
17	$24.3^{+9.8}_{-10.2}$	37	$2.7^{+1.1}_{-1.2}$
18	$26.1^{+10.5}_{-11.0}$	38	$2.7^{+1.1}_{-1.2}$
19	$29.6^{+11.8}_{-12.4}$	39	$17.1^{+6.9}_{-7.3}$
20	$29.6^{+11.8}_{-12.4}$		

Table 7.2: Dosimetry of the clinical case with homogeneous tumor dose distributions. Expected absorbed dose with a 68% confidence interval computed from the measurement-based lognormal distribution.

Table 7.3 shows the tumor control probability of the nodules computed from a single value of r, i.e. $\bar{r} = 3.58$ (TCP_1), and from the lognormal distribution of r (TCP_2). On the basis of these results, different conclusions may be drawn. The single-valued model overestimates the TCP for nodules in the good cases (those with good chances of positive response) and underestimates it in the bad cases, just as it was predicted in Ref. [22]. This behavior became clearly manifest for the 25 nodules considered the target of the treatment. Since the $TCPs$ of these nodules are expected to be high, the single-valued model would have to overestimate all computed $TCPs$. In fact, nodules 1 to 28 excluding nodules 14, 16 and 21 in Table 7.3 are the nodules considered the target of the treatment, and the single-valued model overestimates the $TCPs$ of all of them.

On the other hand, the expected number of positive responses derived from the single-valued model is 28.9, while for the lognormal distribution is 26.1. Since the observed number of positive responses in this clinical case was 23, these results show the tendency for the single-valued model to overestimate $TCPs$. Note that the number of $TCPs$ overestimated with the single-valued model is much greater than the number underestimated (Table 7.3).

To evaluate if the difference between the observed and expected numbers of positive responses can be due to the randomness of the process, the p-value is computed for each model. Let N denote the random variable "number of positive responses", $E(N)$ its expected value, and $N_{obs} = 23$ the observed value of N. The p-value for the single value model is the probability of obtaining a difference such as the one observed between N and $E(N)$, assuming that the model is correct. That is

$$\begin{aligned} p\text{-value} &= P(|N - E(N)| \geq |N_{obs} - E(N)|) \\ &= P(|N - 28.9| \geq |23 - 28.9|), \end{aligned}$$

where $E(N)$ and the probability are computed under the assumption that each nodule has the TCP derived from the single value model. The p-value for the lognormal model is obtained analogously. Therefore, a small p-value (typically, p-value < 0.05 or p-value

Nod. ID	TCP_1	TCP_2	O/U	Output	Nod. ID	TCP_1	TCP_2	O/U	Output
1	0.97	0.83	O	NC	21	0.78	0.69	O	NC
2	0.97	0.85	O	CR	22	0.97	0.84	O	CR
3	0.99	0.92	O	CR	23	0.98	0.87	O	CR
4	0.99	0.93	O	NC	24	0.96	0.82	O	CR
5	0.99	0.90	O	CR	25	0.96	0.81	O	CR
6	0.98	0.87	O	CR	26	0.96	0.81	O	CR
7	0.95	0.87	O	CR	27	0.90	0.71	O	CR
8	0.92	0.72	O	CR	28	0.97	0.83	O	CR
9	0.70	0.61	O	PR	29	0.58	0.45	O	CR
10	0.99	0.92	O	CR	30	0.32	0.31	O	NC
11	0.99	0.93	O	NC	31	0.18	0.22	U	NC
12	1	0.96	O	CR	32	0.38	0.36	O	PR
13	1	0.97	O	CR	33	0.04	0.09	U	NC
14	0.56	0.50	O	CR	34	0.05	0.11	U	NC
15	0.99	0.95	O	CR	35	0.02	0.05	U	PD
16	0.91	0.81	O	CR	36	0.01	0.03	U	PD
17	0.99	0.91	O	CR	37	0	0	-	PD
18	0.99	0.92	O	CR	38	0	0	-	PD
19	1	0.96	O	CR	39	0.93	0.75	O	NC
20	1	0.96	O	CR					

Table 7.3: Tumor control probabilties computed with the single-valued model (TCP_1) and with the lognormal distribution model (TCP_2). CR, PR, NC and PD as in Table 5.2. O/U = overestimation/underestimation of the single-valued model.

< 0.01) suggests that the model should be rejected. In the case of the single-valued model the p-value is almost zero. This result implies the rejection of the model. On the contrary, the p-value for the lognormal model is 0.23, which means that the observed number of positive responses is compatible with the model. In other words, the lognormal model derives a difference between the observed and the predicted number of positive responses that has very good chances to occur.

Nod. ID	v (cm^3)	$\bar{D}(\bar{r})$ (RBE Gy)	$D_{\min}(\bar{r})$ (RBE Gy)	$D_{\max}(\bar{r})$ (RBE Gy)	TCP_1	TCP_2	TCP_3	TCP_4
10	0.87	44.0	38.3	48.0	1	1	0.97	0.97
12	0.78	22.1	16.8	28.4	0.93	0.88	0.75	0.68

Table 7.4: Effect of dose inhomogeneity and tumor-to-blood ratio variability on tumor control probabilities. $TCP_1 = TCP$ for a single ratio and uniform doses, $TCP_2 = TCP$ for a single ratio and inhomogeneous doses, $TCP_3 = TCP$ for variable ratios and uniform doses, and $TCP_4 = TCP$ for variable ratios and inhomogeneous doses.

7.5.3 The effect of dose inhomogeneity

Table 7.4 shows the behavior of the TCP in the presence of dose inhomogeneity and tumor-to-blood ratio variability for two nodules of comparable volume. Nodule 10, located in a high dose region of the target area, has a mean dose of 44.0 RBE Gy and a dose variability of 20% over its volume (for $\bar{r} = 3.58$). This example reveals that in the limit of high doses, such inhomogeneities do not affect the value of the TCP_1, i.e. $TCP_2 = TCP_1$. On the other hand, the tumor-to-blood ratio variability slightly modify the TCP ($TCP_3 \simeq TCP_1$), and this small change is also reflected in TCP_4 that combines the ratio variability and dose inhomogeneities. Thus, there is no considerable change in the TCP for nodule 1 when both effects are considered in calculations (0.97 vs 1). This should not be surprising: in this tumor, the minimum dose is very high. In fact, even if the tumor control probability is computed as in TCP_3 but setting, for each r, the dose of the whole tumor as the minimum dose, the result is 0.95. Therefore, the value of the TCP will be close to 1 no matter how the TCP is computed.

A different case is that of nodule 12. This tumor has a mean dose of 22.1 RBE Gy and a dose variability of almost 41 % (for $\bar{r} = 3.58$). While the TCP_1 happens to be high, the "correct" probability TCP_4 is much lower than the value of TCP_1(i.e., 0.68 vs 0.93). Note that for this tumor, the dose inhomogeneity as well as the ratio variability substantially affects the calculation of the TCP (0.88 and 0.75 vs 0.93, respectively). Moreover, these effects are not simply additive. Indeed, if the dose inhomogeneity and the ratio variability are considered separately, the TCP value is reduced in 0.05 and 0.18, respectively. When

these effects are combined, the TCP is reduced in 0.25, which is greater than 0.05+0.18. The control probability of tumor 12 computed from the mean value of the ratio and the average dose was 0.93, which would be an acceptable value for most physicians. However, when both ratio variability and dose inhomogeneity are considered, the TCP reduces to 0.68, a value that would lead to a reformulation of the treatment in most cases. Recall that the responses of nodules 10 and 12 at 14-week follow up were NC and PD respectively but a longer time was needed to assess the final clinical outcome of this patient.

Generally speaking, if $TCPs$ are computed with the mean value of r and the average dose in tumors, and a treatment is planned so that the tumors have a probability of total response around 0.9, one would observe a considerably worse response. This can be a explanation of the fact that, in many cases, responses in BNCT treatments are not as good as expected. Note that the volume of tumor 12 is less than 1 cm^3. This effect can be even more drastic in larger tumors, where dose inhomogeneity is likely to be higher.

7.5.4 Mle of the lognormal distribution parameters

The estimated parameters of the lognormal distribution based on the clinical outcome of a nodular melanoma patient are presented. The values of μ and σ that maximize the likelihood function $L(\mu, \sigma)$ are $\hat{\mu} = 0.85$ and $\hat{\sigma} = 0.51$. The parametric bootstrap derives 95%-confidence intervals of $[0.49, 1.27]$ and $[0, 1.06]$, respectively.

Figure 7.2 compares the measurement-based lognormal distribution of the ratios, and the lognormal probability density function derived from clinical outcome of a BNCT treatment (named, clinical-based distribution). The mean values of these distributions are 3.58 and 2.66, with standard deviations of 2.27 and 1.45, respectively. The clinical-based distribution shows less variability than the measurement-based distribution and is concentrated in smaller values of r. The difference between the variabilities has a simple explanation. The clinical-based distribution reflects the variation of the ratios in 39 nodules of a single patient at the same moment. The measurement-based distribution,

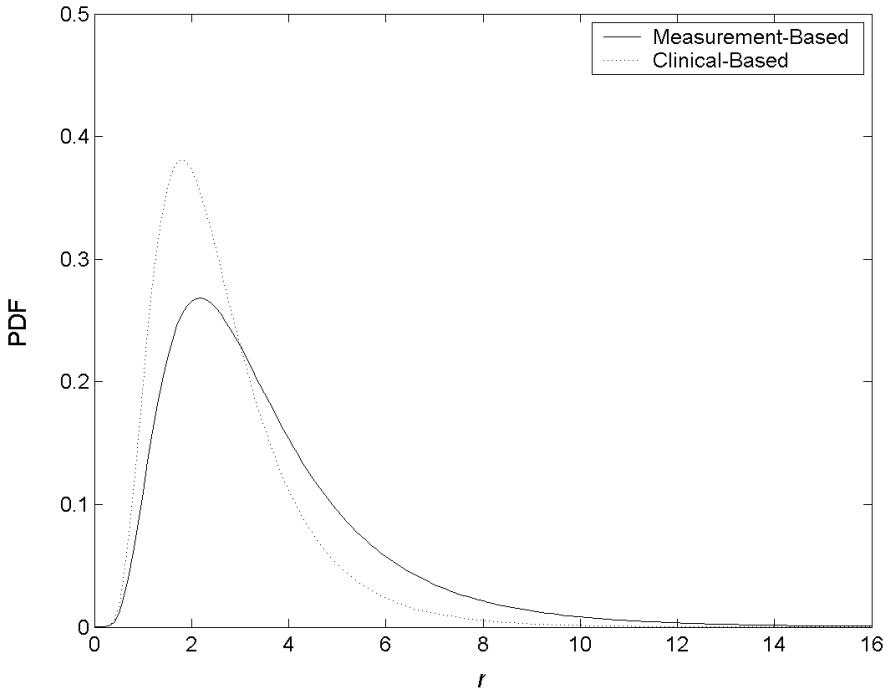

Figure 7.2: Comparison of the lognormal distributions obtained from the fitting of the experimentally-determined tumor-to-blood ratios (Measurement-Based) and from the clinical outcome of a BNCT treatment (Clinical-Based).

on the contrary, was obtained from the ratios of different types of melanoma in different persons. In fact, one might have expected an even smaller deviation in the clinical-based distribution. However, it should be noted that the mle parameter estimation involves the assumptions generally used in treatment planning, for example, to compute irradiation times (independence between nodules' responses, uniform boron concentration throughout each tumor volume, a constant tumor-to-blood ratio during irradiation time, etc.). Since parameters are obtained by matching the clinical outcome to the predictions of the model, the resulting distribution not only reflects variability on the tumor-to-blood ratios, but also adjusts the model to reality. It can absorb, for example, the variability of some other parameter that the model considers fixed.

For the difference between the mean values of both distributions, observe that the ratios in a single person does not necessarily behave as the ratios of the whole population.

In addition, the fact that the clinical-based distribution involved only nodular melanomas makes its smaller mean value expectable. As pointed out in the discussions of Chapter 6, there is some evidence to support that the uptake of boron in nodular melanomas may be lesser than that in other types of melanoma [46].

7.6 Concluding remarks

Two density functions are presented to describe the probability distribution of tumor-to-blood ^{10}B concentration ratios in melanomas. Both of them are lognormal distributions. The first is obtained from a collection of experimental measurements of tumor-to-blood ratios. The second is derived from a maximum likelihood estimation based on the clinical outcome of a BNCT treatment. A natural question now is which of them should be used in order to evaluate a future treatment. The main advantage of the measurement-based distribution is that it takes into account the inter-patient variability of the ratio, while the second is based on the clinical outcome of a single patient. The clinical-based distribution should be used, for example, to perform a retrospective analysis of the specific treatment from which it was derived. This would give as a result the ranges of dose that were actually delivered to nodules, rather than the a priori values inferred from the measurement-based distribution (Table 7.2). If a great number of clinical cases is involved in the clinical-based method, one could expect the obtained distribution to get closer to the measurement-based one. As mentioned in the previous section, the mle estimation forces the clinical-based distribution to absorb the variability of some other parameter that the model considers fixed. Therefore, the clinical-based distribution of a good number of patients is likely to be similar to the measurement-based one, but with a greater variability.

Summarizing, as long as the second method is not applied to a good number of patients, the measurement-based lognormal distribution should be preferred to infer the patient's dosimetry. Otherwise, if inter-patient variability is considered in the clinical-based distribution derivation, this model will be more suitable to compute $TCPs$, since

the mle estimation adjusts the TCP model to reality.

The concepts introduced in this work show that the natural variability of the tumor-to-blood ^{10}B concentration ratios conditions the reporting of the absorbed boron dose as well as the biologically weighted total dose. This means that in addition to the usual reporting of expected absorbed doses (i.e., maximum, minimum and average dose), a confidence interval (e.g., 68% confidence interval) should be included for each reported dose. An alternative for condensing that information in a meaningful way is by means of tumor control probability models. Then, efforts in this direction should be intensified in BNCT.

As a contribution in this field, this work presents a tumor control probability model that takes into account both the variability of the ratios and the possible inhomogeneity of the dose throughout a tumor. This model is first tested in a clinical case where tumors were small and dose could be considered homogeneous in each nodule. The presented TCP model gives a good prediction of the number of positive responses, in opposition to the statistically unacceptable prediction of the classical model based on a single ratio. Next, a case with inhomogeneous dose is analyzed. One can infer from this analysis that, unless the tumor is located in a very high dose region (i.e., where even the minimum dose for low values of r is high), the combined effect of ratio variability and dose inhomogeneity can drastically reduce the TCP. This can be an explanation for the unexpectedly poor responses of some BNCT treatments: if the $TCPs$ were computed without taking into account the mentioned effects, the predicted responses would be too optimistic.

Finally, it is worth mentioning that the formalism developed for the non-uniform dose condition is straightforwardly applicable to TCP models of other kinds of radiotherapies.

Chapter 8

Conclusions

8.1 Research summary

The geometry reconstruction technique that is mainly used in treatment planning systems to create the Monte Carlo model is based on the voxel reconstruction method. This is the case of the MacNCTPlan TPS developed by the Harvard-MIT BNCT group [57, 95], which was thoroughly benchmarked by CNEA under the collaborative work between the two BNCT programs. Owing to the deficiencies identified in the geometry modeling technique, an improved voxelization algorithm was introduced together with a detailed analysis of the performance of the voxel reconstruction method for a fixed voxel size of 1 cm^3. The proposed voxel model was verified and clinically validated against numerical and experimental standards of reference. The new algorithm for the voxel model proved better regardless of the particularities of said reference problems. The in-depth comparison showed that the 1 cm resolution of the voxel method agreed to within 10% of all reference data. Since the new algorithm presents many improvements over MacNCTPlan's, and proved well-suited in a variety of simple and complex geometries for ideal and realistic particle sources, its implementation in the MacNCTPlan's successor, i.e. NCTPlan program, was clearly justified. NCTPlan TPS, which is a joint development of CNEA and

the Beth Israel Deaconess Medical Center, has been successfully used in Phase I/II clinical trials for GBM, intracranial melanoma and cutaneous melanoma at Harvard-MIT, and Phase I/II clinical trials for cutaneous melanoma at CNEA. Currently, it is included in selected protocols at Petten (The Netherlands), Nuclear Research Institute (Rez, Czech Republic), and at the University of Birmingham (UK).

In all BNCT treatments carried out at present, skin is considered one of the organs at risk. Moreover, for cases of cutaneous melanoma in extremities, skin is essentially the organ that limits the delivered dose to patients. Since surface boundary areas are those where homogenization can have a more distorting effect, the performance of the voxel model in these regions was analyzed with special emphasis in this thesis.

The investigation of the impact of the voxel grid position with respect to medical images revealed the difficulty for the voxel reconstruction technique to achieve accuracy near boundary regions. Then, guidelines to get the best performance were introduced: the voxel model of an anatomy should be built in order to minimize the proportion of air in surface cells around the beam entrance point.

A theoretical analysis was carried out both to assess the distortion caused by homogenization, and also to estimate the errors due to the materials percentage rounding process. Based on this analysis, a new strategy for the treatment of surface cells was proposed: the average fluence in the surface voxel must be assigned to the barycenter of the portion of the geometry contained in the voxel instead of assigning it to the center of the cell. The performance of the new strategy was tested in different numerical irradiation problems. Results showed that thermal neutron fluence deviations present at shallow depths are reduced by around five times without any detriment of MCNP execution times. Moreover, even if the rules to position the medical images are not followed, the reassignment also provides very accurate estimates. These results represent a substantial improvement to the performance of the NCTPlan voxel model in surface areas. Since this program is currently used in several BNCT projects, and particularly in the cutaneous melanomas

protocol of extremities in Argentina, the new strategy will be implemented in the newer version of the NCTPlan code.

In vivo quantification of the macroscopic boron distribution in different tissues and organs during the treatment of patients is not possible at this stage. Some approximations are then introduced for the dose calculations, essentially by means of parameters that have been historically determined by experimental measurements. Such is the case of the tumor boron concentration, which is computed from boron in blood and its level is described as a static ratio between both concentrations. The experimental approach to estimating the tumor-to-blood ratio is the most natural and direct method. However, due to the high cost of boron drug and the tissue sample requirement, said approach is expensive, time-consuming and invasive for patients. This thesis presents a new approach to determining the tumor-to-blood ^{10}B concentration ratio. It is a statistical method that consists of a maximum likelihood estimation from the clinical outcome of a BNCT treatment. In other words, the estimated ratio is the value that makes the clinical output most probable or likely. The proposed method was applied to the first skin melanoma BNCT treatment performed in Argentina. The statistical-based result, 2.1 ± 0.3, shows excellent agreement with the experimental ratios obtained for the analyzed patient, 2.2 ± 0.3. Also, it is consistent with the experimental data published by the different groups. The mle method is not meant to replace experimental measurements. However, the approach is particularly attractive because it is minimally invasive for patients, and can play an important role in treatment planning and in retrospective dosimetry analysis. When the presented method is applied to a single patient, the estimated effective ratio can be used for retrospective analysis purposes. Also, a distribution of effective ratios can be obtained from applying the mle method to a good number of patients. Then, the obtained results can be applied for treatment planning calculations in the next patient. Finally, the proposed method can be applied to adjust other parameters involved in the TCP model, such as compound and relative biological effectiveness factors.

It has been described that a large fraction of the dose in BNCT is due to the densely ionizing particles that result from the reaction $^{10}\mathrm{B}(\mathrm{n},\alpha)^{7}\mathrm{Li}$. This dose component can not be measured in patients. Then, for treatment purposes, calculations must be carried out based on several assumptions. It is usual to consider a single value of the tumor-to-blood ratio in order to compute absorbed doses and tumor control probabilities in BNCT treatments. The single value is adequate to compute the expected absorbed dose. However, as pointed out by Culbertson *et al.* [22], a distribution of ratios is more appropriate due to measurements uncertainties and to biological diversity, and it is necessary to obtain confidence intervals for the dose, and also to describe the probability distribution of possible doses. Moreover, the behavior of tumor control probability respect to the dose is highly nonlinear, which makes the computation of these probabilities from a single value of the ratio very questionable. In this work, two density functions were presented to describe the probability distribution of tumor-to-blood $^{10}\mathrm{B}$ concentration ratios in melanomas for the first time. These are lognormal distributions, one derived from a collection of experimental measurements of tumor-to-blood ratios, and the other from a maximum likelihood estimation based on the clinical outcome of a BNCT treatment. In both cases, the natural variability of the ratios clearly conditions the reporting of absorbed doses in BNCT. This would mean that in addition to the IAEA recommendations for reporting doses [49] (i.e., expected maximum, minimum and average doses), a confidence interval should be also included (e.g., 68% confidence interval).

In addition to the tumor-to-blood ratio variability, the dose inhomogeneity over the target volume may also affect the tumor control probability. In this thesis, a comprehensive framework for incorporating the variability of the tumor-to-blood ratios into the calculation of absorbed doses and TCP in BNCT treatments was introduced, and applied to cases of malignant melanomas. Furthermore, a tumor control probability model was developed for the first time in BNCT, which considers the effect of the ratio variability as well as the possible dose inhomogeneity throughout the tumor volume. This model

was first tested in a clinical case where tumors were small and dose could be considered homogeneous in each nodule. The presented TCP model gives a good prediction of the number of positive responses, in opposition to the model based on the mean value of tumor-to-blood ratios which predicts a statistically unacceptable number. Next, a case with inhomogeneous dose was analyzed. Results showed that, unless the tumor is located in a very high dose region, the combined effect of ratio variability and dose inhomogeneity can drastically reduce the TCP. This can be an explanation for the unexpectedly poor responses of some BNCT treatments: if the $TCPs$ were computed without taking into account the said effects, the predicted responses would be too optimistic.

Finally, it should be emphasized that the formalism developed for the non-uniform dose condition is straightforwardly applicable to TCP models of other radiotherapies.

8.2 Future work

Dose calculations in the voxel model are performed with the assumption that charged particle equilibrium conditions (CPE) are satisfied everywhere in the geometry [1]. In the case of photons, CPE condition does not hold for build-up regions, such as the interface between air and skin in patients. The actual dose delivered in the first millimeters of the tissue is lower than the corresponding computed kerma value, which in a sense constitutes a conservative position in terms of normal tissue dose tolerance. However, a more accurate estimation of dose could be obtained if coupled photon-electron transport calculations are carried out with MCNP. The drawback is that coupled neutron-photon-electron calculations would probably be too computationally expensive. A feasibility analysis of this approach should be of interest.

It has been described that in attempting to improve the accuracy of the NCTPlan voxel model further, two lines of action naturally arise: to reduce the 20% step used for rounding material percentages and to decrease the voxel size. A reduction in rounding

percentages increases the number of material mixtures to be considered in calculations. If the percentage step is set to 10%, the resulting number of materials is 286. This is not a problem for a modern computer and execution times are not expected to change. Then, since the error is roughly reduced to a half by rounding material proportions to the closest 10%, this change in the volume percentage increment should be considered for a next upgrade in the voxel reconstruction algorithm. On the other hand, it has been shown that considerable improvements can be obtained in surface areas with minimum computational costs, using the reassignment strategy. Then, a reduction in the voxel size, with the consequent increase of runtimes, may not be well-justified in most GBM and melanoma treatment plans. However, if the NTPlan voxel model is to be used for small anatomies such as a portion of a liver, or for small animals experiments, then calculations should be performed with a smaller voxel size. In order to compensate for the increased execution times, a reduction of the $21 \times 21 \times 25$ cm^3 fixed box should be evaluated.

The Phase I/II clinical trial for cutaneous melanoma in Argentina is continuously recruiting patients. More efforts should be devoted to treatment optimization through further adjustments of the proposed tumor control probability model, as well as new developments of normal tissue complication probability models. A validation of these models is plausible to the extent that a substantial number of patients are treated.

Appendix A

List of acronyms

BNCT Boron Neutron Capture Therapy

BPA-F Boronophenylalanine-Fructose complex

CBE Compound Biological Effectiveness

CDF Cumulative Distribution Function

CNEA Comisión Nacional de Energía Atómica

CT Computed Tomography

DVH Dose Volume Histogram

EKG Electrocardiogram

ENDF Evaluated Nuclear Data File

EORTC European Organisation for Research and Treatment of Cancer

FU Follow Up

GBM Glioblastoma Multiforme

HPGe High-Purity Germanium

ICRP International Commission on Radiological Protection

ICRU International Commission on Radiation Units and Measurements

JAERI Japan Atomic Energy Research Institute

JCDC JAERI Computational Dosimetry System

KERMA Kinetic Energy Released in MAtter

LET Linear Energy Transfer

MCNP Monte Carlo N-Particle

MIT Massachusetts Institute of Technology

mle Maximum Likelihood Estimation

MU Monitor Units

NCT Neutron Capture Therapy

NCTPlan Neutron Capture Therapy Plan

PDF Probability Density Function

ppm Parts per million

RBE Relative Biological Effectiveness

ROI Region Of Interest

RTOG Radiation Therapy Oncology Group

SERA Simulation Environment for Radiotherapy Applications

TCP Tumor Control Probability

TLD Termoluminiscense Dosimeter

TPS Treatment Planning System

VOI Volume Of Interest

WHO World Health Organization

Appendix B

Calculations for the voxel model

B.1 Material homogenization

In this section, the calculation of the probability that a neutron undergoes at most one reaction inside an infinite p centimeter thick slab is presented.

Consider an infinite p centimeter thick slab ($0 < p < 1$) of a low absorbing material M and macroscopic total cross section Σ, perpendicularly irradiated with a monoenergetic neutron beam represented by an infinite planar source. Since M is a low absorbing material, only scattering reactions need be considered.

Let $\mathbf{p} = p$ cm be the slab thickness. The probability that a neutron undergoes at most one reaction inside the slab is

$$P = P_0 + P_1, \tag{B.1}$$

where P_0 is the probability that a neutron does not suffer its first collision in the slab, and P_1 the probability that a neutron suffers its first collision inside the slab and the second outside the slab. The probability that a neutron does not suffer its first collision in the slab is

$$P_0 = e^{-\mathbf{p}\Sigma_0}. \tag{B.2}$$

To compute P_1, let L_1, L_2 and Θ be the random variables representing the track length to the first collision, the track length from the first to the second collision, and the angle between the beam direction and the neutron direction after the first collision, respectively. Then,

$$\begin{aligned} P_1 &= P(0 < L_1 < \mathbf{p} \cap L_1 + L_2 \cos\Theta > \mathbf{p}) \\ &= P\left(0 < L_1 < \mathbf{p} \cap L_2 > \frac{\mathbf{p} - L_1}{\cos\Theta}\right). \end{aligned}$$

Since L_1 is independent of L_2 and Θ, the joint probability density $f_{L_1 L_2 \Theta}$ is

$$\begin{aligned} f_{L_1 L_2 \Theta}(l_1, l_2, \theta) &= f_{L_1}(l_1) f_{L_2 \Theta}(l_2, \theta) \\ &= f_{L_1}(l_1) f_{L_2|\Theta}(l_2|\theta) f_{\Theta}(\theta), \end{aligned}$$

where $f_{L_2|\Theta}$ denotes the conditional density of L_2 given Θ. Angles Θ between 0 and $\pi/2$ occur with a probability density of $2\sin(\theta)\cos(\theta)$. The probability density of L_1 is Σ $e^{-l_1\Sigma}$. Suppose the angle between the beam direction and the neutron direction after the first collision is θ, and let $\Sigma' = \Sigma'(\theta)$ be the macroscopic cross section for the neutron energy after collision. The conditional density[1] of L_2 given $\Theta = \theta$ is $f_{L_2|\Theta}(l_2|\theta) = \Sigma' e^{-l_2\Sigma'}$. Then, Σ' must be computed.

Consider a single collision between a neutron with incident energy E_0 and an hydrogen nucleus at rest. From the conservation laws of an elastic scattering in the center-of-mass system, and their subsequently transformation to the lab system [63], the energy E of the scattered neutron can be written

$$\frac{E}{E_0} = \cos^2\theta.$$

For s-wave neutrons, the cross section formula follows the $1/v$ law. Then,

$$\Sigma = \frac{c}{\sqrt{E_0}} \tag{B.3}$$

[1]This conditional density function may change after the neutron exits the slab. However, it does not affect the computation of the desired probability.

	P		
$\Sigma\backslash\mathbf{p}$	0.1	0.5	0.9
0.1	0.9994	0.9908	0.9765
0.5	0.9908	0.8946	0.7762
1.0	0.9723	0.7468	0.5347
1.5	0.9490	0.6085	0. 3568
2.0	0.9227	0.4896	0. 2346

Table B.1: Probability that a neutron undergoes at most one collision in a slab of thickness $\mathbf{p}$ and macroscopic total cross section Σ.

and

$$\Sigma' = \frac{c}{\sqrt{E}}. \tag{B.4}$$

Combining expressions (B.3) and (B.4),

$$\begin{aligned} \Sigma' &= \Sigma\sqrt{\frac{E_0}{E}} \\ &= \frac{\Sigma}{\cos\theta}. \end{aligned}$$

Therefore,

$$\begin{aligned} P_1 &= \int_0^{\pi/2}\int_0^{\mathbf{p}}\int_{\frac{\mathbf{p}-l_1}{\cos\theta}}^{+\infty} \Sigma e^{-l_1\Sigma}\frac{\Sigma}{\cos\theta}e^{-l_2\frac{\Sigma}{\cos\theta}}2\sin(\theta)\cos(\theta)dl_2dl_1d\theta \\ &= \int_0^{\pi/2}\int_0^{\mathbf{p}}\int_{\frac{\mathbf{p}-l_1}{\cos\theta}}^{+\infty} 2\Sigma^2 e^{-l_1\Sigma}e^{-l_2\frac{\Sigma}{\cos\theta}}\sin(\theta)dl_2dl_1d\theta. \end{aligned} \tag{B.5}$$

Equation (B.5) cannot be solved analytically. Then, to have an estimate of the probability $P = P_0 + P_1$, Eq. (B.5) was numerically computed for different values of $\mathbf{p}$ and a suitable range of Σ. For example, the mean free path of neutrons in muscle with energies in the range of 1/40 eV to 1 keV is about 0.53 cm, which corresponds to a value of Σ of 1.88 cm^{-1}. Table B.1 presents the results obtained for the probability P.

Note that the probability P for photons is even greater than for neutrons.

B.2 Material percentage rounding

In this section, the average fluence relative difference for slabs p and $p-0.1$ cm thick is computed.

As shown in section 4.2.1, the average fluence in the portion A of an infinite p cm thick slab, of material M and macroscopic total cross section $\Sigma^M << 1/\mathbf{p}$, perpendicularly irradiated with an infinite planar source is

$$\overline{\Phi} = \frac{N}{\text{cm}^2}\left(2-\frac{1}{\mathbf{p}\Sigma^M}+\frac{e^{-\mathbf{p}\Sigma^M}}{\mathbf{p}\Sigma^M}\right), \tag{B.6}$$

where $\mathbf{p}$ =p cm, and N is the number of incident particles traversing the 1 cm^2 cross section of A. If $p \geq 0.1$, the relative difference between the average fluences for p and $p-0.1$ can be obtained from equation (B.6). Then,

$$\Delta\left(\Sigma^M, p\right) = \begin{cases} \dfrac{\left(2-\frac{1}{\mathbf{p}\Sigma^M}+\frac{e^{-\mathbf{p}\Sigma^M}}{\mathbf{p}\Sigma^M}\right)-\left(2-\frac{1}{(\mathbf{p}-\mathbf{0.1}\text{cm})\Sigma^M}+\frac{e^{-(\mathbf{p}-\mathbf{0.1}\text{cm})\Sigma^M}}{(\mathbf{p}-\mathbf{0.1}\text{cm})\Sigma^M}\right)}{\left(2-\frac{1}{\mathbf{p}\Sigma^M}+\frac{e^{-\mathbf{p}\Sigma^M}}{\mathbf{p}\Sigma^M}\right)} & 0.1 < p \leq 1 \\ \dfrac{0.1\text{cm}\ \Sigma^M-1+e^{-0.1\text{cm}\ \Sigma^M}}{0.2\text{cm}\ \Sigma^M-1+e^{-0.1\text{cm}\ \Sigma^M}} & p = 0.1. \end{cases}.$$

Figure B.1 shows the graph of function Δ for suitable values of Σ^M. As can be seen, Δ is a decreasing function of p and an increasing function of Σ^M. Note that Δ coincides with the relative error caused by the material percentage rounding whenever p is an odd multiple of 0.1. Therefore, to find an upper bound of the error caused by rounding, only the case $p = 0.1$ must be considered.

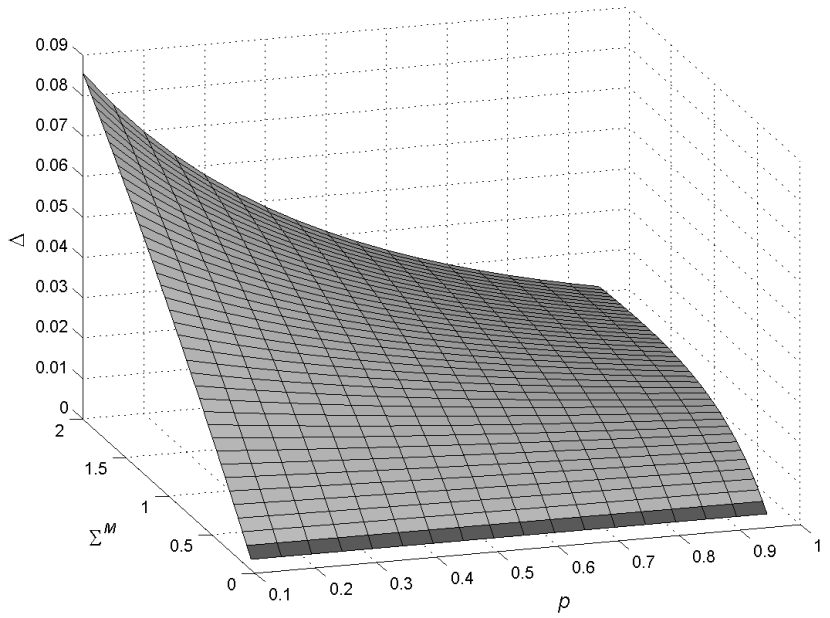

Figure B.1: Relative difference between the average fluences for p and $p-0.1$ cm thick slabs.

Appendix C

Numerical simulations with MCNP

This appendix describes the numerical simulations carried out with MCNP to verify the influence of the material homogenization and material percentage rounding for slabs and sources that are not infinite.

Slabs considered for simulations consisted in acrylic boxes with 40×40 cm^2 cross section and variable thickness p cm ($0.1 < p < 1$, and p a multiple of 0.1). For each original slab, the voxel model with homogeneous mixed materials was constructed. To asses the effect of homogenization only, the material percentage rounding was not carried out. Acrylic composition described in Ref. [1] was used in the problems. Two irradiation sources were used in simulations: a 5 keV monodirectional planar disk neutron source of 10 cm radius, and the RA-6 BNCT neutron beam source of 7.5 cm radius (see section 5.1.2). Note that the characteristics of these neutron sources are quite different. In the case of real slabs, tallies were computed in volumes of 1 cm^2 cross section and p cm thick. For the slab voxel models, tally volumes coincided with the 1 cm^3 cells. Estimates of the average fluence in these volumes were obtained using F4 tally type in MCNP. All calculations were run to high statistical convergence with statistical uncertainties of less than 1%.

Table C.1 shows the average fluences per source particle in the original and voxelized

p	$\overline{\Phi}_a$	$\overline{\Phi^*_a}$	$\tilde{\Delta}^h_a$	$\overline{\Phi}_b$	$\overline{\Phi^*_b}$	$\tilde{\Delta}^h_b$
cm	$(1/\text{cm}^2)$	$(1/\text{cm}^2)$	(%)	$(1/\text{cm}^2)$	$(1/\text{cm}^2)$	(%)
0.1	1.09(1)	1.08(1)	0.3	1.46(1)	1.43(1)	2.5
0.2	1.17(1)	1.16(1)	0.2	1.51(1)	1.49(1)	1.3
0.3	1.24(2)	1.24(1)	0.8	1.55(1)	1.54(1)	0.6
0.4	1.31(1)	1.31(1)	0.1	1.59(1)	1.58(1)	0.5
0.5	1.36(1)	1.37(1)	-0.7	1.63(1)	1.62(1)	0.4
0.6	1.42(1)	1.43(1)	-0.6	1.65(1)	1.65(1)	0.1
0.7	1.47(2)	1.48(1)	-0.5	1.69(1)	1.68(1)	0.3
0.8	1.53(1)	1.53(1)	0.3	1.71(1)	1.71(1)	0.2
0.9	1.57(2)	1.57(1)	-0.1	1.73(1)	1.72(1)	0.1

Table C.1: Average fluences per source particle in a p cm-thick slab ($\overline{\Phi}$), and its corresponding voxelized model ignoring material percentage rounding ($\overline{\Phi^*}$). $\tilde{\Delta}^h$ denotes average fluence percentage relative differences. Subscripts a and b are used for the ideal and RA-6 sources, respectively.

slabs for a tally volume located at the beam entrance point ($\overline{\Phi}$ and $\overline{\Phi^*}$, respectively), and their percentage relative differences ($\tilde{\Delta}^h$). Subscripts a and b are used for the ideal and RA-6 sources, respectively. Note that in this comparison the homogenization effect is the only one considered. As can be seen, relative differences are smaller than 1% and 2.5% for the ideal and real neutron source. Since these values are of the same order as the statistical uncertainties for numerical values, average fluences can be considered the same in the original and voxelized slabs.

Now, consider the material rounding performed by NCTPlan voxel reconstruction method. By the material assignment procedure, materials proportions are rounded to a multiple of 0.2. When the slab thickness p is an odd multiple of 0.1, the algorithm rounds down the proportion of acrylic and rounds up the proportions of air (see section 3.2.2). Then, to compute the errors caused by rounding in these cases, the average fluence of the original slab must be compared to the average fluence in the voxel model with the corresponding rounded proportions. This means for example, that $\overline{\Phi}_a\,|_{p=0.3}$ in Table C.1

p cm	Δ_a (%)	Δ_b (%)
0.1	7.9	9.7
0.3	6.6	3.7
0.5	4.0	2.8
0.7	2.9	2.2
0.9	2.7	1.1

Table C.2: Errors due to the material rounding to a 20% volume increment. Subscripts a and b are used for the ideal and RA-6 sources, respectively.

must be compared to $\overline{\Phi_a^*}\,|_{p=0.2}$.

Table C.2 shows the errors due to the material rounding to a 20% volume increment for the most disadvantage cases, i.e. for p an odd multiple of 0.1. Note that the relative difference Δ is a decreasing function of p, as observed in Appendix B. Then, the upper bounds of the rounding error are those corresponding to the case $p = 0.1$. These are 7.9% and 9.7% for the ideal and realistic neutron sources, respectively.

Appendix D

Tumor dose probability function

In this appendix, the derivation of the probability density function of the tumor dose from the probability function of the tumor-to-blood ratios is presented.

Let R be the random variable representing the tumor-to-blood ratio and f_R the probability density function of R. It was shown in Chapter 7 that for melanoma patients, the lognormal distribution is the probability function that happens to describe the variability of the ratios best (Table 7.1). Therefore, the probability density of the ratios is given as

$$f_R(r) = \frac{1}{r\sigma\sqrt{2\pi}} e^{-\frac{(\ln(r)-\mu)^2}{2\sigma^2}}, \tag{D.1}$$

with μ and σ the parameters of the lognormal distribution.

Let D denote the random variable "tumor dose". Then,

$$D = D_{b-ind} + RD_{b-dep}\, C_{blood}, \tag{D.2}$$

where D_{b-ind} and D_{b-dep} are the boron-independent and boron-dependent (normalized to 1 ppm) biologically weighted dose, respectively, and C_{blood} is the average value of blood boron concentration during the irradiation time. The cumulative distribution function of

D is

$$\begin{aligned} F_D(d) &= P(D \leq d) \\ &= P(D_{b-ind} + RD_{b-dep}\, C_{blood} \leq d) \\ &= P\left(R \leq \frac{d - D_{b-ind}}{D_{b-dep}\, C_{blood}}\right) \\ &= F_R\left(\frac{d - D_{b-ind}}{D_{b-dep}\, C_{blood}}\right), \end{aligned} \tag{D.3}$$

where F_R is the cumulative distribution of R. Thus, the probability density function of the tumor dose f_D can be computed by

$$\begin{aligned} f_D(d) &= \frac{\partial}{\partial d} F_R\left(\frac{d - D_{b-ind}}{D_{b-dep}\, C_{blood}}\right) \\ &= \frac{1}{D_{b-dep}\, C_{blood}} f_R\left(\frac{d - D_{b-ind}}{D_{b-dep}\, C_{blood}}\right). \end{aligned} \tag{D.4}$$

Since f_R is a lognormal density function with parameters μ and σ (Eq. [D.1]), one obtains, after substitution,

$$f_D(d) = \frac{1}{(d - D_{b-ind})\,\sigma\sqrt{2\pi}} e^{-\frac{\left(\ln\left(\frac{d - D_{b-ind}}{D_{b-dep}\, C_{blood}}\right) - \mu\right)^2}{2\sigma^2}}. \tag{D.5}$$

Expression (D.5) shows that D follows a distribution that inherits the asymmetry of the density function f_R.

Bibliography

[1] F. H. Attix, *Introduction to Radiological Physics and Radiation Dosimetry*, John Wiley & Sons, New York, 1986.

[2] R. F. Barth, A. H. Soloway, R. G. Fairchild and R. M. Brugger, Boron neutron capture therapy for cancer. Realities and prospects. *Cancer* **70** (12), 2995-3007 (1992).

[3] P. Bendel, A. Frantz, J. Silberstein, G. W. Kabalka and Y. Salomon, Boron-11 NMR of boro captate: relaxation and *in vivo* detection in melanoma-bearing mice, *Mag. Reson. Med.* **39**, 439-447 (1998).

[4] S. M. Bentzen and H. D. Thames, Tumor volume and local control probability: clinical data and radiobiological interpretations. *Int. J. Radiat. Oncol. Biol. Phys.* **36** (1), 247-51 (1996).

[5] H. Blaumann, J. Longhino and O. Calzetta Larrieu, Beam Dosimetry at the RA-6 BNCT Facility, *Technical Report* CNEA-CAB 47/009/00 (2000).

[6] H. Blaumann, O. Calzetta Larrieu, J. Longhino and F. Albornoz, BNCT Facility Development at the RA-6 Reactor. In *Frontiers in Neutron Capture Therapy* (M. Hawthorne, K. Shelly and R. Wiersena, Eds.) Vol. 1, pp. 313-317. Plenum Publishing Corporation, New York, 2001.

[7] H. R. Blaumann, S. J. González, J. Longhino, G. A. Santa Cruz, O. A. Calzetta Larrieu, M. R. Bonomi and B. M. C. Roth, Boron neutron capture therapy of skin

melanomas at the RA-6 reactor: a procedural approach to beam set up and performance evaluation for upcoming clinical trials. *Med. Phys.* **31,** 70-80 (2004).

[8] J. F. Briesmeister, *MCNP^{TM} - A General Monte Carlo N-Particle Transport Code 12625-M,* University of California, Los Alamos, 1997.

[9] J. F. Briesmeister, *MCNP - A General Monte Carlo N-Particle Transport Code*, Version 4C, LA-13709-M, 2000.

[10] J. Burian, M. Marek, J. Rataj, S. Flibor, J. Rejchrt, L. Viererbl, F. Sus, H. Honova, L. Petruzelka, K. Prokes, F. Tovarys, V. Dbaly, V. Benes, P. Kozler, J. Honzatko, I. Tomandl, V. Mares, J. Marek and M. Syrucek. Report on the First Patient Group of the Phase I BNCT Trial at the LVR-15 Reactor. http://www.csvts.cz/cns/news/030311r.pdf.

[11] P. M. Busse, R. G. Zamenhof, H. Madoc-Jones, G. Solares, S. Kiger, K. Riley, C. Chuang, G. Rogers and O. Harling, Clinical follow-up of patients with melanoma of extremity treated in phase I boron neutron capture therapy protocol. In *Advances in Neutron Capture Therapy* (B. Larson, J. Crawford and R. Weinreich, Eds.) Vol I, pp. 60-64 Elsevier, 1997.

[12] P. M. Busse, O. K. Harling, M. R. Palmer, W. S. Kiger III, J. Kaplan, I. Kaplan, C. F. Chuang, J. T. Goorley, K. J. Riley, T. H. Newton, G. A. Santa Cruz, X.-Q. Lu and R. G. Zamenhof, A critical examination of the results from the Harvard-MIT NCT program phase I clinical trial of neutron capture therapy for intracranial disease. *J. Neuro-Oncol.* **62,** 111-121 (2003).

[13] O. Calzetta Larrieu, H. Blaumann and J. Longhino, RA-6 Reactor Mixed Beam Design and Performance for NCT Trials. In *Proceedings of the Tenth International Congress on Neutron Capture Therapy* (W. Sauerwein, R. Moss and A. Wittig, Eds.), pp. 155-158. Monduzzi Editore, Bologna, 2002.

[14] O. Calzetta Larrieu, H. Blaumann, J. Longhino and F. Albornoz, BNCT Facility at the RA-6 Reactor. In *Proceedings of the IAEA Technical Committee Meeting on Current Issues of BNCT,* IAEA, Austria, 2001.

[15] G. A. Carlsson, *Theoretical Basis for Dosimetry.* The dosimetry of ionizing radiation. Academic Press, Inc., London, 1985.

[16] N. Cerulloand G. Daquino, A Treatment Planning System Based on Real Boron Distribution and MCNP-4^{a}Code: Results and Discussion Frontiers. In *Frontiers in Neutron Capture Therapy* (M. Hawthorne, K. Shelly and R. Wiersena, Eds.) Vol. 1, pp. 225-2302. Plenum Publishing Corporation, New York, 2001.

[17] M. Chadwick, H. Barschall, R. Caswell, P. DeLuca, G. Hale, D. Jones, R. MacFarlane, J. Meulders, H. Schuhmacher, U. Schrewe, A. Wambersie and P. Young, A consistent set of neutron kerma coefficients from thermal to 150 Mev for biologically important materials. *Med. Phys.* **26** (6), 974-991 (1999).

[18] J. A Coderre, A. D. Chanana, D. D. Joel, E. H. Elowitz, P. L. Micca, M. M. Nawrocky, M. Chadha, J. O. Gebbers, M. Shady, N. S. Peress and D. N. Slatkin, Biodistribution of boronophenylalanine in patients with glioblastoma multiforme: boron concentration correlates with tumor cellularity. *Radiat. Res.* **149**, 163-170 (1998).

[19] J. A. Coderre, M. S. Makar, P. L. Nawrocky, H. B. Liu, D. D. Joel, D. N. Slatkin and H. I. Amols, Derivation of relative biological effectiveness for the high-let radiations produced during boron neutron capture irradiations of the 9L rat gliosarcoma in vitro and in vivo. *Int. J. Radiat. Oncol. Biol. Phys.* **27** (5), 1121-1129 (1993).

[20] J. A. Coderre and G. M. Morris, The Radiation Biology of Boron Neutron Capture Therapy. *Radiat. Res.* **151,** 1-18 (1999).

[21] L. Cohen, The tissue volume factor in radiation oncology. *Int. J. Radiat. Oncol. Biol. Phys.* **8** (10), 1171-1774 (1982).

[22] C. N. Culbertson and K. O. Ott, Probabilistic Treatment of Uncertainties in the Computational Modeling of BNCT for Brain Tumors. In *Proceedings of the Tenth International Congress on Neutron Capture Therapy* (W. Sauerwein, R. Moss and A. Wittig, Eds.), pp. 591-598. Monduzzi Editore, Bologna, 2002.

[23] A. Dagrosa, M. Viaggi, J. Longhino, O. Calzetta, M. Edreira, R. Cabrini, G. Juvenal and M. Pisarev, Experimental Application of BNCT to Undifferenciated Thyroid Carcinoma (UTC). In *Proceedings of the Tenth International Congress on Neutron Capture Therapy* (W. Sauerwein, R. Moss and A. Wittig, Eds.), pp. 685-689. Monduzzi Editore, Bologna, 2002.

[24] M. A. Dagrosa, M. Viaggi, R. Jimenez Rebagliati, V. A. Castillo, D. Batistoni, R. L. Cabrini, S. Cstiglia, G. J. Juvenal and M. A. Pisarev, Biodistribution of p-boronophenylalanine (BPA) in dogs with spontaneous undifferentiated thyroid carcinoma (UTC). *Appl. Radiat. Isotopes* **61,** 911-915 (2004).

[25] F. de Braud, D. Khayat, B. B. R. Kroon, R. Valdagni, P. Bruzzi and N. Cascinelli, Malignant Melanoma. *Crit. Rev. Oncol. Hemat.* **45** (3), 35-63 (2003).

[26] B. G. Douglas, Implications of the cuadratic cell survival curve and human skin radiation "tolerance dose" on fractionation and superfractionation dose selection. *Int. J. Radiat. Oncol. Biol. Phys.* **8**, 1135-1142 (1982).

[27] J. J. Duderstadt and W. R. Martin. *Transport Theory*, John Wiley & Sons, New York, 1979.

[28] P. Ellis, Dose, time and fractionation: a clinical hypothesis. *Clin. Radiol.* **20**, 1-7 (1969).

[29] H. Fukuda, J. Hiratsuka, C. Honda, T. Kobayashi, K. Yoshino, H. Karashima, J. Takahashi, Y. Abe, K. Kanda, M. Ichihashi and Y. Mishima, Boron neutron capture

therapy of malignant melanoma using B-10-paraboronophenylalanine with special reference to evaluation of radiation dose and damage to the normal skin. *Radiat. Res.* **138** (3), 435-442 (1994).

[30] H. Fukuda, J. Hiratsuka, T. Kobayashi, Y. Sakurai, K. Yoshino, H. Karashima, K. Turu, K. Araki, Y. Mishima and M. Ichihashi, Boron neutron capture therapy (BNCT) for malignant melanoma with special reference to absorbed doses to the normal skin and tumor. *Australas Phys. Eng. Sci. Med.* **26** (3), 97-103 (2003).

[31] H. Fukuda, N. Honda, N. Wadabayashi, T. Kobayashi, K. Yoshino, J. Hiratsuka, J. Takahashi, T. Akaizawa, Y. Abe, M. Ichihashi and Y. Mishima, Pharmacokinetics of 10B-p-boronophenylalanine in tumours, skin and blood of melanoma patients: a study of boron neutron capture therapy for malignant melanoma. *Melanoma. Res.* **9**, 75-83 (1999).

[32] H. Fukuda, T. Kobayashi, T. Matsuzawa, K. Kanda, M. Ichihashi and Y. Mishima, RBE of a thermal neutron beam and the ^{10}B(n, α)^{7}Li reaction on cultured B-16 melanoma cells. *Int. J. Radiat. Biol.* **51** (1), 167-175 (1986).

[33] H. Fukuda, Y. Mishima, J. Hiratsuka, C. Honda, N. Wadabayashi, T. Kobayashi, K. Yoshino, H. Karashima, J. Takahashi and M. Ichihashi, BNCT of malignant melanoma- radiobiological analysis and data comparison with conventional radiotherapy. In *Cancer Neutron Capture Therapy* (Y. Mishima, Ed.), pp. 663-671. Plenum Press, New York, 1996.

[34] P. R. Gavin, F. J. Wheeler, R. Huiskamp, A. Siefert, S. Kraft and C. DeHaan, Large Animal Studies of Normal Tissue Tolerance Using an Epithermal Neutron Beam and Borocaptate Sodium. In *Towards Clinical Trials of Glioma* (D. Gabel and R. Moss, Eds.) pp. 197-209. Plenum Press, New York, 1992.

[35] S. J. González, M. R. Bonomi, G. A. Santa Cruz, H. R. Blaumann, O. A. Calzetta Larrieu, P. Menéndez, R. Jiménez Rebagliati, J. Longhino, D. B. Feld, M. A. Dagrosa, C. Argerich, S. G. Castiglia, D. A. Batistoni, S. J. Liberman and B. M. C. Roth, First BNCT treatment of a skin melanoma in Argentina: Dosimetric Analysis and clinical outcome. *Appl. Radiat. Isotopes* **61,** 1101-1105 (2004).

[36] S. González, P. Suarez, V. Cazoll, G. Santa Cruz, D. Feld, P. Menéndez, Implementación del planificador MacNCTPLAN para BNCT en ARGENTINA. In *VIII Congreso Argentino de Física Médica*. SAFIM, Argentina, 1999.

[37] S. J. González, G. A. Santa Cruz, W. S. Kiger III, J. T. Goorley, M. R. Palmer, P. M. Busse and R. G. Zamenhof, NCTPlan, the New PC version of MacNCTPlan: Improvements and Verification of a BNCT Treatment Planning System. In *Proceedings of the Tenth International Congress on Neutron Capture Therapy* (W. Sauerwein, R. Moss and A. Wittig, Eds.), pp. 557-561. Monduzzi Editore, Bologna, 2002.

[38] S. J. González, G. A. Santa Cruz, W. S. Kiger III and R. G. Zamenhof, A new computational tool for constructing dose-volume histograms using combinatorial techniques. In *Proceedings of the Tenth International Congress on Neutron Capture Therapy* (W. Sauerwein, R. Moss and A. Wittig, Eds.), pp. 629-633. Monduzzi Editore, Bologna, 2002.

[39] J. T. Goorley, G. McKinney, K. Adams and G. Estes, MCNP enhancements, parallel computing and error analysis for BNCT, In *Frontiers in Neutron Capture Therapy* (M. Hawthorne, K. Shelly and R. Wiersena, Eds.) Vol. 1, pp 599-604. Plenum Publishing Corporation, New York, 2001.

[40] T. Goorley, J. Capala, F. Wheeler, W. S. Kiger III, R. Zamenhof, M. R. Palmer, and D. Nigg, A comparison of two treatment planning programs: BNCT-RTPE and MacNCTPlan, *Frontiers in Neutron Capture Therapy* Vol. 1, pp 207-212. Plenum Publishing Corporation, New York, 2001.

[41] J. T. Goorley, W. S. Kiger III and R. G. Zamenhof, Reference Dosimetry Calculations for Neutron Capture Therapy with Comparison of Analytical and Voxel Models. *Med. Phys.* **29** (2), 145-156 (2002).

[42] E. J. Hall, *Radiobiology for the Radiologist*, Lippincott Williams & Wilkins, Philadelphia, 1994.

[43] O. K. Harling, J.-M. Chabeus, F. Lambert and G. Yasuda, A prompt-gamma neutron activation analysis facility using a diffracted thermal neutron beam. *Nucl. Instrum. Meth. Phys. Res. Section B* **83**, 557-562 (1993).

[44] O. K. Harling, K. J. Riley, P. J. Binns, W. S. Kiger III, J. Capala, V. Giusti, P. M. Munck af Rosenschold, K. Skold, I. Auterinen, T. Seren, P. Kotiluoto, J. Uusi-Simola, T. Seppälä, M. Marek, L. Viererbl, F. Spurny, F. Stecher-Rasmussen, W. P. Voorbraak, J. Morrisey, R. L. Moss, O. Calzetta Larrieu, H. Blaumann and J. Longhino, International Dosimetry Exchange: A Status Report. In *Proceedings of the Tenth International Congress on Neutron Capture Therapy* (W. Sauerwein, R. Moss and A. Wittig, Eds.), pp. 333-339. Monduzzi Editore, Bologna, 2002.

[45] H. Hatanaka and Y. Nakagawa, Clinical results of long surviving brain tumour patients who underwent boron neutron capture therapy. *Int. J. Radiat. Oncol. Biol. Phys.* **28,** 1061-1066 (1994).

[46] J. Hiratsuka, H. Fukuda, T. Kobayashi, K. Yoshino, C. Honda, M. Ichihashi and Y. Mishima, Long term outcome of boron neutron capture therapy for malignant melanoma. In *Proccedings of the Ninth International Symposium on Neutron Capture Therapy for Cancer*, pp. 165-166. Osaka, 2000.

[47] J. H. Hubbell and S. M. Seltzer, Tables of X-Ray Mass Attenuation Coefficients and Mass Energy-Absorption Coefficients 1 keV to 20 MeV for Elements Z = 1 to 92 and

48 Additional Substances of Dosimetric Interest, NISTIR 5632. *National Institute of Standards and Technology*, 1995.

[48] R. J. Howerton, D. E. Cullen, R. C. Haight, M. H. MacGregor, S. T. Perkins and E. F. Plechaty, The LLL Evaluated Nuclear Data Library (ENDL): Evaluation Techniques, Reaction Index, and Descriptions of Individual Reactions. *Report UCRL-50400*, Vol. 15, Part A. Lawrence Livermore Scientific Laboratory, 1975.

[49] IAEA-TECDOC-1223. *Current status of neutron capture therapy*, IAEA, Australia, 2001.

[50] ICRU, Tissue substitutes in radiation dosimetry and measurement, *International Commission on Radiation Units and Measurements Report* 44 (Bethesda, MD: ICRU), 1989.

[51] ICRU, Photon, Electron, Proton, and Neutron Interaction Data for Body Tissues *International Commission on Radiation Units and Measurements Report* 46 (Bethesda, MD: ICRU), 1992.

[52] ICRU, Nuclear data for neutron and proton radiotherapy and for radiation protection *International Commission on Radiation Units and Measurements Report* 63 (Bethesda, MD: ICRU), 1999.

[53] D. T. Ingersoll, C. O. Slater, E. L. Redmond and R. G. Zamenhof, Comparison of TORT and MCNP Dose Calculations for BNCT Treatment Planning. In *Advances in Neutron Capture Therapy* (B. Larsson, J. Crawford and R. Weinreich, Eds.) Vol. I, pp. 95-99. Elsevier Science B.V., Amsterdam, 1997.

[54] R. Jiménez Rebagliati and M. A. Dagrosa, Análisis de los resultados de (B) en tejidos, Technical Report CNEA BNCT-c.47/04 (2004).

[55] W.S. Kiger, III, M.R. Palmer, K.J. Riley, R.G. Zamenhof and P.M. Busse, A pharmacokinetic model for the concentration of ^{10}B in blood after boronophenilalanine-fructose administration in humans. *Radiat. Res.* **155**, 611-618 (2001).

[56] W. S. Kiger, III, G. A. Santa Cruz, S. J. González, F.-Y. Hsu, K. J. Riley, P. J. Binns, O. K. Harling, M. R. Palmer, P. M. Busse, and R.G. Zamenhof, Verification and Validation of the NCTPlan Treatment Planning Program. In *Proceedings of the Tenth International Congress on Neutron Capture Therapy* (W. Sauerwein, R. Moss and A. Wittig, Eds.), pp. 613-616. Monduzzi Editore, Bologna, 2002.

[57] W. S. Kiger III, R. G. Zamenhof, G. R. Solares, E. L. Redmond II and C. S. Yam, MacNCTPlan: An Improved Macintosh-Based Treatment Planning Program for Boron Neutron Capture Therapy. *Trans. Am. Nuc. Soc.* **75,** 38 (1996).

[58] G. F. Knoll. *Radiation Detection and Measurements*, John Wiley & Sons, New York (1989).

[59] M. W. Konijnenberg, L. G. Dewit, B. J. Mijnheer, C. P. Raaijmakers and P. R. Watkins, Dose homogeneity in boron neutron capture therapy using an epithermal neutron beam. *Radiat. Res.* **142** (3), 327-39 (1995).

[60] P. Kotiluoto, P. Hiismäki and S. Savolainen, Application of the new MultiTrans SP3 radiation transport code in BNCT dose planning. *Med. Phys.* **28,** 1905-1910 (2001).

[61] E. L. Kreimann, M. E. Itoiz, J. Longhino, H. Blaumann, O. Calzetta and A. E. Schwint, Boron Neutron Capture Therapy for the Treatment of Oral Cancer in the Hamster Cheek Pouch Model. *Cancer Res.* **61**, 8638-8642 (2001).

[62] H. Kumada, K. Yamamoto, A. Matsumura, T. Yamamoto, Y. Nakagawa, K. Nakai and T. Kageji, Verification of the computational dosimetry system in JAERI (JCDS) for boron neutron capture therapy. *Phys. Med. Biol.* **49,** 3353-3365 (2004).

[63] W. R. Leo. *Techniques for Nuclear and Particle Physics Experiments*, Springer-Verlag, Germany, 1994.

[64] S. J. Liberman, M. A. Dagrosa, R. Jimenez Rebagliati, M. R. Bonomi, B. M. C. Roth, L. Turjanski, S. G. Castiglia, S. J. González, P. Menéndez, R. Cabrini, M. J. Roberti and D. A. Batistoni, Biodistribution studies of boronophenylalanine-fructose in melanoma and brain tumor patients in Argentina. *Appl. Radiat Isotopes*, **61** (5), 1095-1100 (2004).

[65] G. L. Locher, Biological effects and therapeutic possibilities of neutrons. *Am. J. Roentgenol.*, **36**, 1-13 (1936).

[66] J. Longhino, H. Blaumann, O. Calzetta, D. Feld and S. González, Caracterización dosimétrica dos ejes en fantoma de referencia en el haz mixto de la facilidad de BNCT del Reactor RA-6. *Technical Report* CNEA-CAB 47/007/03.

[67] J. Longhino, O. Calzetta Larrieu and H. Blaumann, Experimental Determination of the Thermal Neutron Sensitivity of a TE Ionisation Chamber. In *Proceedings of the Tenth International Congress on Neutron Capture Therapy* (Sauerwein, R. Moss and A. Wittig, Eds.), pp. 489-493. Monduzzi Editore, Bologna, 2002.

[68] H. Madoc-Jones, R. Zamenhof, G. Solares, O. Harling, C-S Yam, K. Riley, S. Kiger, D. Wazer, G. Rogers and M Atkins, A Phase-I dose escalation trial of boron neutron capture therapy for subjects with metastatic subcutaneous melanoma of the extremities. In *Cancer Neutron Capture Therapy* (Y. Mishima, Ed.), pp. 707-716. Plenum Press, New York, 1996.

[69] J. L. Mallesch, D. E. Moore, B. J. Allen, W. H. McCarthy, R. Jones and W. Stening, The pharmacokinetics of p-boronophenylalanine.fructose in human patients with glioma and metastatic melanoma. *Int. J. Radiat. Oncol. Biol. Phys.* **28**, 1183-1188 (1994).

[70] E. L. Matos, D. I. Loria, N. Zingarini, M. M. Fernández, G. Guevel, E. Marconi, A. Spitale and S. Rosso, *Atlas de Mortalidad por Cáncer. Argentina 1997-2001,* Universidad de Buenos Aires, Argentina, 2003.

[71] R. L. Maughan, P. J. Chuba, A. T. Porter, E. Ben-Josef and D. R. Lucas, The elemental composition of tumors: Kerma data for neutrons. *Med. Phys.* **24**, (8), 1241-1244 (1997).

[72] R. L. Maughan, P. J. Chuba, A. T. Porter, E. Ben-Josef, D. R. Lucas and B. E. Bjarngard, Mass energy-absorption coefficients and mass collision stopping powers for electrons in tumors of various histologies. *Med. Phys.* **26** (3), 472-477 (1999).

[73] J. M. Moran, D. W. Nigg, F. J. Wheeler and W. F. Bauer, Macroscopic geometric heterogeneity effects in radiation dose distribution analysis for boron neutron capture therapy. *Med. Phys.* **19** (3), 723 732 (1992).

[74] J. D. Moulton, *Nodal Methods: analysis, performance and fast iterative solvers*, Ph. D. Thesis, University of British Columbia, 1996.

[75] T. Nakagawa, K. Shibata, S. Chiba, T. Fukahori, Y. Nakajima, Y. Kikuchi, T. Kawano, Y. Kanda, T. Ohsawa, H. Matsunobu, M. Kawai, A. Zukeran, T. Watanabe, S. Igarisi, K. Kosako and T. Asami, Japanese evaluated nuclear data library version 3 revision2: JENDL-3.2. *J. Nuc. Sci. Technol.* **32**, 1259 (1995).

[76] T. L. Nichols, G. W. Kabalka, L. F. Miller, M. K. Khan and G. T Smith, Improved treatment planning for boron neutron capture therapy for glioblastoma multiforme using fluorine-18 labeled boronophenylalanine and positron emission tomography. *Med. Phys.* **29** (10), 2351-2358 (2002).

[77] D W Nigg, F J Wheeler, D E Wessol, J Capala and M Chadha, Computational dosimetry and treatment planning for boron neutron capture therapy. *J. Neuro-Oncol.* **33**, 93-104 (1997).

[78] D. W. Nigg, C. A. Wemple, D. E. Wessol, F. J. Wheeler, C. Algright, M. Cohen, M. Frandsen, G. Harkin and M. Rossmeier , SERA - An advanced treatment planning system for neutron therapy and BNCT. *Trans. Am. Nuc. Soc.* **80,** 66-68 (1999).

[79] J. Overgaard, The role of radiotherapy in recurrent and metastatic malignant melanoma: a clinical radiobiological study. *Int. J. Radiat. Oncol. Biol. Phys.* 1**2**, 867-872 (1986).

[80] J. Overgaard, M. Overgaard, P. Vejby Hansen and H. von der Maase, Some factors of importance in the radiation treatment of malignant melanoma. *Radiother. Oncol.* **12**, 867-872 (1986).

[81] M. R. Palmer, J. T. Goorley, W. S. Kiger III, P. M. Busse, K. J. Riley, O. K. Harling and R. G. Zamenhof, Treatment planning and dosimetry for the Harvard-MIT Phase I clinical trial of cranial neutron capture therapy. *Int. J. Radiat. Oncol. Biol. Phys.* **53,** 1361-1379 (2002).

[82] T. M. Pawlik and V. K. Sondak, Malignant melanoma: current state of primary and adjuvant treatment. *Crit. Rev. Oncol. Hemat.* **45** (3), 245-264 (2003).

[83] C. P. J. Raaijmakers, I. A. D. Bruinvis, E. L. Nottelman and B. J. Mijnheer, A fast and accurate treatment planning method for boron neutron capture therapy. *Radiother. Oncol.* **46,** 321-332 (1998).

[84] J. A. Rice, *Mathematical Statistics and Data Analysis*, Duxbury Press, 1995.

[85] R. D. Rogus, O. K. Harling and Y. C. Yanch, Mixed field dosimetry of experimental neutron beams for boron neutron capture therapy at the MITR-II research reactor. *Med. Phys.* **21** (10), 1611-1625 (1994).

[86] P.F. Rose, ENDF/B-VI Summary Documentation, BNL-NCS-17541 (ENDF-201) 4th Edition, October 1991.

[87] B. M. C. Roth, P. Menéndez, S. J. Liberman, R. Jiménez Rebagliati, D. A. Batistoni, S. G. Castiglia, M. J. Roberti, Estudio de biodistribución de boro en pacientes con cirugía de melanoma en extremidades. *Technical Report* CNEA BNCT-c.36/03 (2002).

[88] D. N. Slatkin, A history of boron neutron capture therapy of brain tumours-Postulation of brain radiation dose tolerance limit. *Brain* **114,** 1609-1629 (1991).

[89] W. S. Snyder, M. R. Ford, G. G. Warner, and H. L. Fisher Jr., Estimates for absorbed fractions for monoenergetic photon sources uniformly distributed in various organs of a heterogeneous phantom. *J. Nuc. Med. Suppl.* **3**, 47 (1969).

[90] S. C. van der Zee, A. Hogenbirk and S. C. van der Marck, Orange, a Monte Carlo Dose Engine for BNCT. In *Proceedings of the Tenth International Congress on Neutron Capture Therapy* (W. Sauerwein, R. Moss and A. Wittig, Eds.), pp. 569-572. Monduzzi Editore, Bologna, 2002.

[91] W. F. Verbakel, W. Sauerwein, K. Hideghety and F. Stecher-Rasmussen, Boron concentrations in brain during boron neutron capture therapy: in vivo measurements from the phase I trial EORTC 11961 using a gamma-ray telescope. *Int J Radiat Oncol Biol Phys.* **55** (3), 743-56 (2003).

[92] L. S. Waters, *MCNPXTM User's manual Version 2.1.5 TPO-E83-G-UG-X-00001*, University of California, Los Alamos, 1999.

[93] C. Wojnecki and S. Green, A preliminary comparative study of two treatment planning systems developed for neutron capture therapy: MacNCTPlan and SERA. *Med. Phys.* **29** (8), 1710-1715 (2002).

[94] R. Zamenhof, E. Redmond II, G. Solares, D. Katz, K. Riley, S. Kiger and O. Harling, Monte Carlo-based treatment planning for boron neutron capture therapy using cus-

tom designed models automatically generated from CT data. *Int. J. Radiat. Oncol. Biol. Phys.* **35** (2), 383-397 (1996).

[95] R. G. Zamenhof, G. R. Solares, W. S. Kiger III, E. L. Redmond II, P. M. Busse and C.-S. Yam, MacNCTPlan: an improved Macintosh-based treatment planning program for boron neutron capture therapy. In *Advances in Neutron Capture Therapy* (B. Larson, J. Crawford and R. Weinreich,Eds.) Vol I, pp. 100-105. Elsevier Science B.V., Amsterdam, 1997.

[96] C. S. Zuo, P. V. Prasad, P. Busse, L. Tang and R. G. Zamenhof, Proton nuclear magnetic resonance measurements of p-boronophenylalanine (BPA): A therapeutic agent for boron neutron capture therapy. *Med. Phys.* **26** (7), 1230-1236 (1999).